DOT/FAA/PM-86/38

A Preliminary Assessment of Thunderstorm Outflow Wind Measurement with Airport Surveillance Radars

**M. E. Weber
W. R. Moser**

15 May 1987

Lincoln Laboratory

MASSACHUSETTS INSTITUTE OF TECHNOLOGY

LEXINGTON, MASSACHUSETTS

1. Report No.	2. Government Accession No.	3. Recipient's Catalog No.
DOT/FAA/PM-86/38		

4. Title and Subtitle	5. Report Date
A Preliminary Assessment of Thunderstorm Outflow Wind Measurement with Airport Surveillance Radars	15 May 1987
	6. Performing Organization Code

7. Author(s)	8. Performing Organization Report No.
Mark E. Weber and William R. Moser	ATC-140

9. Performing Organization Name and Address	10. Work Unit No. (TRAIS)
Lincoln Laboratory, MIT P.O. Box 73 Lexington, MA 02173-0073	
	11. Contract or Grant No.
	F19628-85-C-0002
	13. Type of Report and Period Covered

12. Sponsoring Agency Name and Address	
Department of Transportation Federal Aviation Administration 800 Independence Ave., SW Washington, DC 20591	Project Report
	14. Sponsoring Agency Code

15. Supplementary Notes

16. Abstract

Modern airport surveillance radars (ASR), situated on or near most major air terminals, feature coherent pulse-Doppler processing, a vertical-fan beam and rapid azimuthal antenna scanning for detection and tracking of aircraft. These radars might serve an additional useful role by making radial wind measurements in the immediate vicinity of an airport so as to provide data on thunderstorm outflow winds. This report presents a preliminary analysis of the capabilities and limitations of ASRs in measuring outflow winds. Principal results are: (1) radar sensitivity is adequate to measure winds associated with weakly reflecting (5-20 dBZ) thunderstorm outflows at ranges less than 20 km provided that appropriate operating parameters are chosen; (2) overhanging precipitation, often moving at a markedly different radial velocity than the outflow, will be a significant source of interference owing to the vertical-fan antenna pattern. If radar reflectivity is approximately constant with altitude, this interference will limit the maximum range for reliable outflow velocity measurements to about 20 km for an outflow that extends 1000 m above the surface and to 7 km for an outflow that extends only 300 m above the surface; (3) At two example major air terminals (Memphis International and Denver Stapleton) ground clutter suppression of approximately 40 dB, combined with the use of inter-clutter visibility techniques, would result in an adequate signal-to-interference ratio for thunderstorm outflow velocity measurement over the significant approach/departure corridors. This result applies when the radar reflectivity factor in the outflow is 20 dBZ or greater and the associated winds extend at least 300 m above the surface.

17. Key Words	18. Distribution Statement
thunderstorm outflows radial velocity measurement airport surveillance radar radar sensitivity to weather echoes overhanging precipitation echoes ground clutter	Document is available to the public through the National Technical Information Service, Springfield, VA 22161.

19. Security Classif. (of this report)	20. Security Classif. (of this page)	21. No. of Pages	22. Price
Unclassified	Unclassified	108	

FORM DOT F 1700.7 (8-69)

ABSTRACT

Modern airport surveillance radars (ASR), situated on or near most major air terminals, feature coherent pulse-Doppler processing, a vertical-fan beam and rapid azimuthal antenna scanning for detection and tracking of aircraft. These radars might serve an additional role by making radial wind measurements in the immediate vicinity of an airport so as to provide data on thunderstorm outflow winds for use with a low level wind shear alert system (LLWAS) and/or a terminal Doppler weather radar (TDWR). The feasibility of radial wind measurements with ASRs is being investigated through numerical simulation and a field measurement program.

This report presents a preliminary analysis of the capabilities and limitations of ASRs in measuring outflow winds. Principal results are:

(1) Radar sensitivity is adequate to measure winds associated with weakly reflecting (5-20 dBZ) thunderstorm outflows at ranges less than 20 km provided that appropriate operating parameters are chosen;

(2) Overhanging precipitation, often moving at a markedly different radial velocity than the outflow, will be a significant source of interference owing to the vertical-fan antenna pattern. If radar reflectivity is approximately constant with altitude, this interference will limit the maximum range for outflow velocity measurements to about 20 km for an outflow that extends 1000 m above the surface. For an outflow that extends only 300 m above the surface, reliable velocity measurements will be possible to about 7 km in range. Thunderstorm outflows that extend well above 1000 m, such as gust fronts, could be reliably measured at considerably greater ranges;

(3) At two example major air terminals (Memphis International and Denver Stapleton) ground clutter suppression of approximately 40 dB, combined with the use of inter-clutter visibility techniques, would result in an adequate signal-to-interference ratio for microburst or gust front velocity measurements over the significant approach/departure corridors. This result applies when the radar reflectivity factor in the outflow is 20 dBZ or greater and the associated winds extend at least 300 m above the surface.

December 31, 1986

iii

TABLE OF CONTENTS

LIST OF ILLUSTRATIONS

A Preliminary Assessment of Thunderstorm Outflow Wind Measurement with Airport Surveillance Radars

I. INTRODUCTION

The Federal Aviation Agency is procuring over 130 new airport surveillance radars (ASR-9). Their primary mission is to detect aircraft while rejecting ground and precipitation clutter. A separate weather channel will provide displays of precipitation reflectivity for use in air traffic control. In view of their high data update rate (4.8 seconds/scan), coherent pulse-Doppler processing and on airport location, it is appropriate to consider whether airport surveillance radars might also detect thunderstorm-generated low altitude wind shear (LAWS) such as microbursts or gust fronts. This would require:

(1) estimation of the radial wind velocity associated with the outflows;

(2) an adaptation of the LAWS detection algorithms that are being developed for use with pencil-beam Doppler weather radars (1,2,3).

Figure I-1 sketches a vertical cross-section of a microburst. A microburst occurs when an intense, small scale downdraft encounters the earth's surface, producing a brief (< 10 minute) outburst of highly divergent horizontal winds (4). Aircraft taking off or landing through a microburst experience increased lift as they enter the outflow, followed by a reduction in lift in the downdraft and tailwind sections of the microburst. Owing to the small spatial extent of microbursts (< 4 km) this sequence is encountered in a period of 1 minute or less. For aircraft on approach to landing, an attempt to keep the plane on its glide slope by reducing power in the headwind section of the microburst may compound subsequent loss of lift in the downdraft and tailwind sections. A number of commercial carrier accidents in recent years have resulted from microburst wind shear (4,5,6).

Gust fronts, as sketched in Figure I-2, are generated by thunderstorm outflows that persist over a longer period of time; thus the leading edge of the outflow may be distant from the generating storm. Squall lines such as encountered in the midwestern portions of the United States produce gust fronts that propagate tens of kilometers away from the generating precipitation. The wind shear encountered by an aircraft penetrating a gust front is generally considered less hazardous than that associated with a microburst since the change is towards greater lift. However, turbulence behind a gust front can be hazardous and the change of wind direction behind the front is of concern for runway usage. Gust fronts are longer lasting phenomena (15 minutes or more) and may result in significant disruption of normal airport operation. Tracking and prediction of gust front arrivals at an airport based on low altitude radial velocity data appears feasible (1) and would yield important cost benefits for airport operation (8).

The limited number of operationally oriented LAWS detection programs to date indicate that the regions of greatest practical concern for LAWS detection are one nmi wide corridors centered on the runway centerlines and extending out about 3 nmi beyond the runway ends (8). These are
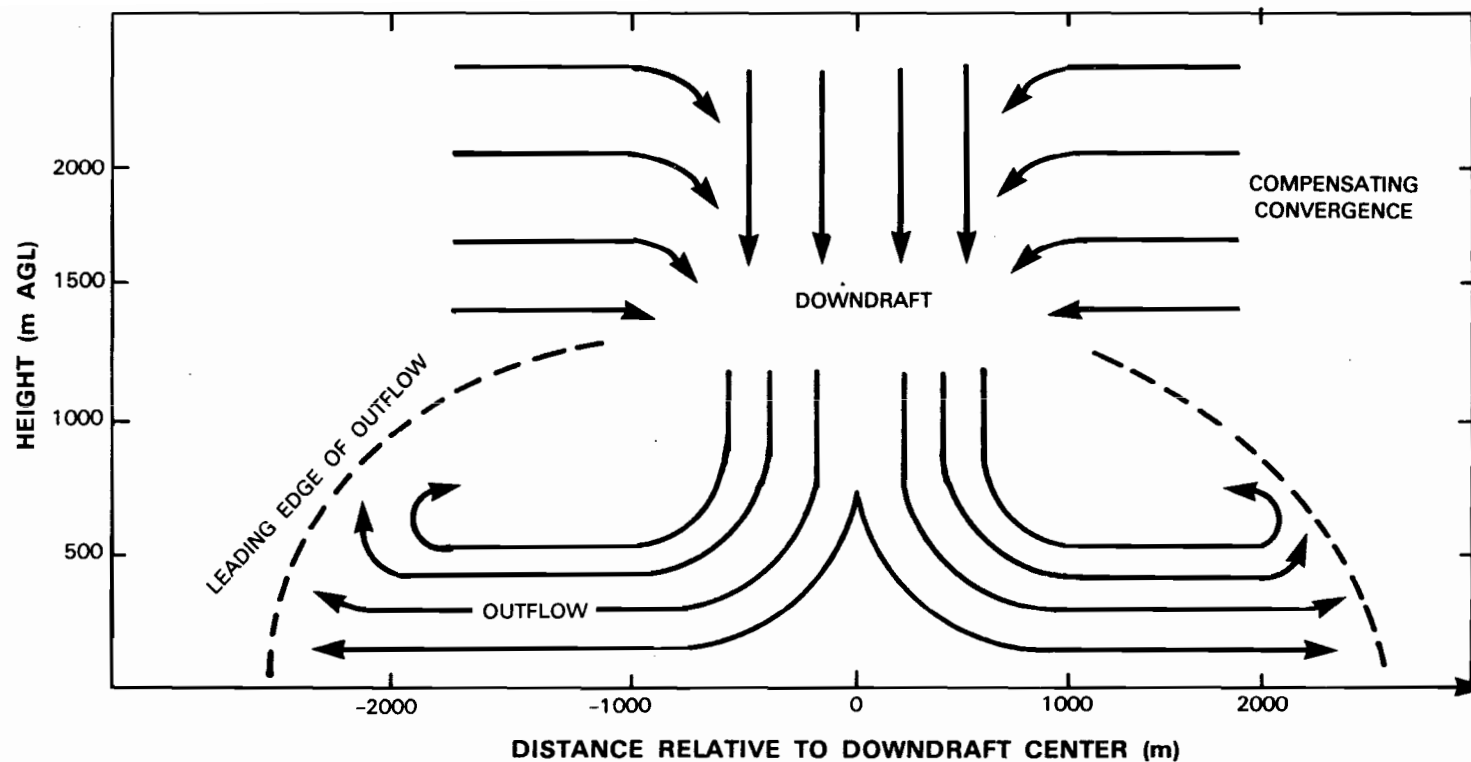
Figure I-1.   Vertical cross section of microburst wind structure.
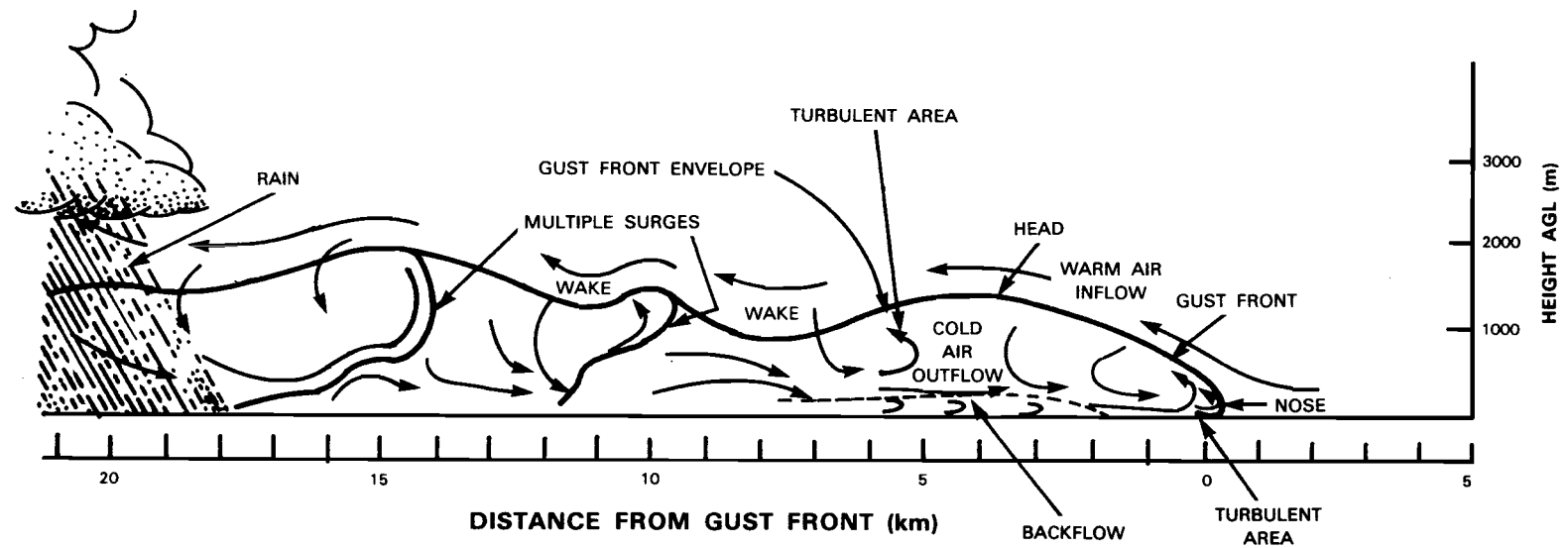
Figure I-2.   Vertical cross section of thunderstorm outflow and gust front. (Adapted from Goff (7)).

the regions in which aircraft on approach or takeoff are less than 1000 feet above ground level. LAWS in the area surrounding these corridors is of concern because the area of wind shear may grow or move into the critical region. Figure I-3 sketches the key areas for microburst detection at a hypothetical airport. Detection of gust fronts at distances up to 25 nmi would be useful for providing predictions of significant wind shift at an airport.

The primary wind-shear sensor under development is a dedicated, terminal Doppler weather radar (TDWR) that will use its pencil beam in a combination of PPI and RHI scans to provide volumetric measurements of storm reflectivity and velocity parameters. The TDWR will provide the capability for nowcasting of fully developed LAWS events and for identification of potential microburst precursors aloft as well as detection and tracking of gust fronts, areas of heavy precipitation, turbulence and tornadoes (9).

It has been suggested that airport surveillance radars could serve as useful adjunct LAWS sensors for airports that will receive a TDWR and as stand-alone systems at those terminals that are not slated for a TDWR. The siting of an ASR, often at runway intersections, or at one end of a major runway, might allow for an improved measurement of headwind-tailwind shear when a TDWR is sited off-airport. It is unlikely that TDWRs will be deployed extensively at secondary terminals or in locales where LAWS is infrequent. At these terminals, an ASR might provide at least some capability for wind-shear detection, particularly in the critical region within 5 - 10 km of an airport. It might also be possible to improve the performance of the low-level wind shear alert system (LLWAS) by using the data from an airport surveillance radar to reduce the LLWAS false-alarm rate and to distinguish between various forms of wind shear.

Table I-1 summarizes principal parameters of the ASR-9. The dual-beamed ASR-8 currently in operation at many airports has very similar radar system parameters. If airport surveillance radars are to be used for LAWS detection, the most likely method would be by way of a processing retrofit that would not affect their primary aircraft detection/tracking mission. Thus wind-shear detection with an ASR will be limited by such factors as the fan-shaped elevation antenna pattern, the short coherent processing intervals (CPI) and the concomitant difficulties in achieving adequate signal-to-interference ratios for estimation of radial velocity in shallow, possibly low-reflectivity microbursts or gust fronts.

Table I-1: ASR-9 Parameters	
Transmitter	
Frequency	2.7-2.9 GHz
Polarization	Linear or Circular
Peak Power	1.1 MW
Pulse Width	1.0 μs
Block-Staggered CPI lengths	8 pulses/10 pulses
PRFs (Example)	972 s^{-1}/1250 s^{-1}
Receiver	
Noise Figure	4.1 dB (max)
Sensitivity	-108 dBm
A/D Word Size	12 bit
Antenna	
Elevation Beamwidth	4.8° (min)
Azimuth Beamwidth	1.4°
Power Gain	34 dB
Rotation Rate	12.5 RPM

3 nmi

3 nmi

3 nmi

3 nmi

1 nmi

≈ 1 nmi

1 nmi

≈ 1 nmi

RUNWAY

KEY LAWS
DETECTION REGION

BOUNDARY OF
SECONDARY LAWS
DETECTION REGION

77540-3
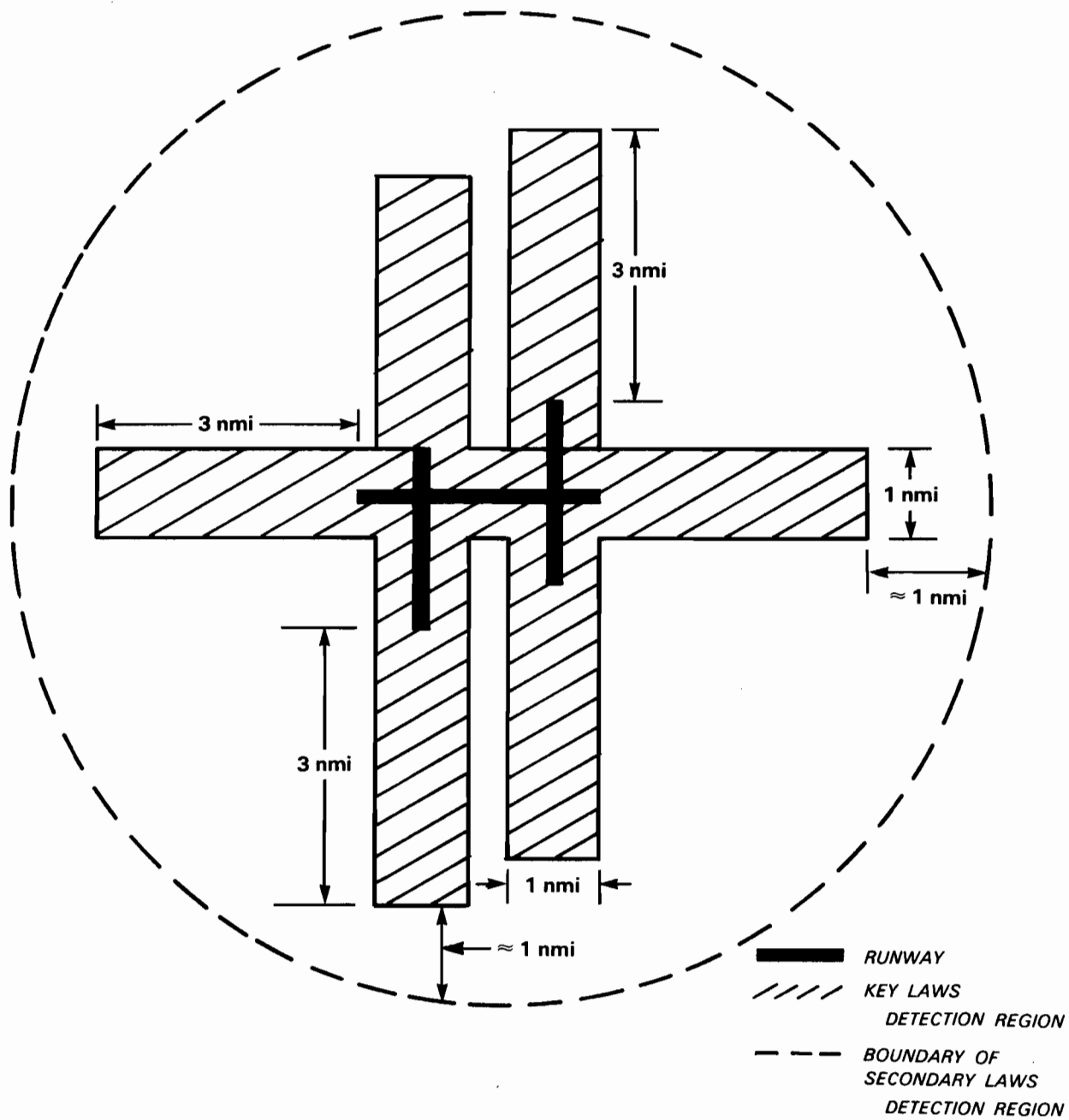
Figure I-3.   Principal microburst detection area for a hypothetical airport.

In this report, we discuss signal-to-interference considerations for detection of LAWS with airport surveillance radars. Receiver sensitivity, the impact of partial filling of the fan-shaped elevation beam, interference from precipitation echoes above the low-altitude outflow and ground clutter will be treated to provide a sense for the capabilities and limitations of ASRs in this role. To be specific, we will use parameters of the ASR-9 in all calculations, although much of the discussion is also applicable to the ASR-8 which has similar antenna and transmitter/receiver characteristics.

II. SIGNAL-TO-NOISE FOR WIND SHEAR DETECTION

A. Radar Reflectivity Factor in Thunderstorm Outflows

Figure II-1, reproduced from Wilson *et al.* (10), shows the spread in the maximum radar reflectivity factor of microbursts detected in the Denver, CO area during the Joint Airport Weather Surveillance (JAWS) program. The median reflectivity factor was 45 dBZ and in 10% of these microbursts, peak reflectivity was 20 dBZ or less. Preliminary analysis of FAA/Lincoln Laboratory Observational Weather System (FLOWS) data from Memphis, TN indicates that while surface radar reflectivities in the moist sub-cloud environment at Memphis are typically larger than at Denver, significant wind shear may still occur in the absence of intense precipitation. Of the 27 microbursts identified in 1984 with the MESONET† network of surface stations, 2 were not accompanied by measurable precipitation (11). Figure II-2, reproduced from Rinehart and Isaminger (12), shows the distribution of maximum low-altitude reflectivity for FLOWS microbursts in 1985. Here, the median reflectivity factor is 55 dBZ and the tenth percentile is 45 dBZ. Two of these microbursts had maximum surface reflectivity less than or equal to 20 dBZ.

The above values represent the maximum surface radar reflectivity in thunderstorm microbursts which may be significantly higher than the reflectivity in the region of greatest wind shear. For example microbursts at Denver and Memphis respectively, Tables II-1 and II-2 list this latter reflectivity factor as well as other parameters that affect microburst detectability. Table II-1 was generated by S.D. Campbell (personal communication) using radar data provided by the National Center for Atmospheric Research. Table II-2 was compiled by M.W. Wolfson (personal communication) using FLOWS radar observations during the 1985 data collection season. The tabulated parameters are: (i) the magnitude of the largest wind (approaching or receding); (ii) the depth of the outflow over the volume of largest wind; (iii) the average of the reflectivity factors in the volumes of maximum outflow approaching and receding velocity; and (iv) the near-surface reflectivity factor in the downdraft core of the microburst.

Table II-1: Example Denver Microburst Features						
Date/Time (MDT)	Radar	Peak Wind (ms^{-1})	Height Resolution (km)	Outflow Depth (km)	$dBz_{outflow}$	dBz_{core}
29 June 1982 1606	CP-2	12	0.8	1.0	21	23
29 June 1982 1606	CP-4	10	0.6	0.9	11	14
8 July 1983 1351	CP-2	8	0.3	0.5	25	23
8 July 1983 1351	CP-4	9	0.3	0.4	19	23
13 July 1982 1506	CP-4	9	0.4	0.4	15	26
14 July 1982 1444	CP-2	9	0.6	0.7	13	14

† A network of meteorological surface stations that sample temperature, relative humidity, atmospheric pressure, rainfall accumulations and wind speed and direction at 30 s intervals.
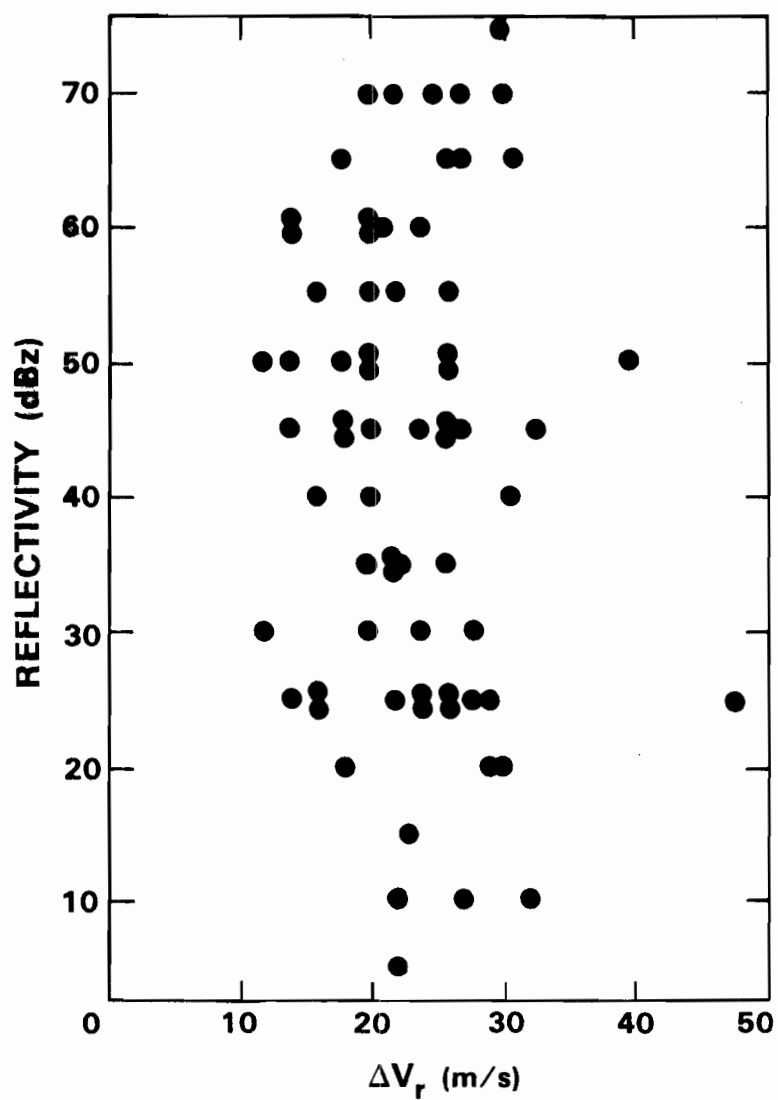
Figure II-1.   Correlogram of maximum radar reflectivity for JAWS microbursts versus maximum velo-
city differential. (Reproduced from Wilson *et al.* (10)).

157729-N
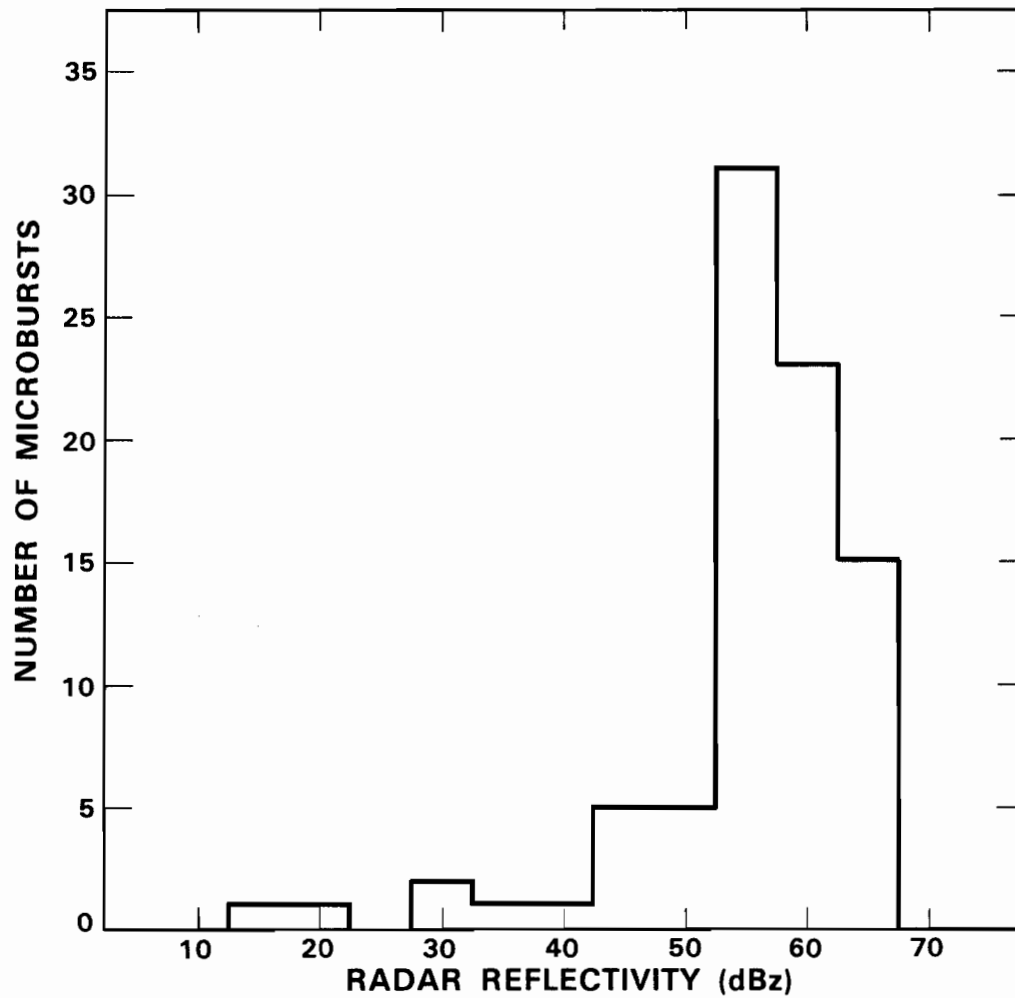
Figure II-2.   Distribution of maximum radar reflectivity factor for FLOWS microbursts. (Reproduced from Rinehart and Isaminger (12)).

9

Table II-2: Summary of Microburst Features for FLOWS Memphis Data in 1985						
Date/Time (CST)	Radar	Peak Wind (ms^{-1})	Height Resolution (km)	Outflow Depth (km)	$dBz_{outflow}$	dBz_{core}
30 April 1985 1452	UND	8	0.8	0.8	20-35	35-40
30 April 1985 1544	UND	24	0.3	0.3-0.6	30	45
30 April 1985 1608	UND	13	0.4	0.5	25	40
26 June 1985 1238	FL-2	14	0.1	0.4	50	50
26 June 1985 1348	FL-2	12	0.3	0.4	50	45
30 June 1985 1705	FL-2	15	0.5	0.8	< 5	50
15 July 1985 1357	FL-2	12	0.1	0.5	25	55
23 July 1985 1418	FL-2	12	0.4	0.5	20	20-50
10 August 1985 1400	FL-2	14	0.2	0.2-0.8	20-45	25-45
15 August 1985 1519	FL-2	12	0.1	0.3	20-45	20-45
24 August 1985 1418	FL-2	12	0.6	0.6	20	40
7 September 1985 1619	FL-2	8	0.2	0.4	10-35	20-40
8 September 1985 1755	UND	13	0.3	0.7	40	40-45

Particularly in the Memphis outflows, radar reflectivity in the head wind and tail wind sections of the microbursts may be significantly lower than in the precipitation core that generates the downdraft. As an example, reflectivity in the Memphis microburst on 30 June varied from 50 dBZ in the precipitation core to 5 dBZ or less in the region of maximum radial velocity. In those Denver microbursts considered in Table II-1, evaporation in the dry sub-cloud layer reduced radar reflectivity even in the downdraft core to values less than 30 dBZ.

Low radar cross-sections may also be presented by gust fronts, once these have propagated away from the precipitation that generates the outflow. Table II-3, condensed from Klingle (13), gives parameters of gust fronts measured at the National Severe Storms Laboratory (NSSL) in Norman, Oklahoma. Minimum radar reflectivities along the gust front range from approximately 0 to 30 dBZ, in conformance with results published in Doviak and Zrnic (14).

For comparison, Figure II-3 plots the minimum detectable signal versus range for an ASR-9, plotted in units of weather reflectivity. The computation, described in Appendix A, assumed that the antenna beam is filled with constant reflectivity precipitation. The dashed curve assumes a
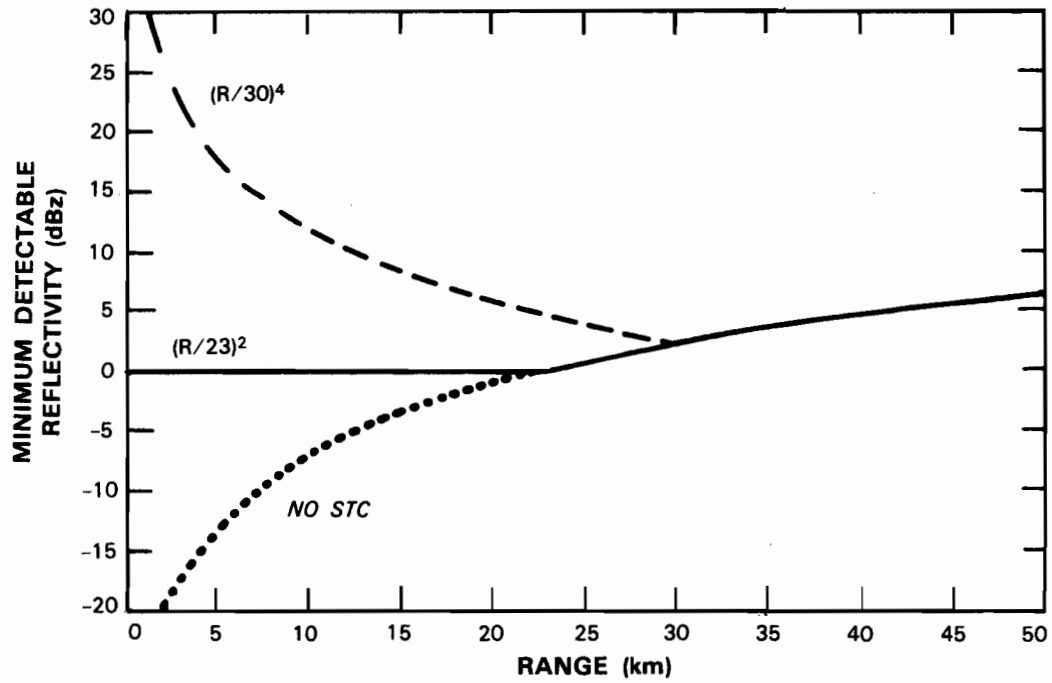
Figure II-3.   Minimum detectable weather reflectivity factor versus range for an ASR-9. The three curves are for different STC functions as described in the text.

Table II-3: Example NSSL Gust Front Features						
Date/Time (CST)	Radar	Peak Wind (ms^{-1})	Height Resolution (km)	Outflow Depth (km)	dBz_{max}	dBz_{min}
30 April 1978 2108†	NRO	28	0.4	3.2	38	5
30 April 1978 2108†	NRO	36	0.2	3.9	33	3
02 May 1978 1740	NRO	16	0.3	0.9	50	25
19 June 1980 2235	NRO	23	0.4	1.1	32	8
15 May 1982 1952	NRO	32	0.9	2.0	47	-1
30 May 1982 2038	NRO	40	0.5	2.8	40	9
17 May 1983 2228	NRO	43	0.7	2.3	43	29
26 April 1984 2029†	NRO	28	0.7	3.6	54	9
26 April 1984 2148†	NRO	36	0.3	1.6	37	7

sensitivity time control (STC) function that varies as $(R/R_0)^4$ where $R_0 = 30$ km. This is representative of STC functions used for aircraft detection at sites with moderate to severe ground clutter. Clearly, at ranges less than about 10 km the attenuation of this STC function is too great for detection of low reflectivity wind shear events.

With the STC disabled (dotted curve) the minimum detectable signal is below 0 dBZ out to 23 km. In this mode, however, receiver clipping from ground clutter or from intense weather echoes would severely degrade radar performance. Assuming that the 12-bit A/D converters are the limiting factor for receiver dynamic range, maximum unsaturated signal power would lie along a curve displaced upwards no more than 65 dB.

As a compromise between the requirements for adequate sensitivity and minimization of clipping, the solid line shows an STC function that varies as $(R/R_0)^2$ where $R_0 = 23$ km. This function gives a constant sensitivity of 0 dBZ out to 23 km, adequate for detection of most thunderstorm outflows. As will be shown in Section IV, ground clutter would produce saturation in a relatively small percent of resolution cells.

The specified configuration of the ASR-9 provides a separate receiver path for weather signals only when circular polarization is employed. Thus, the capability to utilize an STC function that is appropriate for wind-shear detection would depend on the air traffic controllers' willingness to accept the approximately 2.5 dB loss in aircraft target cross-section associated with the use of circular polarization. One alternative would be to provide a second receiver for LAWS processing at short range. This would receive the low beam signal over the range interval where the target channel employs the high beam. Thus a less attenuating STC function could be used in the critical region for LAWS detection without affecting target channel parameters.

† The storms on 30 April 1978 and 26 April 1984 produced two distinct gust fronts.

B. Vertical Structure of LAWS Phenomena

Observations with pencil beam Doppler weather radars have shown that the divergent outflow in microbursts is often shallow. Of those JAWS microbursts where there were sufficient data to identify the top of the outflow, 90% were between 300 m and 1200 m in depth (10). Radar data from FLOWS in 1985 and 1986 indicate that microburst outflows in the southeastern United States are likewise confined to a shallow layer; as indicated in Table II-2 outflow depths measured near Memphis varied from 200 m to 800 m in the region of largest wind speed. Figure II-4 plots example vertical profiles of radial velocity from RHI scans of microbursts near Memphis and Huntsville, AL.

The convergent radial velocity signature produced by gust fronts often extends considerably higher in altitude. Klingle (13) and Doviak and Zrnic (14) indicate that gust fronts are typically observable to 1000 m - 3000 m AGL.

An airport surveillance radar will suffer a significant loss in effective sensitivity against shallow thunderstorm outflows, owing to partial filling of the antenna beam. The loss in sensitivity† , relative to that plotted in figure II-3, is given by:

$$BL = \frac{\int_0^{\theta_0} B_T(\theta)B_R(\theta)d\theta}{\int_0^{\frac{\pi}{2}} B_T(\theta)B_R(\theta)d\theta} \tag{1}$$

where $B_T(\theta)$, $B_R(\theta)$ are the transmit and receive elevation antenna patterns and θ_0 is the angle subtended by the top of the thunderstorm outflow. Figure II-5 plots the one-way elevation patterns for the ASR-9's low (solid) and high (dotted) antenna beams. An antenna tilt of 2.0° is assumed. The dashed curve is the "effective" high-beam pattern given that signal transmission is on the low beam. Figure II-6 plots the associated beamfilling loss as functions of range for assumed outflow depths of 300 m, 500 m, 1000 m and 3000 m. The solid curves are for the low receiving beam and the dashed curves are for the high beam. Figure II-7 combines the losses for a 300 m and 500 m thick outflow layer with the sensitivity calculation in Figure II-3. (An $(R/23km)^2$ STC function is assumed.)

Assuming that the range at which the switch from the high to the low receiving beam occurs is no greater than 30 km, the curves indicate that echoes from a 3 km thick gust front would be reduced by no more than 4 dB. For a shallow microburst however, the loss could exceed 20 dB in the high beam at operationally significant ranges. The plots indicate that it would be desirable to use the low receiving beam, even at short range, for detection of shallow thunderstorm outflows. For example, at 20 km range the minimum detectable reflectivity factor for a microburst 300 m in depth would be 12 dBZ in the low beam and 23 dBZ in the high beam. In ten percent of the microbursts measured during the JAWS program in a dry sub-cloud environment, peak surface reflectivity was less than the latter value (Figure II-1). As indicated in Table II-2, reflectivity factors in the region of greatest wind shear are sometimes lower than 23 dBZ, even when the sub-cloud layer is moist as in Memphis.

---

† This loss applies to the weather echo spectrum component that is returned from scatterers in the outflow. The impact of the spectrum component returned from precipitation scatterers above the outflow is treated in Section III.
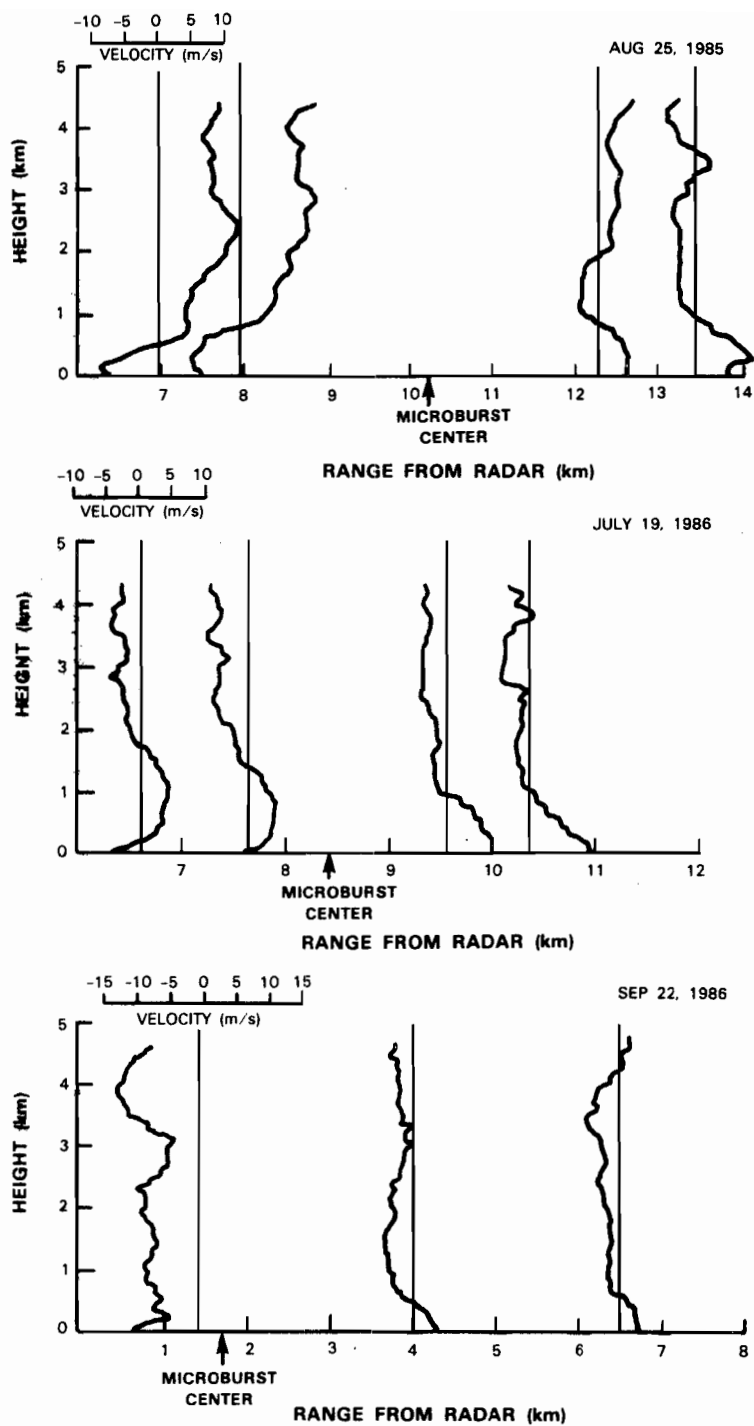
Figure II-4.   Vertical distribution of the windspeeds of three FLOWS microbursts. The horizontal distance from the radar to each profile is indicated by the associated vertical line. This line also marks the zero point for the radial velocity scale.

14
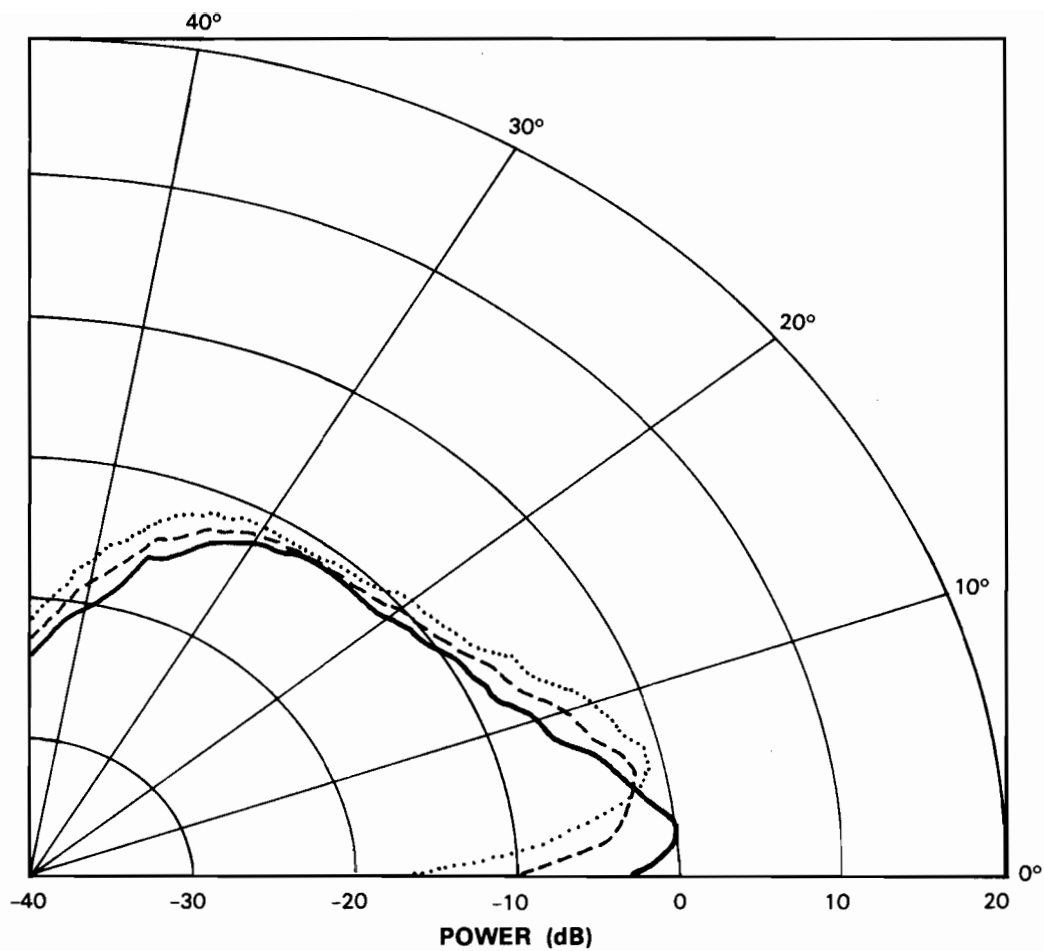
Figure II-5. One-way elevation antenna patterns for an ASR-9. An antenna tilt of 2.0° is assumed. The solid line is the pattern for the active (transmit and receive) low beam. The dotted line is the pattern for the receive-only high beam. The dashed line is the effective high beam pattern (the square root of the product of the low and high beam patterns), given that signal transmission is on the low beam.

15
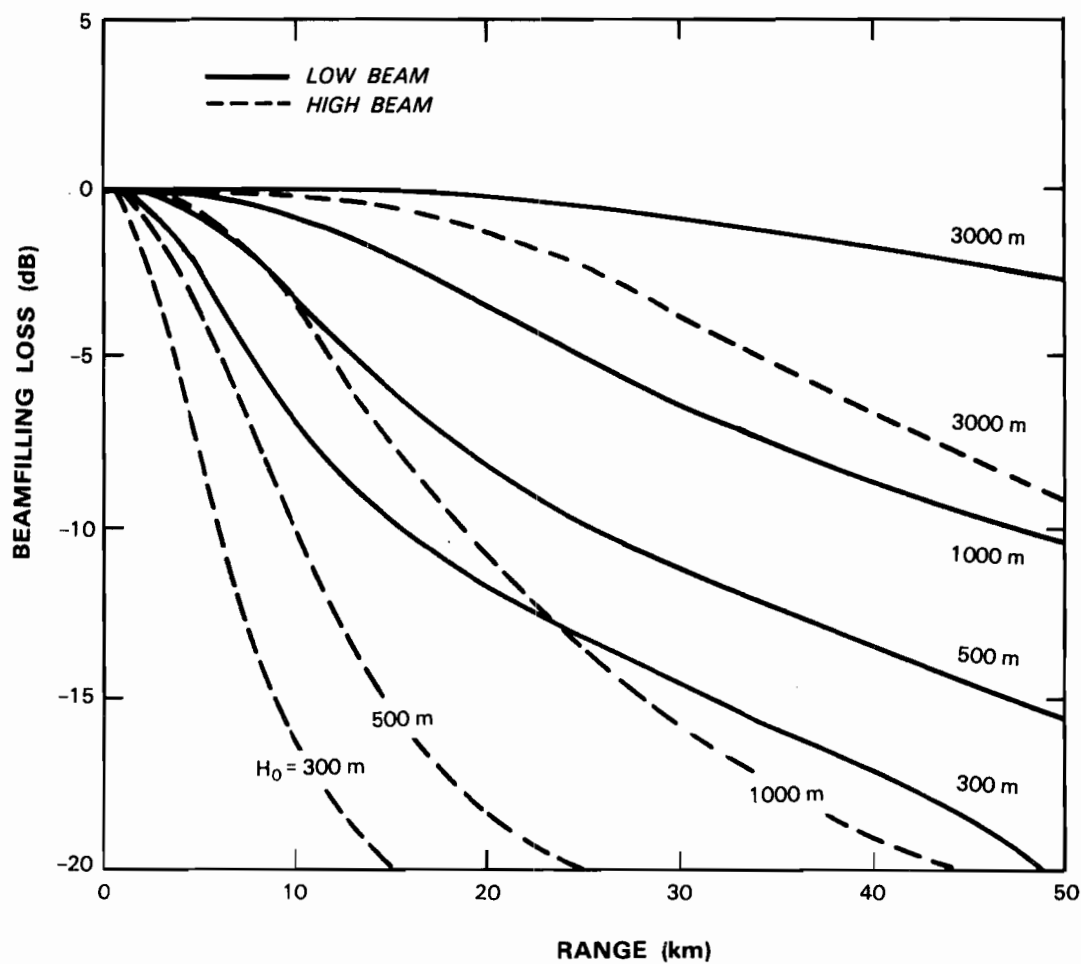
Figure II-6.   Beamfilling loss versus range for an ASR-9. The different curves are for echoes extending from the surface to the indicated heights.

16
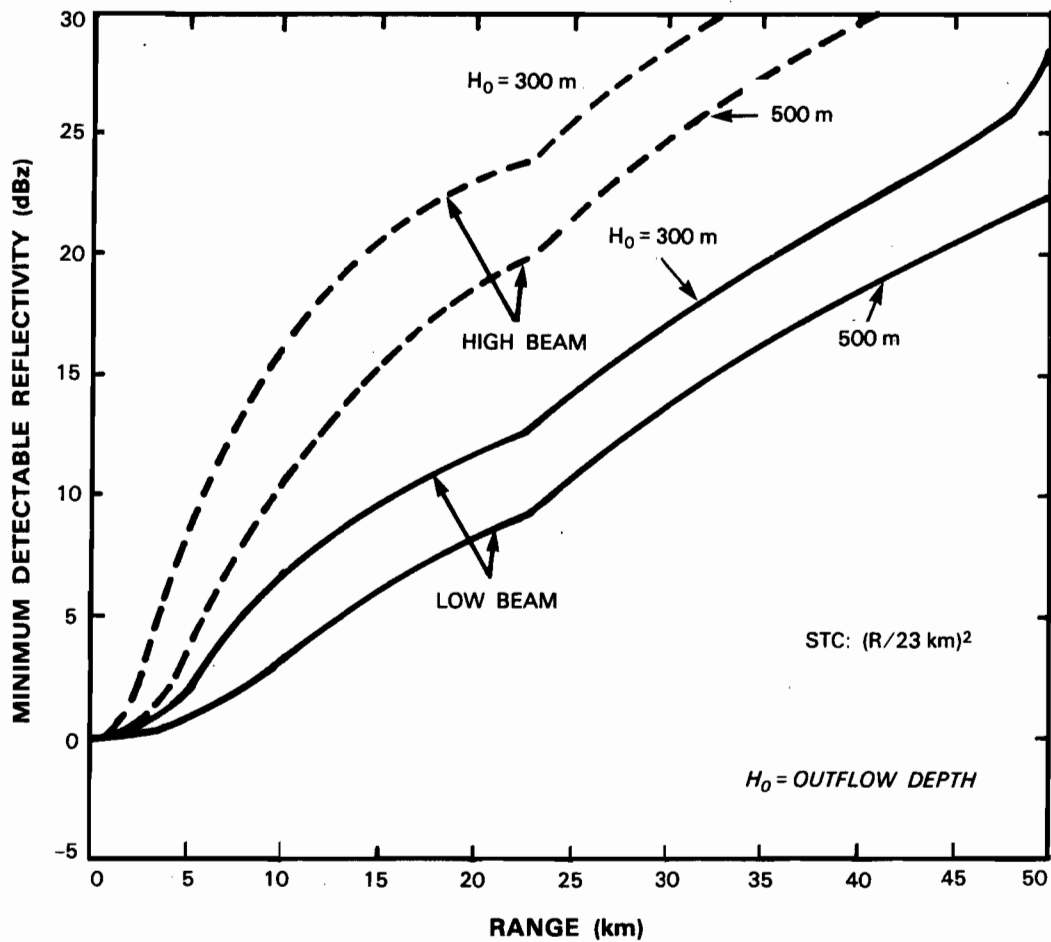
Figure II-7.   ASR-9 minimum detectable weather reflectivity factor including the beamfilling losses for a 300 or 500 m deep thunderstorm outflow layer. An $(R/23km)^2$ STC function is assumed.

III. INTERFERENCE FROM PRECIPITATION ECHOES ABOVE THE OUTFLOW

A. Single-Beam Measurement

Owing to its fan-shaped elevation beam pattern, an airport surveillance radar will receive significant scattered power from precipitation above shallow thunderstorm outflows, even at short ranges. For example, a 500 m deep outflow will fill the radar's low-beam 3 dB limits only to 5.7 km in range. At greater ranges, the velocity spectrum of the precipitation echo will be significantly modified by higher altitude scatterers with a different radial velocity (typically lower in magnitude and/or of opposite sign). Mean velocity estimators, for example the pulse-pair method, will therefore underestimate the true outflow velocity when the power contribution from these scatterers is significant (e.g. -5 dB relative to power from scatterers in the outflow layer). Full spectral estimation (conventional or nonlinear) might resolve the outflow velocity component at lower signal to interference ratios, but an algorithm for identification of the spectral component of interest is required. In any case, this "clutter" -- closely related to the beamfilling loss discussed previously -- further limits an airport surveillance radar's detection range for LAWS events.

The ratio of power from scatterers in the outflow region, P(S), to power from scatterers at higher altitudes, P(C), is given by:

$$\frac{P(S)}{P(C)} = \frac{\int_0^{\theta_0} Z(\theta)B_T(\theta)B_R(\theta)d\theta}{\int_{\theta_0}^{\frac{\pi}{2}} Z(\theta)B_T(\theta)B_R(\theta)d\theta} \tag{2}$$

$$= (1/BL - 1)^{-1}$$

where the beamfilling loss, BL, was defined in equation (1). Here $Z(\theta)$ is the cloud reflectivity profile versus elevation angle. The second equality holds when precipitation reflectivity is constant over the elevation angle interval where antenna gain is significant ($< 40°$). Obviously, this ratio decreases as the beamfilling loss increases (i.e. BL becomes smaller). Thus loss of sensitivity for shallow wind shear events, owing to partial beamfilling, is compounded by an increase in the interference background. Figure III-1 plots the power ratio of equation (2) as a function of range for the outflow depths considered previously (300 m, 500 m, 1000 m and 3000 m). The calculation assumes constant radar reflectivity from the surface to 10000 m. If the high receiving beam is used, this power ratio becomes less than unity at ranges of 3,5,10 and 29 km respectively for the above outflow depths. If the ground clutter environment permits data from the low receiving beam to be used, these ranges increase to 6,10,19 and 55 km.

1. Simulation of ASR Velocity Reports Using Simplified Outflow Models

To determine an ASR's detection range using a specific velocity estimator -- the pulse-pair method -- we simulated time-series weather signals corresponding to a simple model of the vertical distribution of precipitation reflectivity and radial velocity in a thunderstorm outflow and the ASR
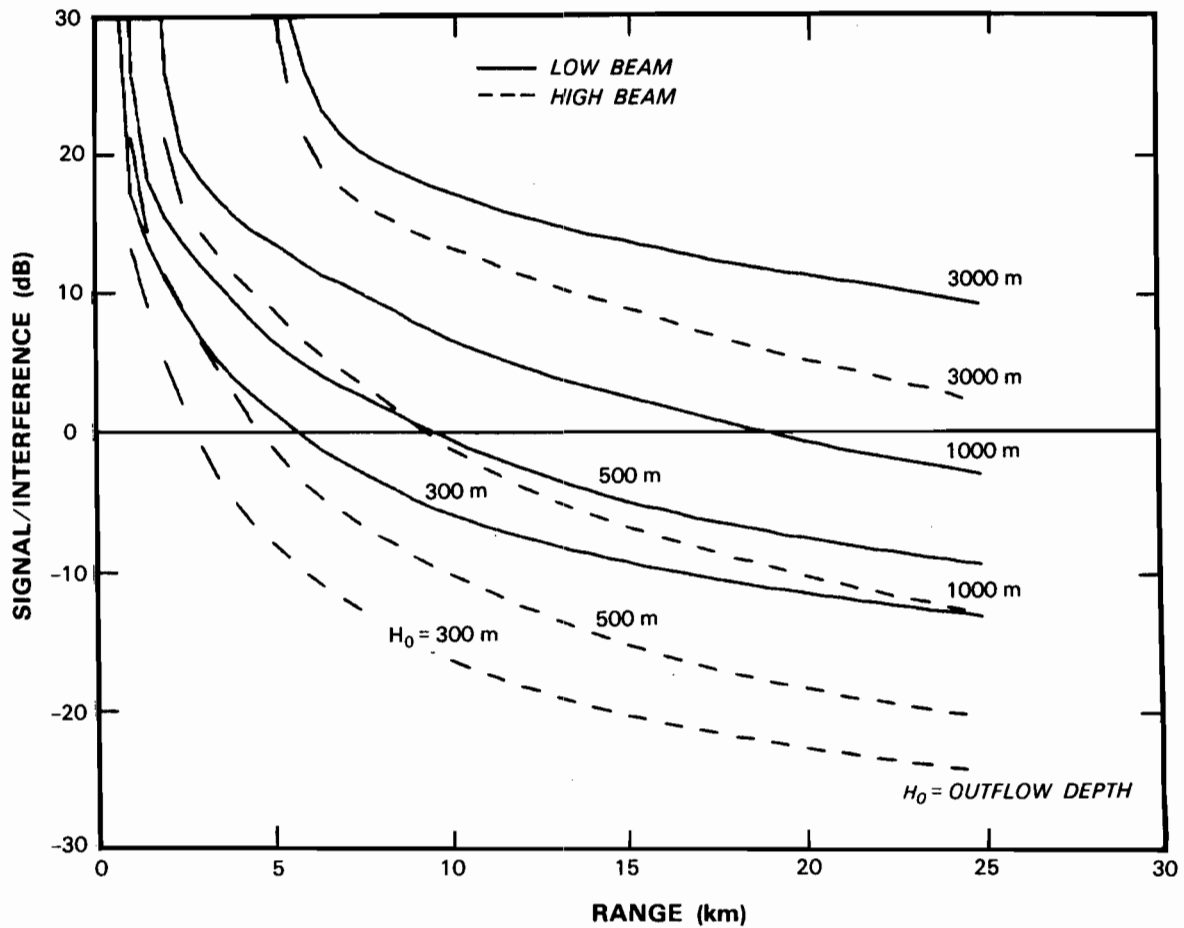
Figure III-1.   Decibel ratio of echo power from precipitation in a thunderstorm outflow layer to power scattered from precipitation above the outflow. The assumed depth of the outflow layer is indicated on each curve. The solid curves are for the low receiving beam and the dashed curves are for the high beam. The computation assumes constant radar reflectivity from the surface to 10 km AGL.

elevation beam patterns. The power spectrum of the precipitation echo sensed by a fan-beamed radar is related to the elevation angle resolved power spectra, $S(V,\theta)$ by:

$$\tilde{S}(V) = \left\{ \frac{\int_0^{\frac{\pi}{2}} S(V,\theta) B_T(\theta) B_R(\theta) d\theta}{\int_0^{\frac{\pi}{2}} B_T(\theta) B_R(\theta) d\theta} \right\} * S_{SM}(V) \qquad (3)$$

Convolution with the Gaussian scan modulation function, $S_{SM}(V)$, accounts for the increase in spectrum width caused by the rapidly scanning ASR antenna. A white-noise spectral component corresponding to the noise level for an ASR-9 was added to the spectrum of equation (3). In calculating the noise level, we assumed use of an $(R/23km)^2$ STC function as discussed in section II.

20

From the calculated spectrum, I and Q time-series weather data were simulated using a technique analogous to that described by Sirmans and Bumgarner (15). This Monte Carlo approach simulates statistical realizations of the mean weather spectrum where the amplitude distribution of each frequency component is Rayleigh distributed and the phase is uniformly distributed between 0 and 2π. Inverse Fourier transformation of this complex spectrum produces a time-series with appropriate statistical attributes, conforming to the input power spectrum shape. We used 128 point transforms and extracted from the resulting time-series one 8-point segment, corresponding to the low-PRF coherent processing interval (CPI) for an ASR-9. Pulse pair velocity estimates:

$$\hat{V} = -\frac{\lambda}{4\pi\tau_S} ARG \left\{ \sum_{i=1}^{i=N-1} x_{i+1} x^*_i \right\} \tag{4}$$

were formed where λ is the radar wavelength, τ_S the pulse repetition period, the x_i are the time samples and N is the number of pulses in a CPI.

The standard deviation of the resulting velocity estimates is large owing to the short CPIs available for averaging of autocorrelation lag estimates and the large spectrum width associated with the vertical shear in radial velocity. In practice, velocity estimate variance could be substantially reduced by incoherent averaging of estimates obtained on at least six successive antenna scans, since the 4.8 s scan period is short in comparison to the time scale for significant evolution of a microburst or gust front. We have assumed incoherent averaging of six independent velocity estimates in the simulations presented.

The mean and standard deviation of 128 such velocity estimates were computed at 1 km increments from 1-30 km to illustrate the LAWS detection performance versus range for an ASR. Figures III-2 and III-3 plot the +/- one standard deviation limits for the velocity estimates, assuming:

(i)   outflow depths of 300 m, 500 m, 1000 m and 3000 m as above;

(ii)   constant reflectivity of 30 dBZ from the surface to 10,000 m;

(iii) a radial velocity of –15 ms^{-1} in the outflow layer, changing discontinuously to +5 ms^{-1} above this layer.

The weather spectrum width in each of the two layers is taken as equal to a relatively high value of 3 ms^{-1} to simulate the effect of additional vertical shear in radial velocity within the layers considered. The two figures treat separately the low and the high receiving beam. Note that the maximum range considered is well beyond operational requirements for microbursts. As indicated in the introduction, however, detection and tracking of gust fronts at relatively long range from an airport may be useful.

As expected, when signal power is dominated by returns from one of the two layers considered, the pulse-pair velocity estimates accurately reflect radial velocity in that layer. This situation occurs at short range when the low-altitude outflow dominates and (for the shallower outflows) again at long range where echoes from the overhanging precipitation are the stronger component. At intermediate ranges where the spectral power associated with the two components is comparable, the velocity estimates reflect the average velocity between the two layers.

We will arbitrarily define the outflow maximum "detection range" as the range at which the mean of the velocity estimates equals –5 ms^{-1}, the midpoint between the radial velocities in the two layers considered. For the low beam, this range is 7, 11, and 19 km for outflow depths of 300, 500 and 1000 m respectively. In the high beam the corresponding ranges are 3, 5 and 9 km. As would be expected, these detection ranges correspond to the range at which the signal-to-interference ratio plotted in figure III-1 drops below 0 dB. For the deeper 3000 m outflow model,
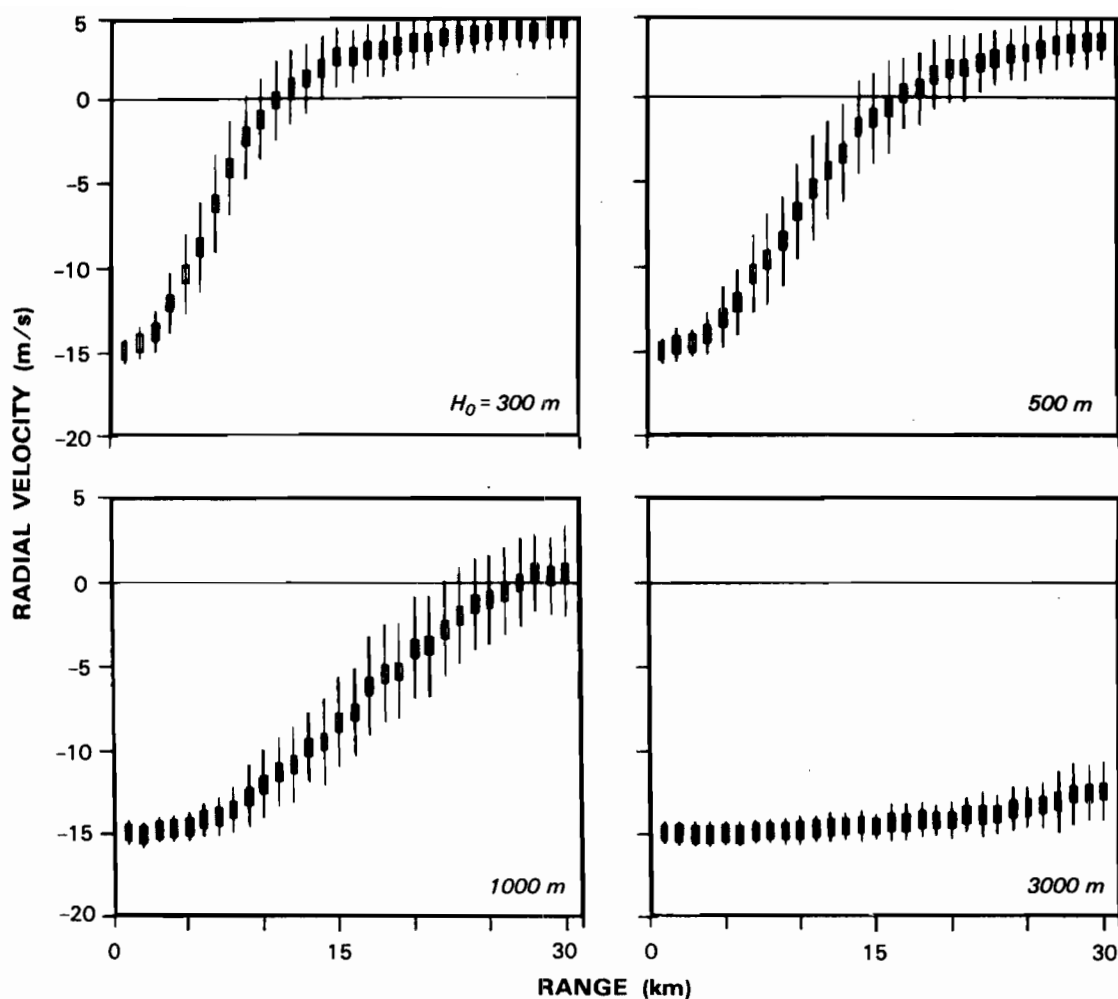
Figure III-2. Monte Carlo simulation of mean and standard deviation of pulse-pair velocity estimates versus range. Each plot assumes: (i) uniform reflectivity from the surface to 10 km; (ii) an outflow layer from the surface to the indicated height where the radial velocity component is -15 ms^{-1}; (iii) radial velocity of 5 ms^{-1} at all altitudes above this layer. The simulation assumed that the low receiving beam is used.
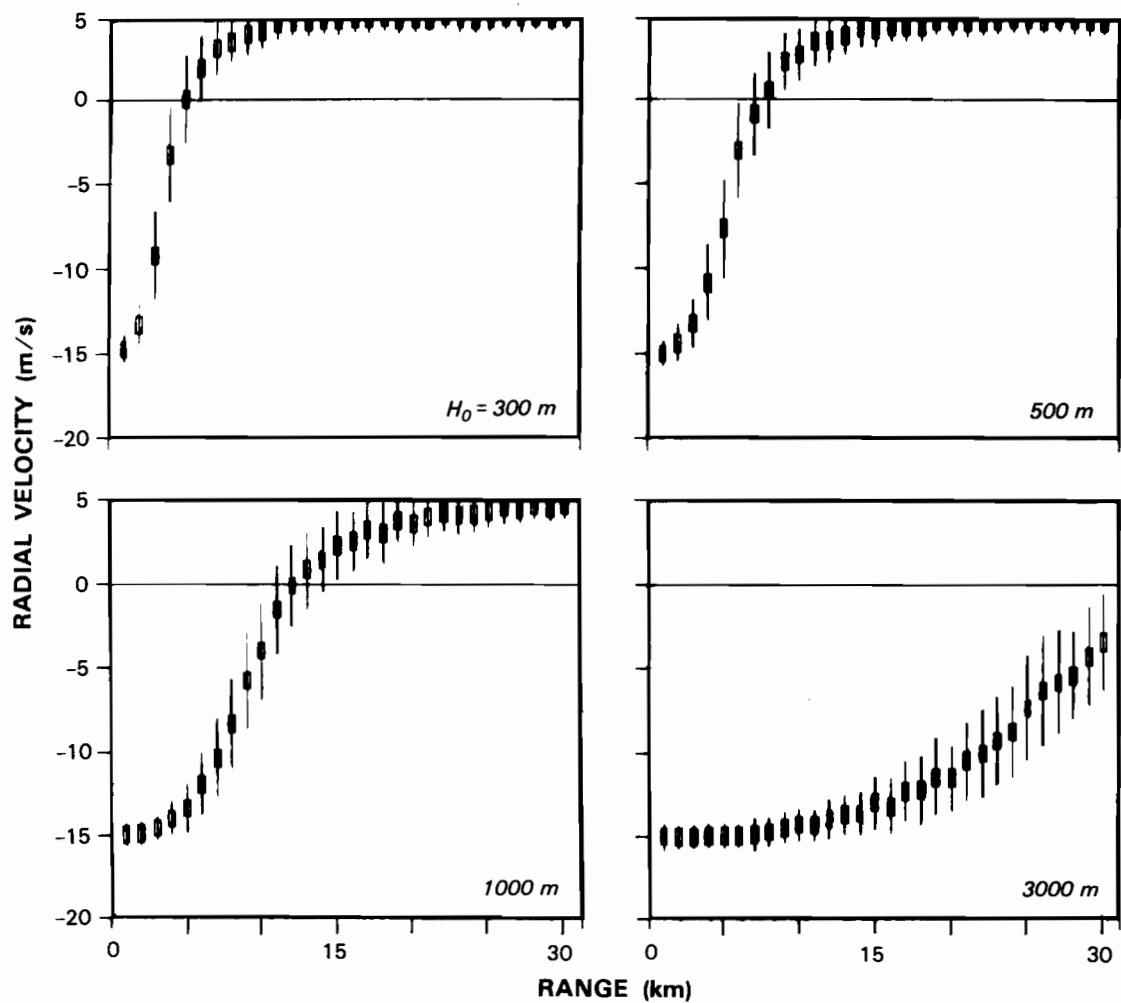
Figure III-3.   As in Figure III-2, except that use of the high receiving beam is assumed.

23

77540-9

the low beam would detect the outflow well beyond the 30 km range limit considered whereas the high beam would detect it to 26 km range.

The simple outflow models used here suggest that the elevation beam patterns of an ASR will limit microburst detection with straightforward mean velocity estimators to ranges of about 20 km or less. Gust fronts should be detectable at much longer ranges, given that they may extend well above 1000 m in height and may have propagated away from highly reflective overhanging precipitation. As is the case with the radar sensitivity issue discussed in the previous section, better detection performance would be obtained if the ground clutter environment allowed for use of low-beam data in the critical region within 10 km of an airport.

2.   Simulation of ASR Velocity Reports Using Radar Measurements of Thunderstorm Outflows

In this subsection, we simulate ASR measurements of thunderstorm outflows using radar data from FLOWS operations in Hunstville, AL. Two events are considered to illustrate microburst feature variability and its impact on the detection performance of a fan-beamed ASR.

The method of simulation is similar to that employed in the previous subsection. RHI measurements of the reflectivity factor, radial velocity and spectrum width through an outflow-producing thunderstorm cell were used to calculate the velocity spectrum of echoes received by an ASR as in equation (3). For this calculation, we assumed that the shape of the power spectrum contribution from each elevation angle in the input data was Gaussian with the measured spectrum width. From the calculated spectra, pulse-pair velocity estimates were simulated as before. The procedure was repeated for successive range intervals in an RHI tilt to simulate an ASR's radial velocity measurement along a fixed azimuth through the outflow.

The outflows treated occurred within 10 km of the FL-2 radar so that vertical resolution was 175 m or better. Although the wind shear in these events was not as intense as that observed in many microbursts, the radial velocity gradient in both cases significantly exceeded $2.5 \; x \; 10^{-3} \; s^{-1}$ over a distance of several kilometers; this gradient value was used in the CLAWS program as an operational threshold for issuance of a microburst warning (8).

(a)   Case 1: 22 September 1986

Figure III-4 shows the reflectivity and radial velocity fields from a PPI scan of a thunderstorm over the FL-2 radar in Huntsville. The scan is at 0° elevation angle. The storm generated moderate rain with 40 dBZ echoes extending 3000 m above the surface. Embedded in the general outflow from the rain was an area of strong divergence centered 2-4 km east of the radar. The maximum radial velocity differential here was 13 ms^{-1} over a distance of 2.5 km.

The vertical structure of the outflow was measured with a sequence of RHI scans at the azimuth angles indicated by the overlay on Figure III-4. One of these tilts is displayed in Figure III-5. Ticks on the horizontal axis are at 2 km intervals and ticks on the vertical axis are separated by 1 km. The downdraft and approaching velocity region are essentially over the radar so that negative radial velocities were measured through much of the storm's depth at short range. The receding portion of the outflow is more typical of radar measurements of microburst winds. A shallow layer of receding flow was observed beneath a much deeper volume where scatterers moved towards the
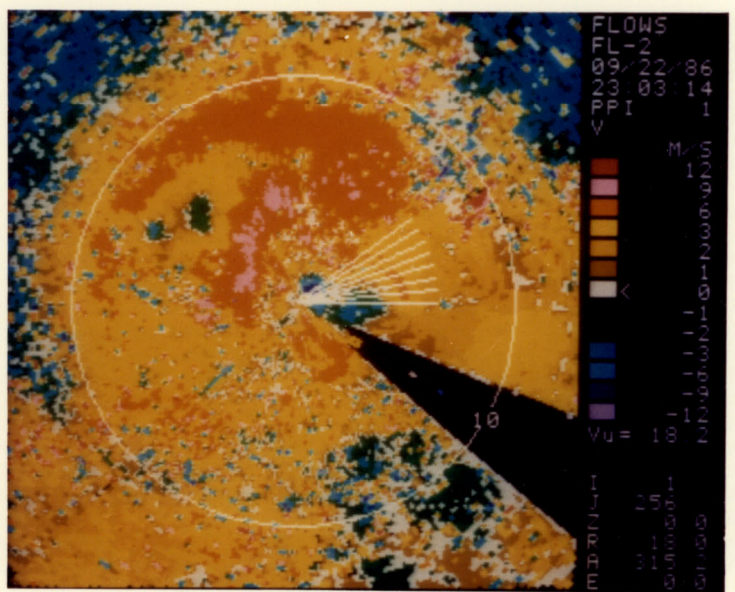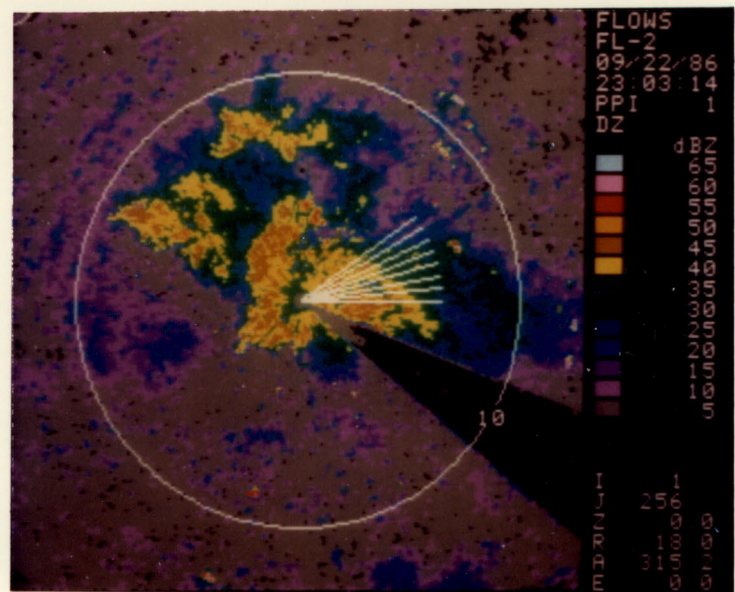
Figure III-4.   PPI scan at 0° elevation of reflectivity and radial velocity fields in a microburst near Huntsville, AL. The radial overlay lines indicate the azimuths and range extents for the ASR velocity report simulations in Figure III-6.

25
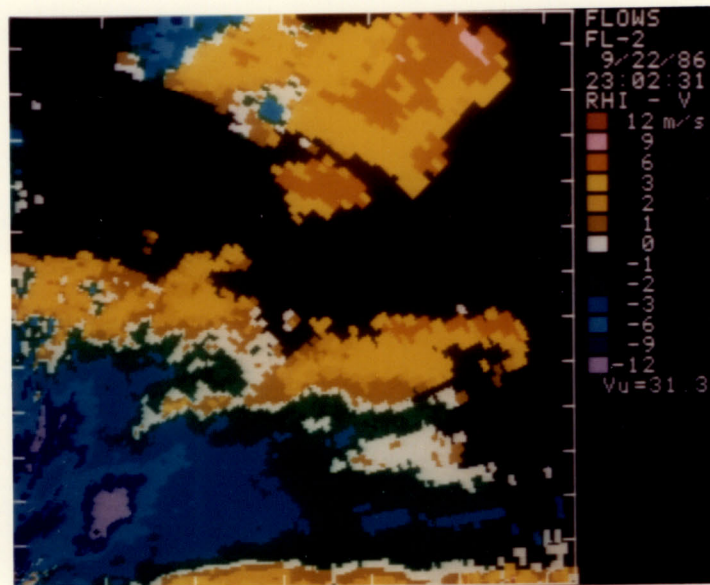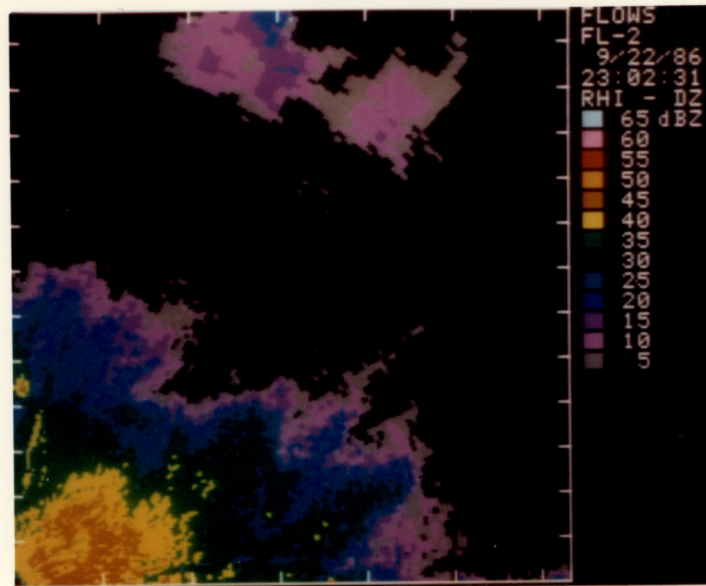
Figure III-5.   An RHI scan of the reflectivity and radial velocity field at 75° azimuth. Vertical axis ticks are at 1 km intervals and horizontal axis ticks are at 2 km intervals.

27

radar. As illustrated here and in Figure II-4, the receding air motion extended 500 m - 800 m above the surface.

Figure III-6 plots simulated velocity reports from an ASR-9 along the azimuths where RHI scans were performed. The azimuths of the RHI scans and the range extent treated in the simulations are indicated with overlays on figure III-4. The horizontal range ticks at 2 km intervals in figure III-6 are matched to those in figure III-5. Shown for each azimuth are:

(1) "truth" as given by the reflectivity-weighted radial velocity field averaged over the altitude interval 0-250 m AGL;

(2) the velocity field estimated using the pulse-pair technique applied to low-beam data from an ASR-9;

(3) the velocity field estimated using high-beam data from an ASR-9.

We have simulated a single realization of the velocity estimates assuming incoherent averaging over six successive antenna scans.

Velocities in the approaching portion of the microburst would have been accurately measured with either receiving beam of an airport surveillance radar. This results because of proximity to the radar and the depth of the approaching velocity region. The receding flow is also accurately measured with the low beam. In the high receiving beam, however, echoes from the layer of approaching precipitation overhanging the receding flow would have biased the velocity measurements by as much as 5 ms^{-1}. Along azimuths near 90° the divergent velocity signature would have been difficult to detect using the high receiving beam.

In this case, then, the microburst velocity signature would have been accurately measured by an airport surveillance radar if the ground clutter environment permitted use of the low receiving beam. Using the high beam, the divergent signature would have been measured over some but not all of the azimuthal extent of the microburst.

(b)   Case 2: 19 July 1986

A 0° elevation angle PPI display of a thunderstorm's reflectivity and radial velocity fields is shown in Figure III-7. The storm occurred slightly to the east of the FL-2 radar in Huntsville. Heavy rain produced a microburst centered 8 km from the radar with a velocity differential of 16 ms^{-1} over about 4 km.

Eight RHI scans were performed between the azimuths indicated by the overlay on Figure III-7. One of these is displayed in Figure III-8. The approaching velocity region in this microburst was extremely shallow. The height of the radial velocity zero-crossing was generally 300 m or less with an overhanging volume of positive radial velocity extending to 1.5-2.0 km AGL. The receding portion of the microburst was considerably deeper, extending about 1.0 km AGL.

Figure III-9 shows "truth" and simulated ASR velocity reports as before. The negative radial velocity region on the near side of the microburst would not have been measured with either receiving beam owing to the shallowness of the outflow layer. In spite of the greater range from the radar, an ASR would have performed better in measuring the deeper, receding microburst winds. Here, the low beam velocity estimates would have been accurate to within a few meters per second.

LAYER AVERAGE: 0-250 m   LOW BEAM   HIGH BEAM

RADIAL VELOCITY (m/s)

RANGE (km)
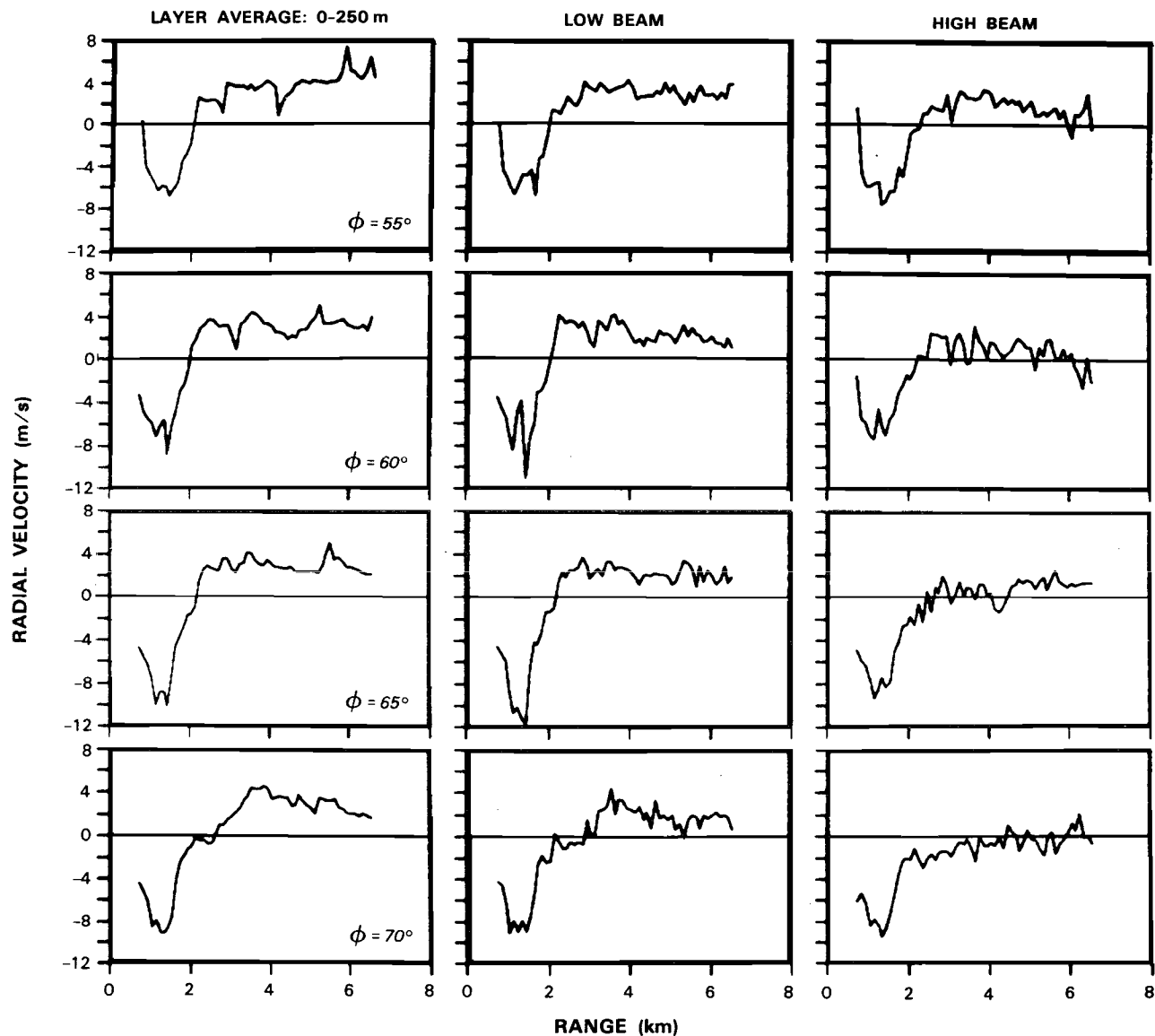
Figure III-6.   "Truth" and simulated ASR radial velocity reports for the range-azimuth intervals indicated in Figure III-4. The first column shows reflectivity-weighted, layer averaged velocities from 0 to 250 m AGL. The second and third columns plot simulated pulse-pair velocity estimates versus range using the low and high receiving beams of an ASR-9.

30

77540-13
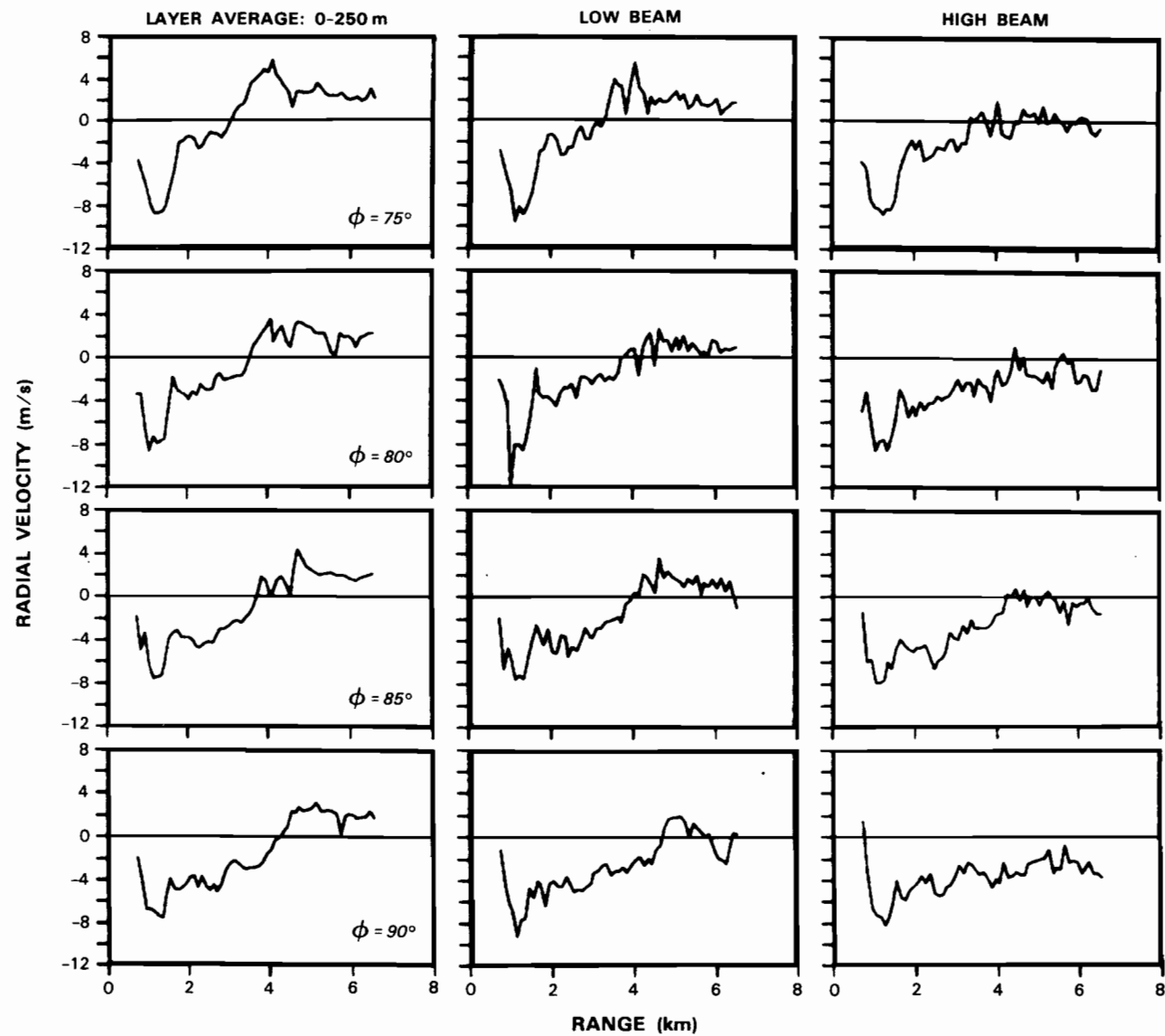
Figure III-6.   Continued.
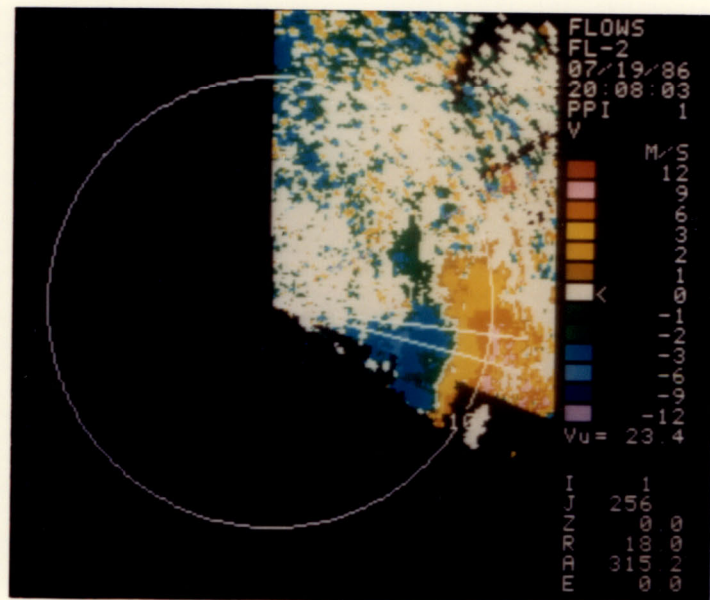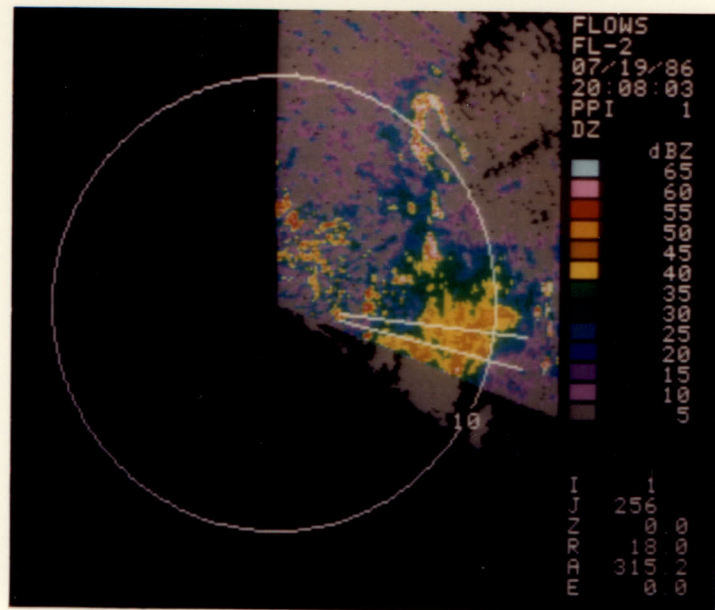
Figure III-7.   Sector scan at 0.0° elevation of reflectivity and radial velocity fields in a microburst near Huntsville, AL. The overlay indicates the range extent and azimuth interval between which the ASR velocity reports in Figure III-9 were simulated.
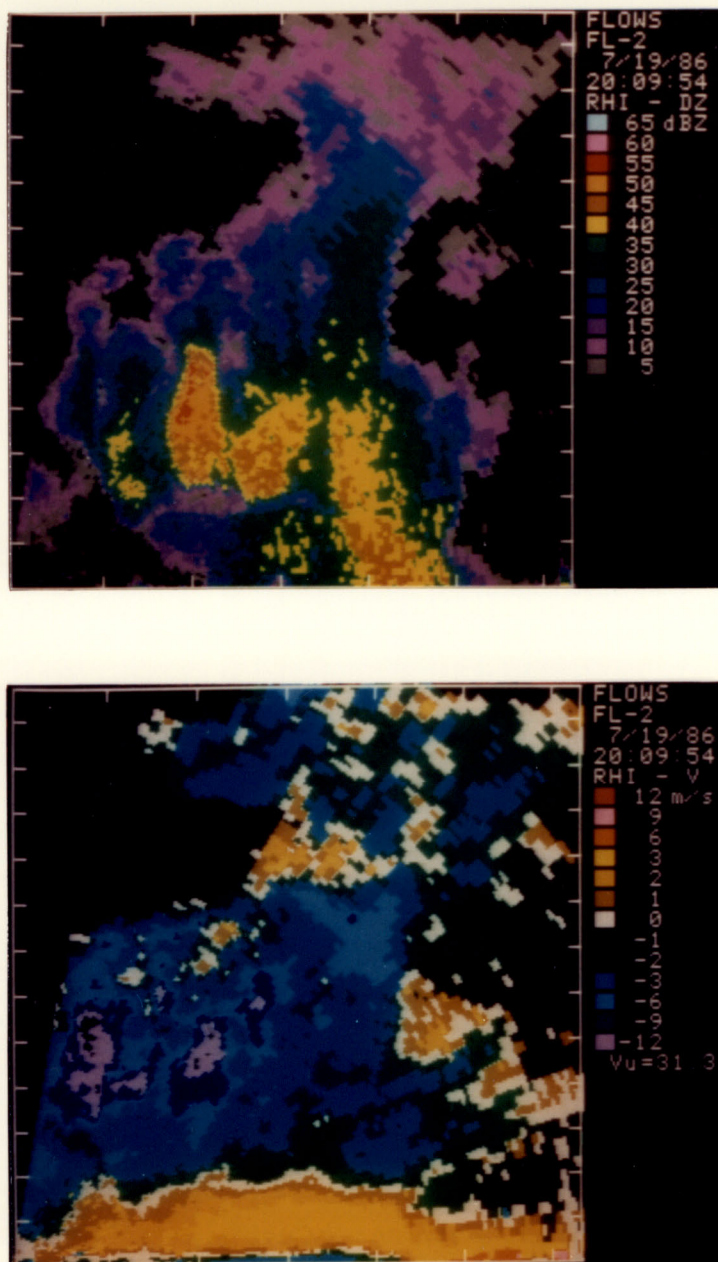
Figure III-8.   RHI scan of reflectivity and radial velocity at 101° azimuth. Vertical axis ticks are at 1 km intervals and horizontal axis ticks are at 2 km intervals.

77540-16
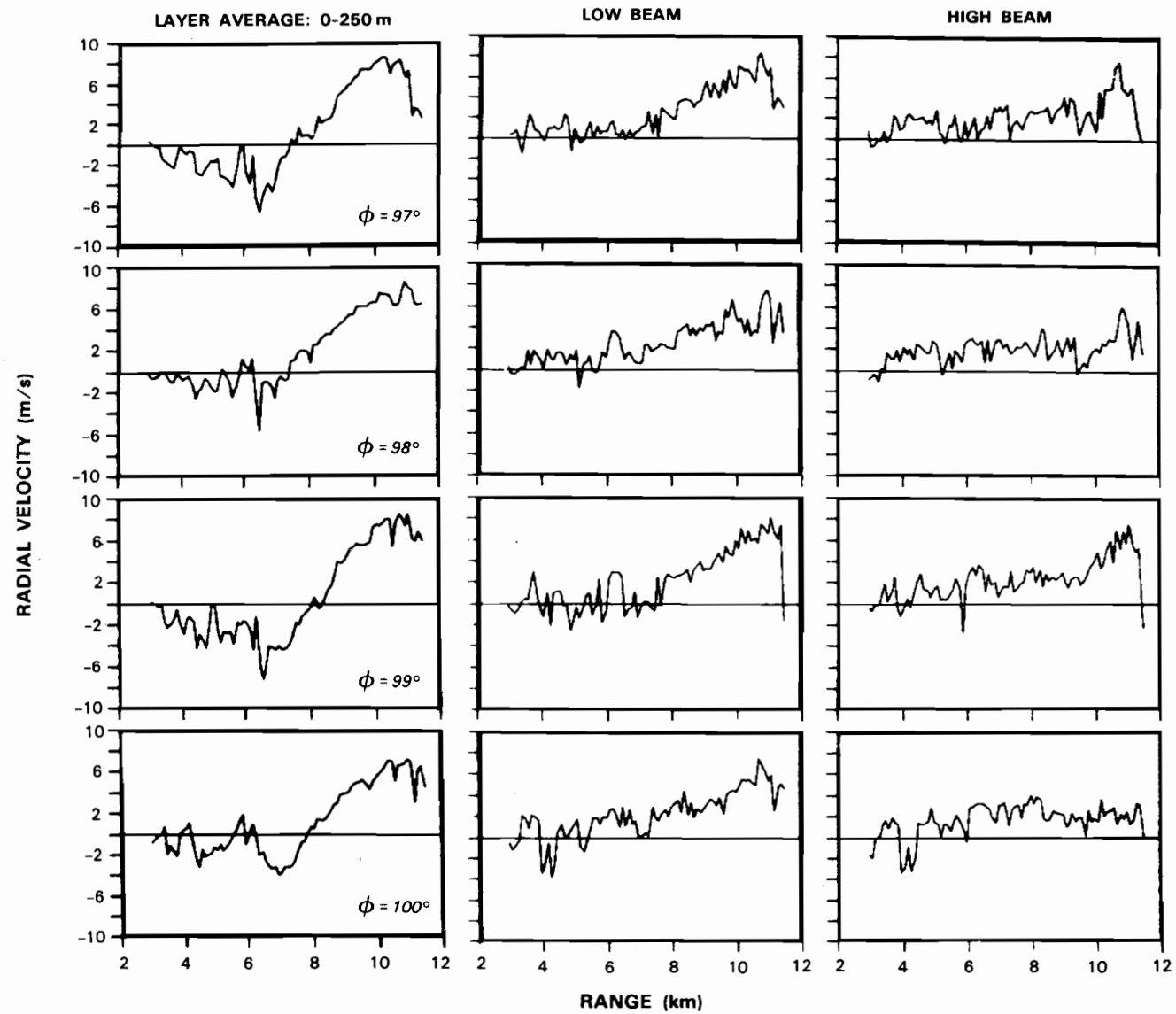
Figure III-9.   "Truth" and simulated ASR-9 velocity reports over the range-azimuth interval indicated in Figure III-7.

37
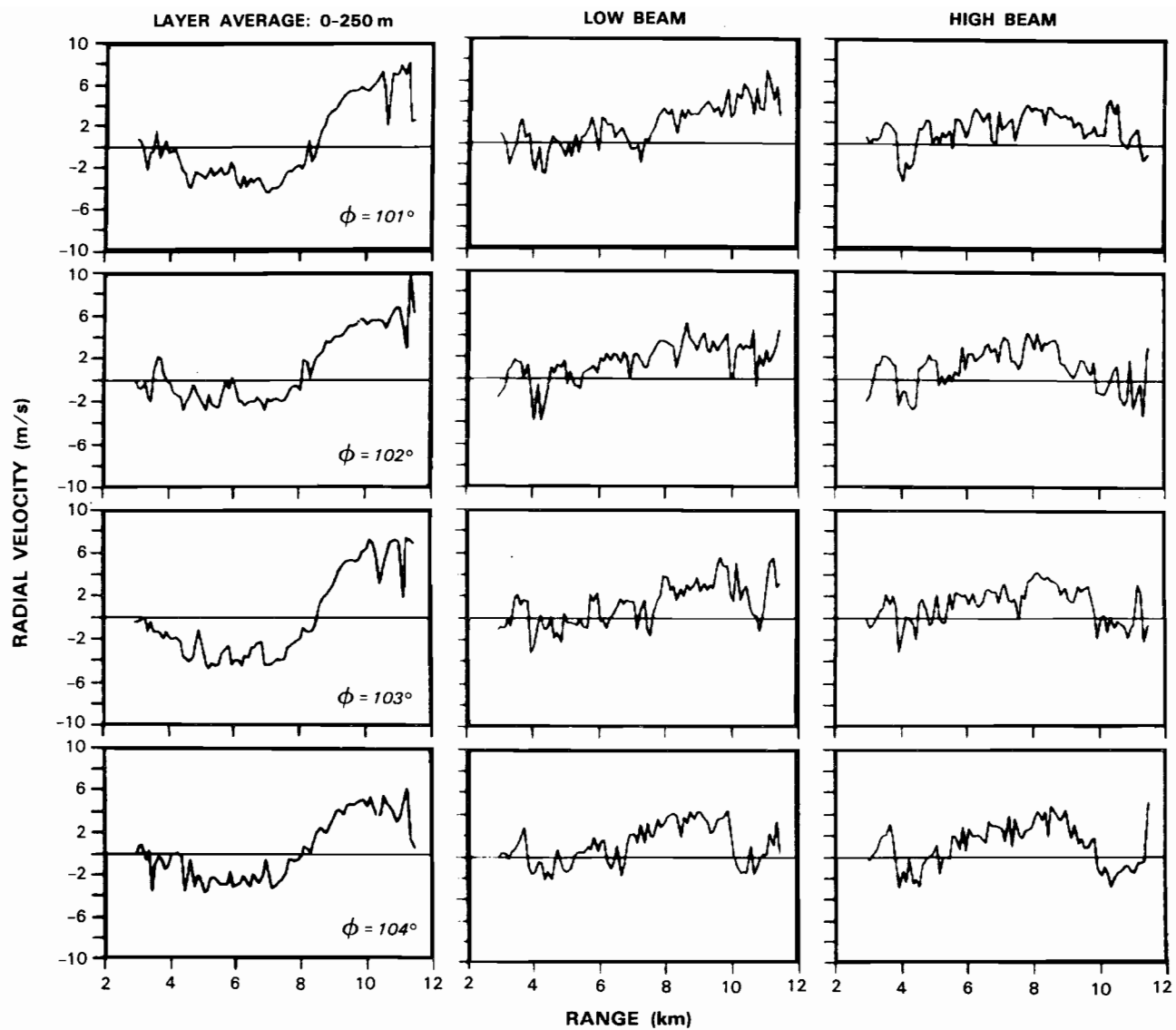
Figure III-9.   Continued.

An estimate of the velocity gradient in this microburst using ASR data would not have exceeded $1.5 x 10^{-3} s^{-1}$. This is well below the previously mentioned CLAWS operational threshold. In addition, the negative/positive velocity couplet signature of the microburst would not have been measured. This event, then, would probably have been missed if ASR measurements were relied upon. The case illustrates that extremely shallow thunderstorm outflows may be difficult to detect with an airport surveillance radar even when they occur at short range.

B. Dual Beam Measurement

One potential method for improving an airport surveillance radar's measurement of low-altitude wind shear is to utilize data from both receiving beams to: (a) "sharpen" the effective beam pattern; and/or (b) eliminate those spectral components that arise from higher altitude precipitation scatterers. The first technique implies combination of signals at the I and Q level as in a monopulse radar, whereas the second involves linear combination of power spectrum (or equivalently autocorrelation) estimates from the two beams. The potential efficacy of these approaches can be readily discerned from the beam patterns in figure II-5. Sensitivity to low elevation angle precipitation differs by 14 dB between the two beams; at angles greater than 5° however, the difference is 2 dB or less. Thus, "subtraction" of the high beam signal from the low beam signal should provide a higher degree of cancellation at large elevation angles than at small elevation angles: the effect is to increase the power ratio in equation (2).

In the remainder of this section we describe and evaluate two specific techniques for combining signals from the high and low receiving beams to extend an airport surveillance radar's detection range for shallow LAWS events. While not exhaustive, these implementations illustrate processing considerations and the magnitude of improvement that could be obtained.

As outlined in figure III-10, both approaches presume that ground clutter has been separately filtered from the two receiving channels prior to combination. In figure III-10(a), I and Q signals are combined so as to maximize the power ratio of equation (2). A pulse-pair mean velocity estimate is formed from the resulting signal. In figure III-10(b) a second "orthogonal" signal channel is synthesized that minimizes the power ratio in equation (2). Autocorrelation lag estimates are formed separately for the two receiving channels and linearly combined. Since the autocorrelation function and power spectrum are a Fourier transform pair, the intent is to cancel that part of the power spectrum that is common to the two receiving channels (i.e. scattering from high elevation angle precipitation). A pulse-pair velocity estimate is formed from the combined autocorrelation lag estimate.

For both methods, the range-dependent weights used for combining signals from the two receiving beams are determined from a model of the thunderstorm outflow. Here we will assume that the outflow extends to 500 m in height, that precipitation reflectivity is constant from the surface to 5000 m, and that reflectivity is zero at higher altitudes. An adaptive scheme for combining the two channels could probably improve performance at the expense of increased signal processing complexity. For an initial evaluation however, use of "static" weights was felt to be adequate.

1.   Coherent Combination of I and Q Signals

For both of the above methods, we require complex weights for the combination of high- and low-beam I and Q signals that maximize the power ratio of equation (2). The method illustrated
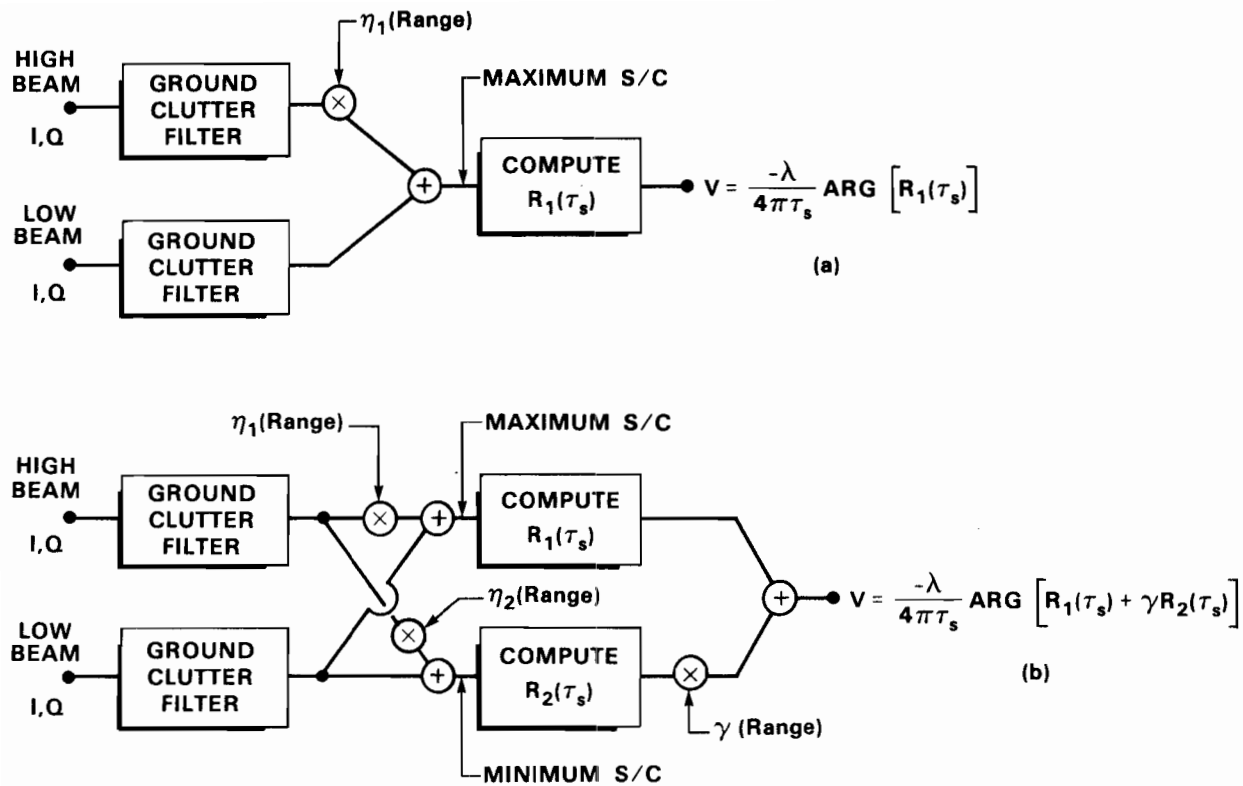
Figure III-10. Schematic of two methods for using signals from an ASR's high and low receiving beams to improve wind measurements in low-altitude thunderstorm outflows.

in figure III-10(b) requires another set of weights that minimizes this ratio. Only the difference in the amplitude and phase response of the channels is significant; without loss of generality, therefore, we can multiply only the high-beam signal by range-dependent complex weights and sum it with the low beam signal. We seek therefore extrema in the ratio:

$$\frac{P(S)}{P(C)} = \frac{\int_0^{\theta_0} Z(\theta)||\,V_1(\theta)\{\,V_1(\theta)+\eta\,V_2(\theta)\}||^2 d\theta}{\int_{\theta_0}^{\frac{\pi}{2}} Z(\theta)||\,V_1(\theta)\{\,V_1(\theta)+\eta\,V_2(\theta)\}||^2 d\theta} \tag{5}$$

As before θ_0, a function of range, is the angle subtended by the top of the thunderstorm outflow. η is the range-dependent complex weighting coefficient and $V_1(\theta)$ and $V_2(\theta)$ are the low and high antenna beam voltage patterns. The magnitude of these patterns is the square root of the solid and dotted curves in figure II-5 respectively. We incorporate the elevation-angle dependent phase difference between the channels into $V_2(\theta)$ so that $V_1(\theta)$ is taken as real. An estimate of this phase difference is plotted in figure III-11. This function was calculated by Winter (16) for an L-band air-route surveillance radar (ARSR) with vertically displaced antenna feeds. To a reasonable approximation, the geometry of his calculation scales with the difference in wavelength so that the calculated phase pattern serves as a rough model for an S-band airport surveillance radar.

40
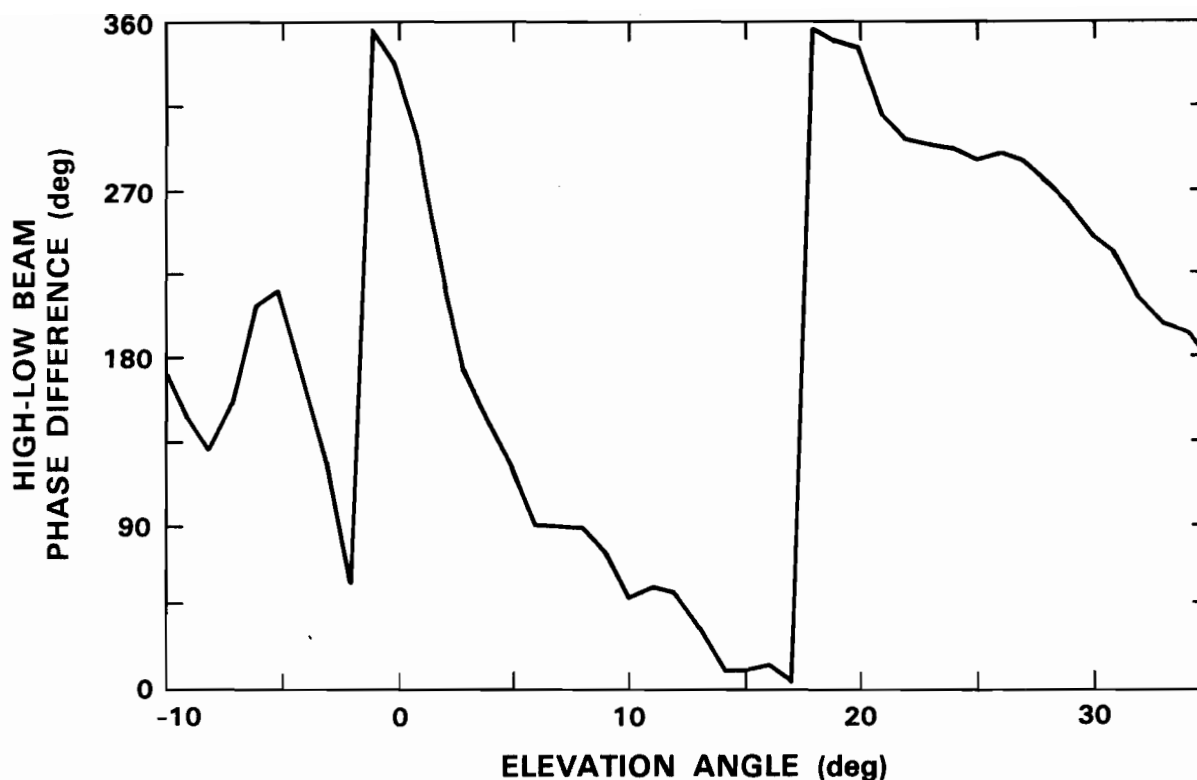
Figure III-11.   Phase difference versus target elevation angle of signals in the high and low receiving beams of a fan-beamed FAA radar.   The phase difference results from vertical displacement of the antenna feeds.   (Adapted from Winter (16).)

As shown in appendix B, the extrema of equation (5) are given by the roots of a quadratic equation whose coefficients involve definite integrals of these voltage antenna patterns, weighted by the assumed cloud reflectivity profile.   For the above assumptions concerning outflow depth and cloud reflectivity, figure III-12 shows the effective one-way power beam patterns:

$$\| V_1(\theta)\{ V_1(\theta)+\eta V_2(\theta)\}\| \tag{6}$$

for the extremal solutions, plotted at ranges of 5 km, 10 km and 15 km.   These are directly comparable with the low and high receive beam patterns plotted in figure II-5.   The angles subtended by the assumed outflow top (500 m) and the overhanging echo top (5000 m) are indicated.

Mismatch in the amplitude and phase patterns of the input beam channels severely limits the precipitation clutter rejection that can be obtained.   The maximum signal-to-interference solution typically achieves good suppression over only part of the angular interval subtended by the interfering precipitation echoes, with mainlobe overlap and sidelobes as high as -6 dB over the remainder of this interval.   The minimum signal-to-interference solution places a notch at low elevation angle in an attempt to zero power from the outflow layer.   The upper elevation limit for this notch decreases with increasing range in order to maintain sensitivity to echoes from higher altitude precipitation.

41
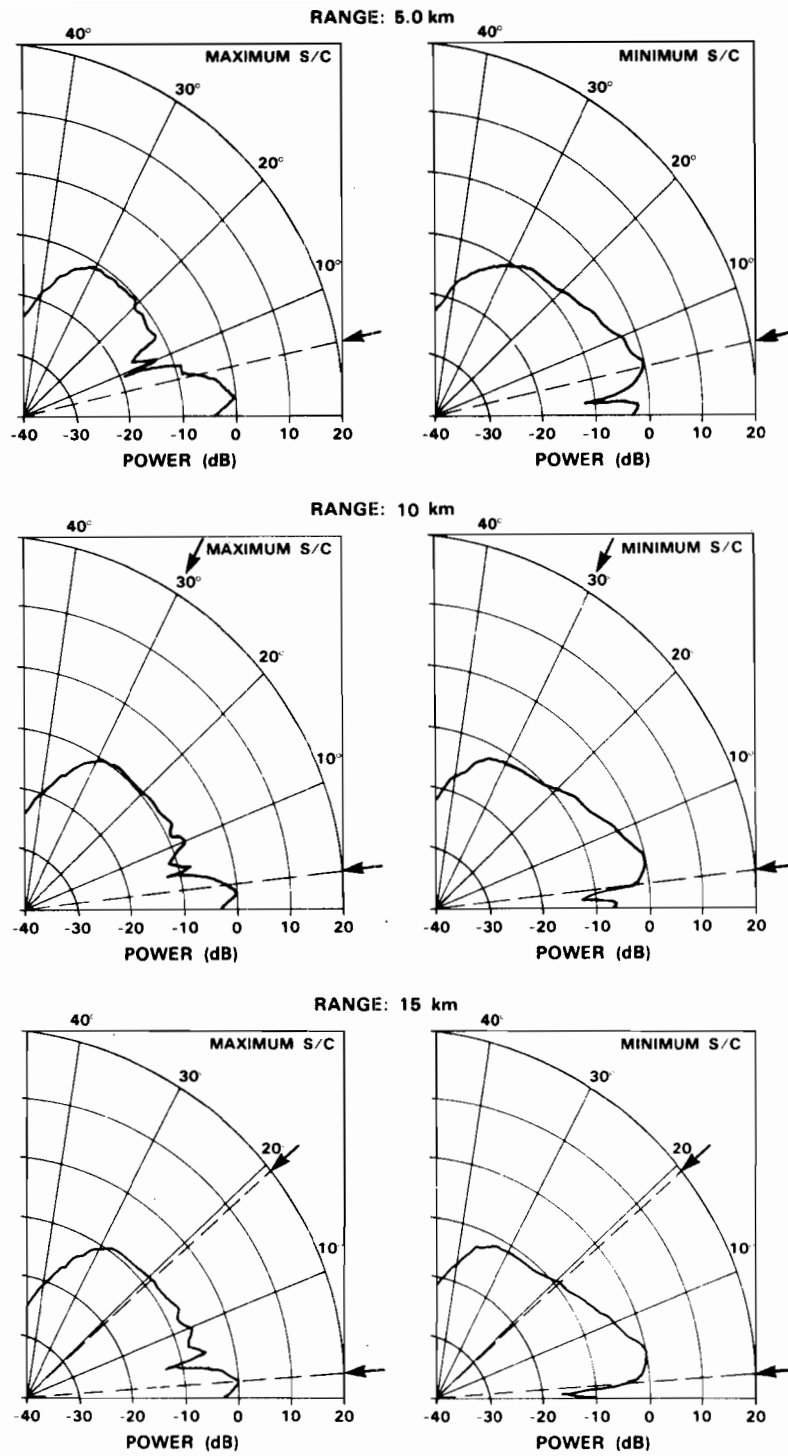
Figure III-12. Effective one-way power beam patterns for signals synthesized through coherent combination of high and low beam signals as described in the text.

Figure III-13 repeats the previous calculation (figure III-1) of signal-to-interference ratio versus range using the elevation response patterns for these two weighted combinations of high and low beam signals. Since the weights were computed for an assumed outflow depth of 500 m, the curves represent the achievable extrema only for this case. Comparison of figure III-13 and figure III-1 shows that for outflow depths of 1000 m or less, the maximum signal-to-interference weighting provides an improvement of approximately 4 dB relative to use of the low-beam signal. The range within which the power ratio in equation (5) exceeds unity increases to 7.5, 13 and 25 km for outflow depths of 300 m, 500 m and 1000 m. This represents an average increase of 30% over the range achieved by the low receiving beam, suggesting a comparable increase in detection range for shallow thunderstorm outflows. For a deeper 3000 m thunderstorm outflow, the synthesized beam pattern actually decreases the signal-to-interference ratio since the notch falls within the angular limits subtended by the LAWS event. There is still good signal-to-interference power, however, so that use of the incorrect model in computing beam combining weights should not degrade the ability to see deeper outflows.

Analogously, the signal-to-interference ratio for the minimum signal-to-interference channel is significantly lower than in the high-beam signal, particularly beyond 5 km. This will be shown to be useful for measuring the precipitation "clutter" residue in order to subtract this residue from the maximum signal-to-interference channel.

To evaluate these dual-beam outflow velocity estimators, we repeated the Monte-Carlo simulations of figures III-2 and III-3, substituting the effective dual-beam antenna patterns (equation 6) in computing the elevation angle integrated weather spectrum. The receiver noise level was raised to account for the weighted combination of uncorrelated noise in the high and low beam receivers.

Figure III-14 plots mean and one standard deviation limits for pulse-pair velocity estimates formed from the maximum signal-to-clutter channel as in figure III-10(a). As before the simulation assumes constant weather reflectivity over altitude and a 20 ms^{-1} velocity discontinuity at the top of an "outflow layer" that is varied from 300-3000 m in depth. The previously defined "detection range" is now 9 km, 14 km and 25 km for outflow depths of 300 m, 500 m and 1000 m respectively. This represents an average increase of 29% in this performance measure, relative to pulse-pair velocity estimates formed from the low beam signal. As indicated above, the synthesized beam pattern actually decreases the ratio of signal to precipitation "clutter" for a deeper 3000 m mesoscale outflow, relative to use of the low receiving beam alone. This accounts for the larger outflow velocity estimate bias beyond 10 km (compare figures III-2 and III-14). The defined detection range, however, is still greater than the 30 km range limit considered.

2.   Combination of Autocorrelation Lag Estimates

We consider next the linear combination of autocorrelation estimates from the two receiving channels as in figure III-10(b). In Appendix B we show that the appropriate weighting is:

$$\gamma = \frac{-\int_{\theta_0}^{\frac{\pi}{2}} Z(\theta) B_1(\theta) d\theta}{\int_{\theta_0}^{\frac{\pi}{2}} Z(\theta) B_2(\theta) d\theta} \tag{7}$$

Here, $B_1(\theta)$ and $B_2(\theta)$ are the two-way power beam patterns associated with the maximum and minimum signal-to-interference channels respectively. This factor is simply the ratio of precipitation "clutter" residue in the two signal channels.
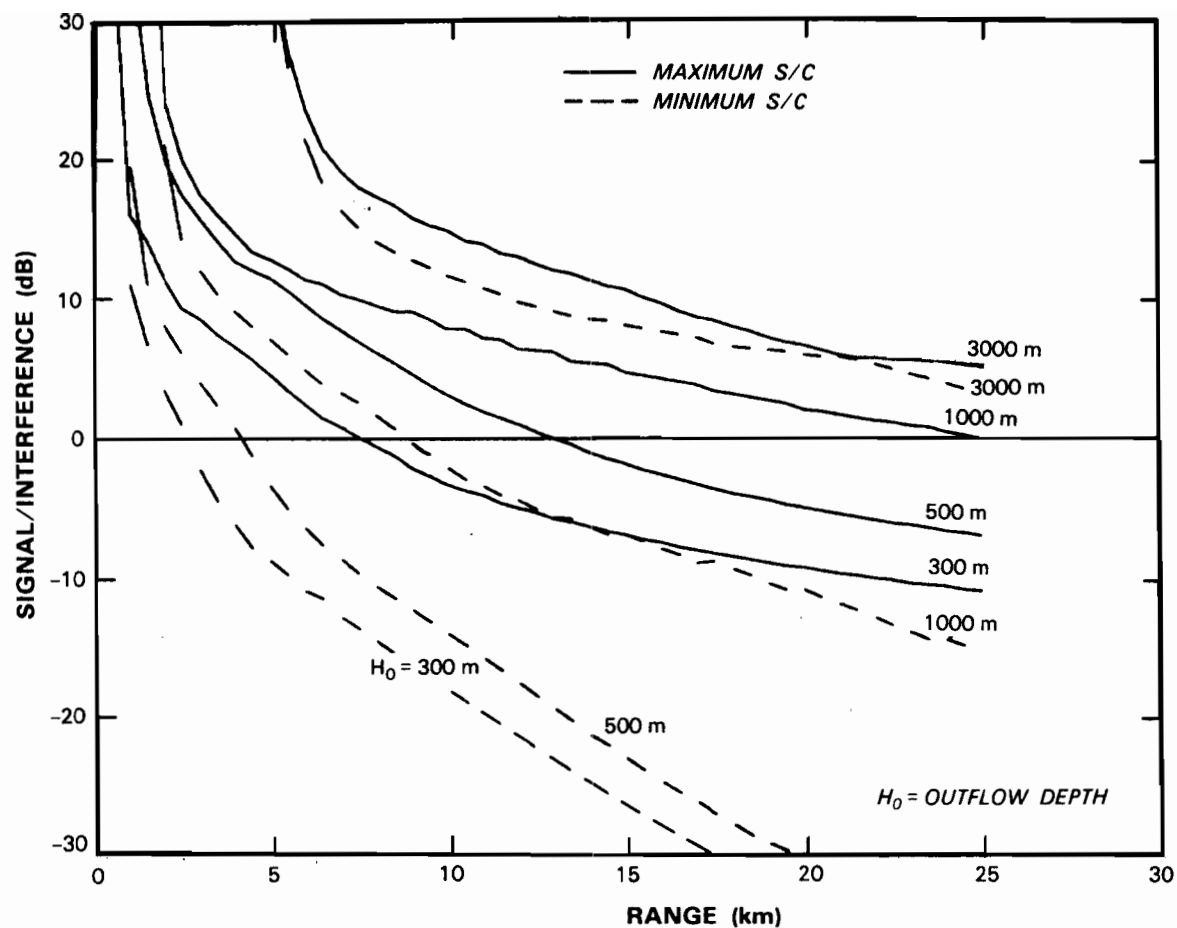
Figure III-13.   Decibel ratio of echo power from precipitation in a thunderstorm outflow layer to power scattered from precipitation above the outflow. The assumed depth of the outflow layer is indicated on each curve. The solid and dashed curves are for synthesized signals that respectively maximize and minimize the signal to precipitation interference ratio for a 500 m deep outflow.
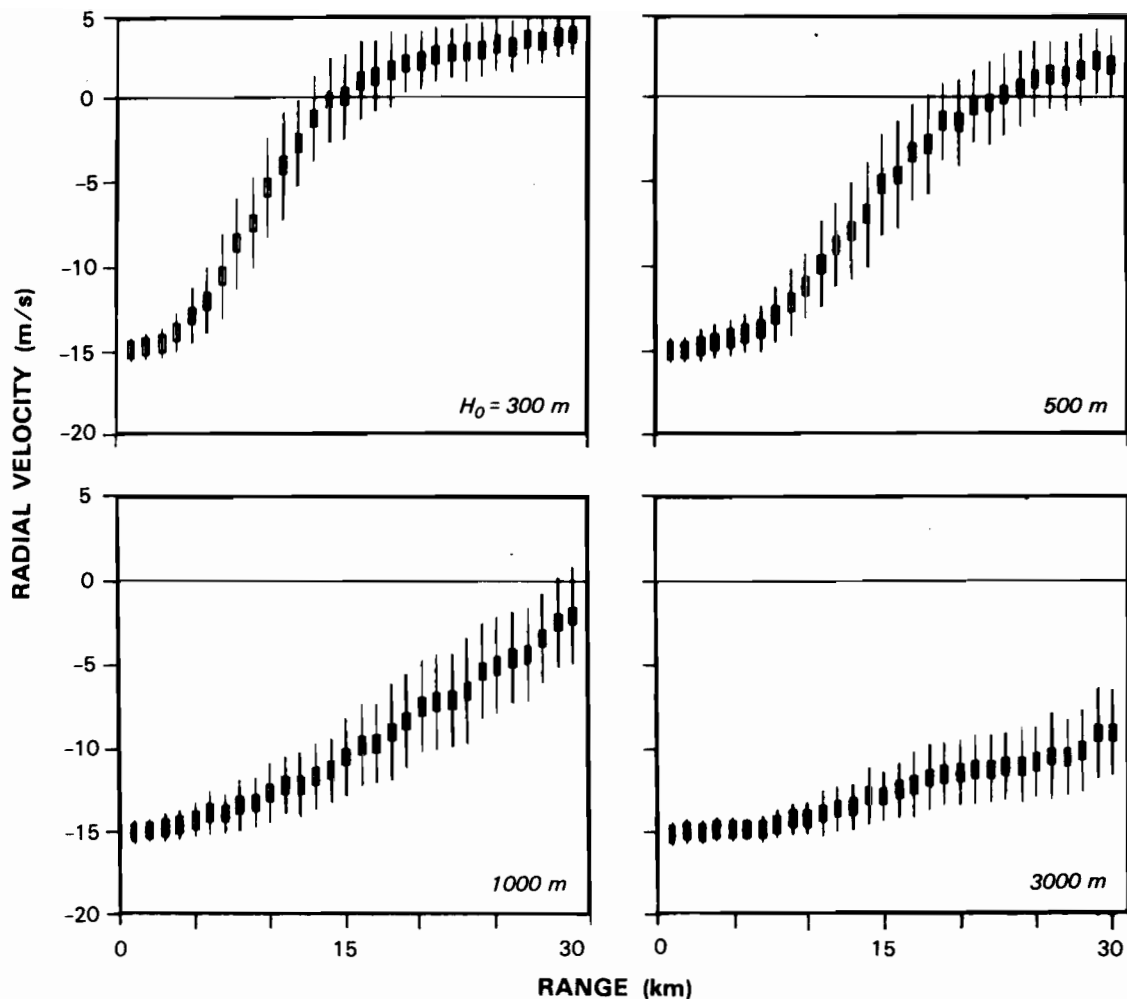
Figure III-14.   Monte Carlo simulation of mean and standard deviation of pulse-pair velocity estimates versus range. The assumptions are as in Figure III-2, except that use of the synthesized maximum signal to precipitation interference channel is assumed as in Figure III-10(a).

As previously, figure III-15 plots the mean and standard deviation versus range of velocity estimates generated using this method. The simulations were again performed using the simple thunderstorm outflow model described above with assumed outflow depths of 300 m, 500 m, 1000 m and 3000 m. The large estimate standard deviations result from the "differencing" of statistically fluctuating measured quantities.

Bias in the velocity estimates obtained with this method result from:

(a)   modeling error when outflow vertical structure does not match that assumed in computing the combining weight in equation (7);

(b)   statistical fluctuation of the autocorrelation lag estimates for the two channels which results in imperfect "clutter" cancellation even when the combining weight is appropriate.

45
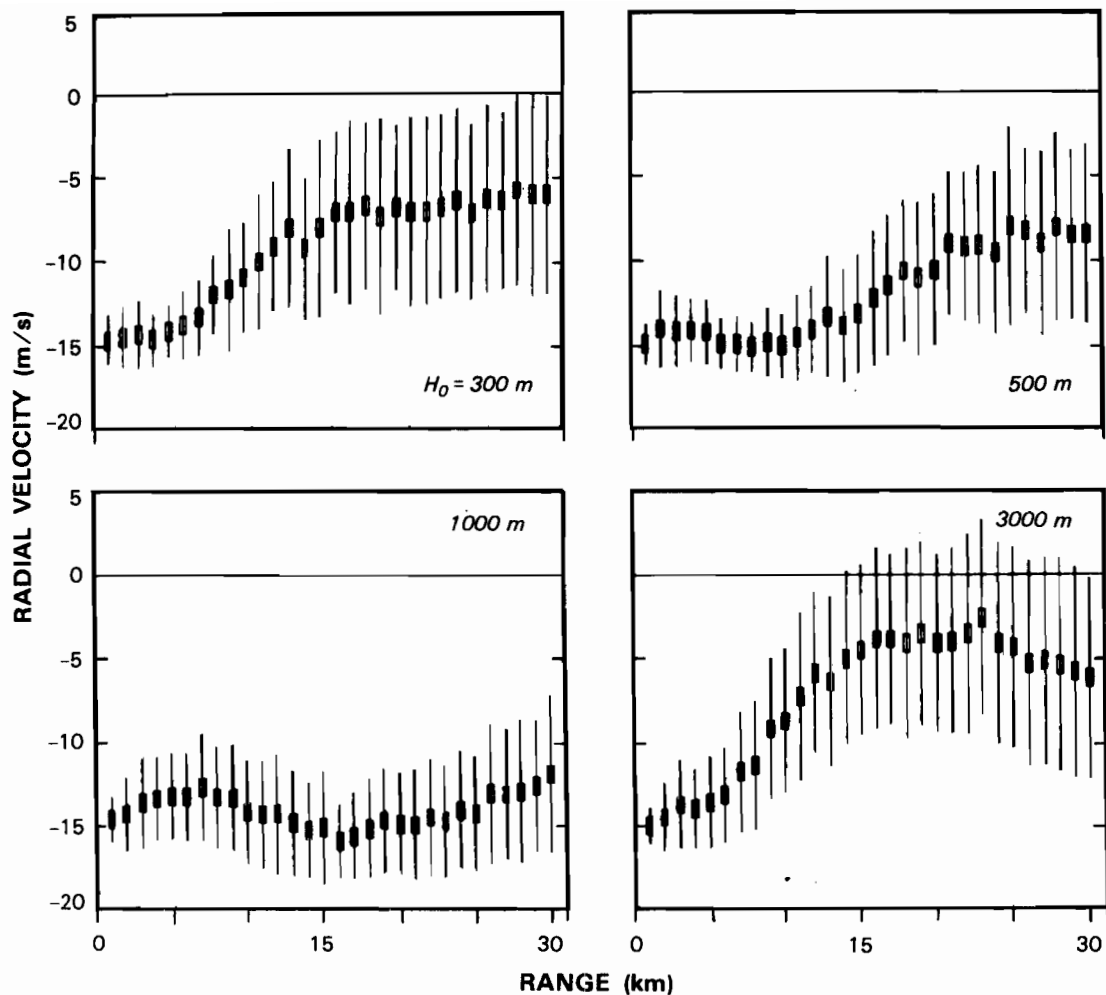
Figure III-15.   Monte Carlo simulation of mean and standard deviation of pulse-pair velocity estimates versus range. The assumptions are as in Figure III-2, except that use of the two-channel method sketched in Figure III-10(b) is assumed.

As illustrated in Appendix B, the latter effect seems to dominate for those cases where the actual outflow depth is equal to or greater than that assumed in evaluating equation (7).

Comparison of Figure III-15 with figures III-2, III-3 and III-14 shows that for outflows of depth 1000 m or less, use of the "orthogonal" signal channel results in outflow velocity estimate bias that is smaller than or equal to that achieved with either high or low beams, or the synthesized maximum signal-to-interference channel. The previously defined "detection range" is greater than 30 km for the 300 m, 500 m and 1000 m deep outflow models. For an assumed 3000 m outflow depth however, velocity estimate bias beyond 6 km range is greater than that achieved with even the high receiving beam. Analysis of the source of this error (Appendix B) indicates that it is statistical in nature, resulting from the "subtraction" of weighted autocorrelation lag estimates of approximately equal magnitude. The error could be reduced by further averaging of the single channel autocorrelation lag estimates before combination, at the expense of reduced temporal and/or spatial resolution.

46

3.   Dual-Beam Simulations with Radar Measurements of Thunderstorm Outflows

In Figure III-16 and III-17 we simulate ASR-9 velocity reports for the microburst case studies of Section III-A using both of the dual beam techniques considered in this section. A five-point moving-average filter along the range axis was used to reduce the large estimate variance associated with the two-channel approach of Figure III-10(b).

For both methods, the simulated velocity estimates for September 22 (figure III-16) correspond well to the pencil-beam radar measurements of the low-altitude wind field. Here, however, the low beam of an ASR would also have accurately measured the outflow winds (figure III-6) so that the dual-beam techniques do not provide a substantive improvement.

Outflow winds in the shallow microburst on July 19, however, would not have been well measured with either beam of an ASR used separately. Comparison of Figures III-9 and III-17 indicates that modest improvement -- relative to the low receiving beam -- would result from use of the maximum signal to interference channel alone. With the synthesized beam pattern, the shallow approaching microburst outflow would have been apparent along some azimuths and the measured radial velocity gradient would have been increased by as much as 70 percent. The resulting estimate -- $2.5 \times 10^{-3} \ s^{-1}$ -- approaches the CLAWS operational threshold but remains well below the maximum gradient measured in this microburst by the pencil beam FL-2 radar.

Use of the two-channel approach of figure III-10(b) would have resulted in unambiguous identification of the shallow approaching velocity region and therefore a clearly recognizable microburst velocity signature. Note however, that while the sign of the velocity measurements would now indicate the presence of a microburst, wind speed in the approaching region of the outflow would be significantly overestimated in many gates. Since pilots require quantitative information on microburst wind shear, the two-channel measurements simulated here would probably be inadequate for operational usage.

We conclude that:

(a)   signal combination on the I,Q level to synthesize a more favorable beam pattern results in only modest improvement in thunderstorm outflow wind measurement, relative to data from the low receiving beam alone. Mismatch in the amplitude and phase responses of the two receiving beams limits the extent to which interference from overhanging precipitation can be rejected. Our simulations indicate that the range to which shallow outflow winds could be accurately measured would be increased by roughly 30 percent using this method;

(b)   use of a second synthesized signal channel to measure and "cancel" the overhanging precipitation interference residue might provide a more substantial improvement in the ability to measure outflow winds. The simple implementation considered here, however, would not produce consistently reliable measurements owing to the use of static combining weights in highly variable thunderstorm outflow environments and to statistical uncertainties in the autocorrelation lag estimates used for the cancellation procedure. Future work will investigate whether data-adaptive methods for combining information from the two signal channels would provide more robuste measurements of outflow winds.
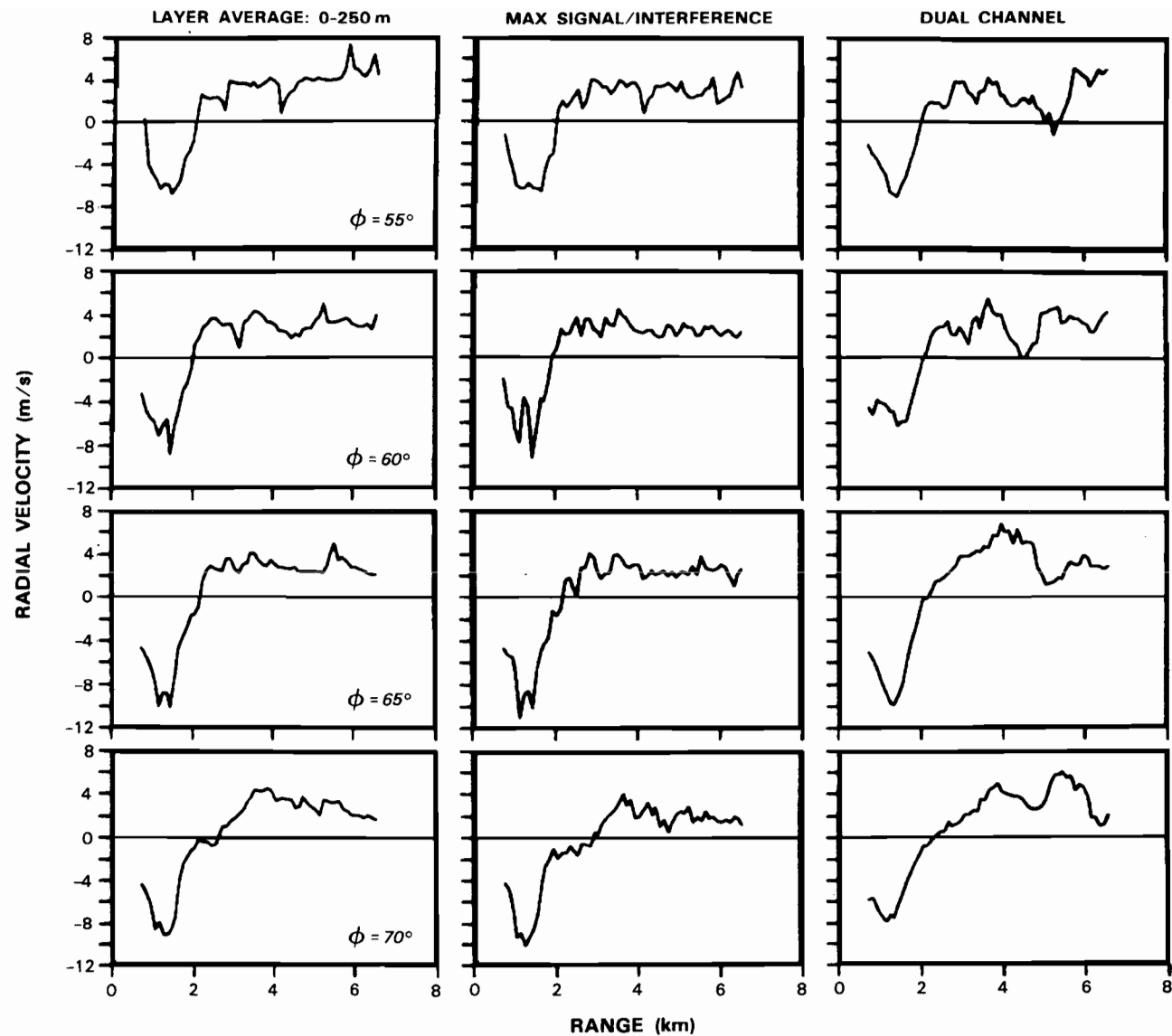
Figure III-16. "Truth" and simulated dual-beam velocity reports for the microburst treated in Figures III-4 to III-6. The second column plots simulated ASR-9 velocity reports using the method of Figure III-10(a) and the third column simulates the method of Figure III-10(b).
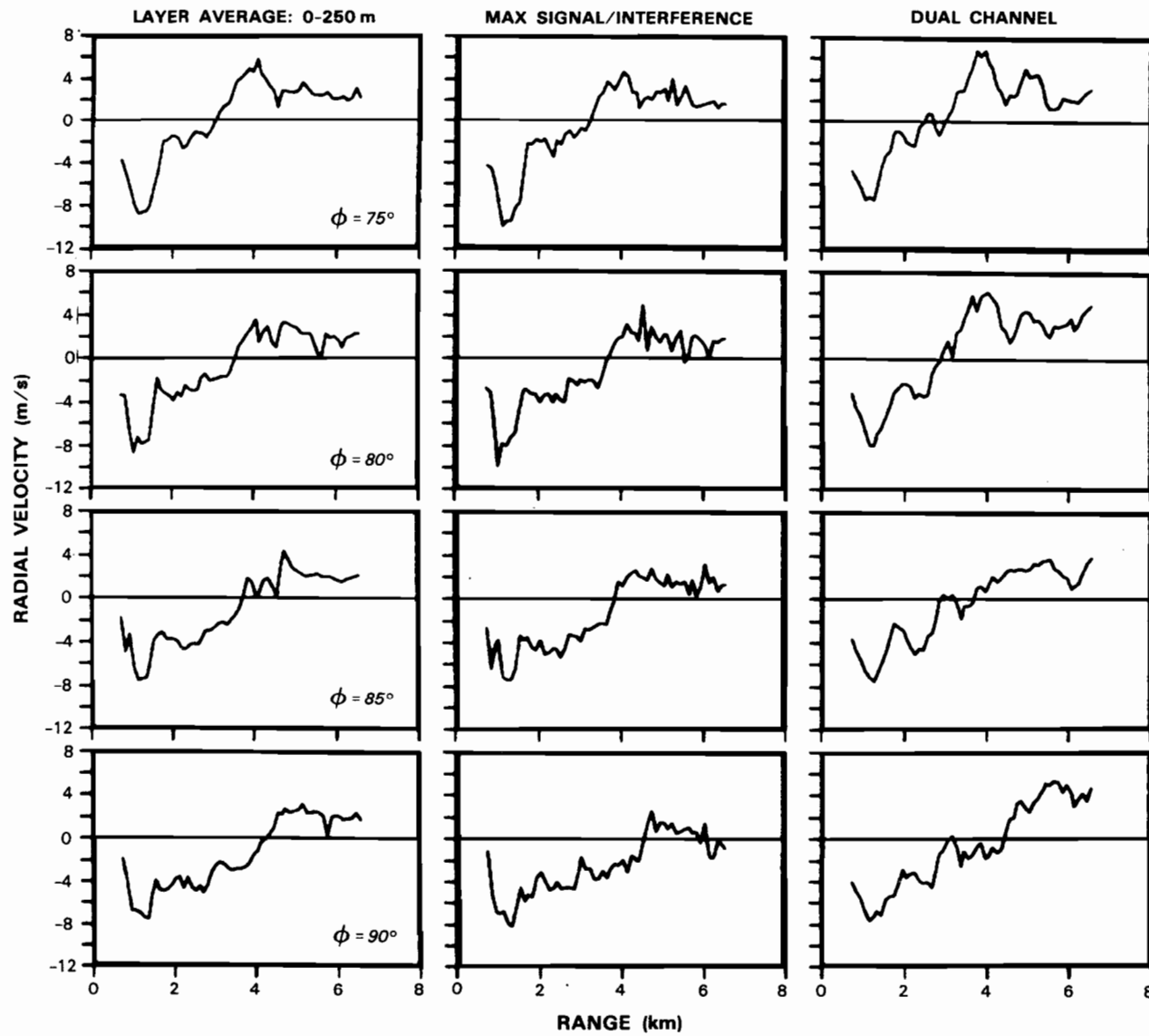
Figure III-16.   Continued.
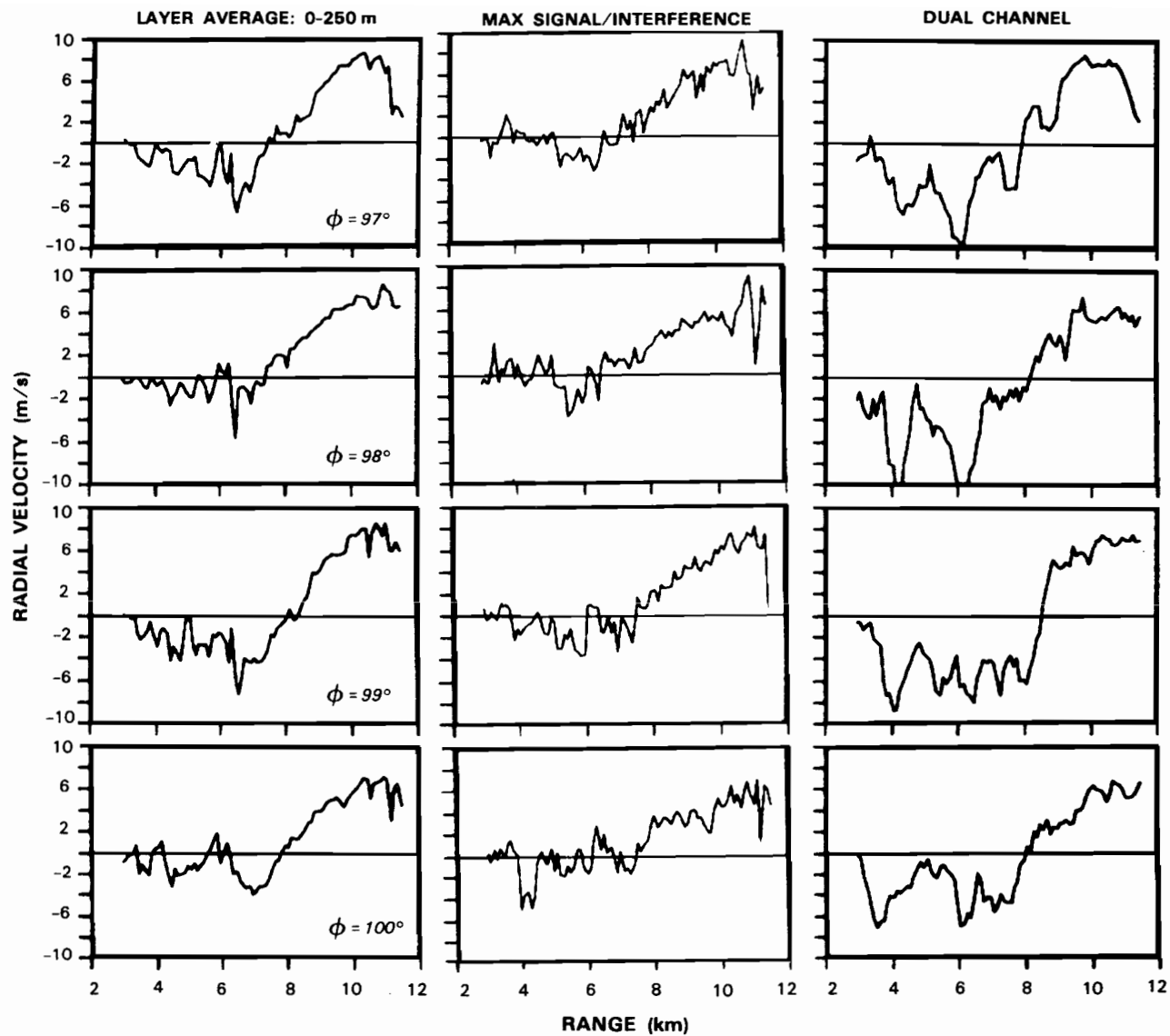
Figure III-17.   "Truth" and simulated dual-beam velocity reports for the microburst treated in Figures III-7 to III-9.

LAYER AVERAGE: 0-250 m   MAX SIGNAL/INTERFERENCE   DUAL CHANNEL

$\phi = 101°$

$\phi = 102°$

$\phi = 103°$

$\phi = 104°$

RADIAL VELOCITY (m/s)

RANGE (km)
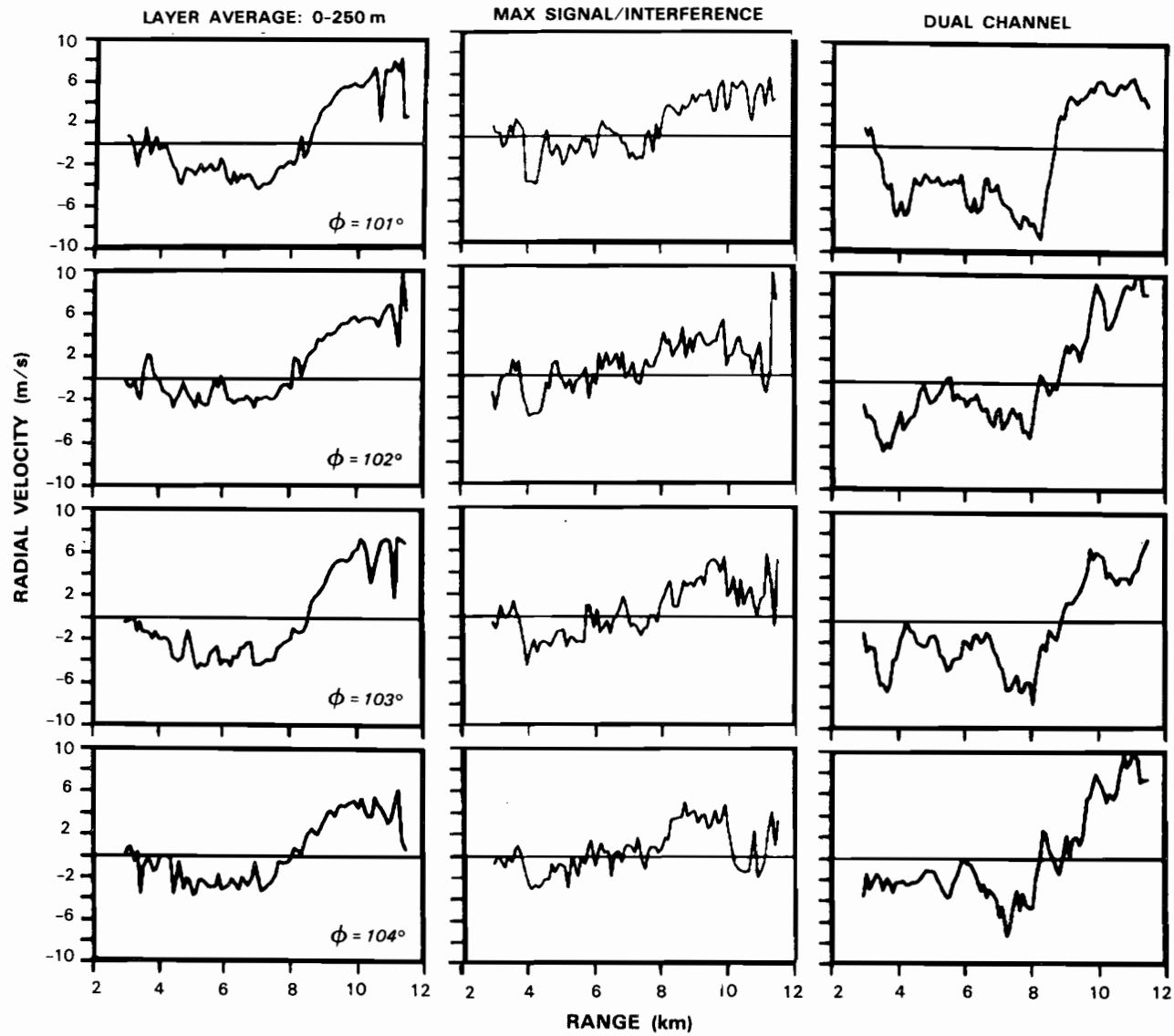
Figure III-17.   Continued.

IV. GROUND CLUTTER

The desirability of using low-beam data in the critical region near an airport means that ground clutter will be an important factor in limiting the LAWS detection capability of an airport surveillance radar. To quantify its impact, we have examined ground clutter recordings from operational ASR-8s at Memphis International Airport and at Stapleton Airport in Denver. Appendix C describes the clutter recording system and the data reduction procedure used to compute resolution cell averaged received power or, equivalently, the clutter cross-section density σ_0. The resolution of the reduced clutter data is 140 m in range by 1.4° in azimuth.

Figure IV-1 plots the clutter returns in a PPI format. The data have been scaled to an equivalent weather reflectivity factor using equation A-1 in Appendix A. Clutter in the high and low receiving beams are displayed separately for each site. Histograms of ground clutter intensity -- likewise in units of equivalent weather reflectivity factor -- are plotted in figure IV-2 for the range intervals 0-10 km, 10-20 km and 20-30 km. The upper abscissa labels give the corresponding cross-section density scale for the midpoint of each range interval. Figure IV-3 shows the median clutter reflectivity factor (ensembled over azimuth) as a function of range.

Intense ground clutter at the Memphis site extended in a wedge northwards from the radar and was associated with gently upsloping, tree-covered terrain in the suburbs of Memphis. The maximum equivalent weather reflectivity factor exceeded 65 dBZ in the low beam with values greater than 40 dBZ measured over much of this area. In the low beam, less than 1% of the resolution cells within 10 km of the radar were noise limited.

For comparison, Figure IV-4 sketches the runway layout at Memphis airport. The airport has three instrumented runways, two oriented north-south and one oriented east-west. Secondary runways are oriented north-northeast to south-southwest and northwest to southeast. Aircraft approaching from the northern sector on a 3° glide-slope would drop below 500 m at a range of 9.5 km. Thus, throughout the last stages of approach where low-altitude wind shear is a real danger such aircraft would be over intense ground clutter. Conversely, aircraft approaching the east-west runways or from the southern sector would generally be over weaker ground clutter until the final few kilometers.

Three areas of intense ground clutter were measured with the Stapleton (Denver) ASR-8. These were: (i) at ranges less than 5 km from the radar; (ii) an area to the north-northwest at 15-25 km in range; and (iii) in the southwestern quadrant at 25-35 km in range. The second area is an urban region slightly elevated with respect to the airport and the third corresponds to higher hills to the west of Denver. Equivalent weather reflectivity factors within these regions were again frequently greater than 40 dBZ with maxima exceeding 65 dBZ.

As sketched in Figure IV-5, Stapleton airport has four major runways, two oriented east-west and two oriented 10 degrees clockwise from north-south. Three of the four runways are equipped for instrumented landings. The principal approach directions intersect regions of intense ground clutter only to the west at ranges greater than 30 km and within 5 km of the radar. Thus, from the viewpoint of low altitude wind shear detection, vulnerable aircraft at low altitude would be over severe competing ground clutter only within 5 km of the ASR-8.

HIGH BEAM
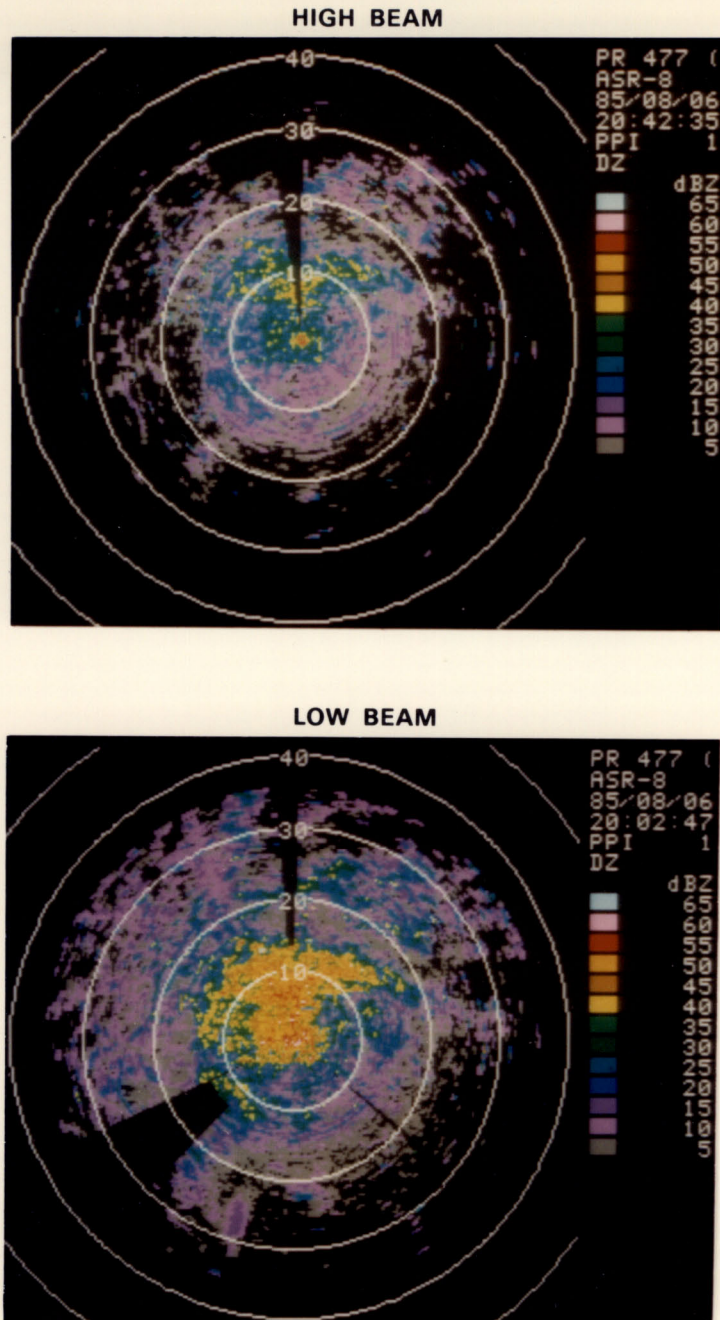
LOW BEAM

Figure IV-1a.   PPI display of ground clutter returns from the ASR-8 at Memphis International Airport. High and low beam returns are shown separately. Received power is scaled to represent the equivalent weather reflectivity factor using a filled-beam assumption.

HIGH BEAM

LOW BEAM
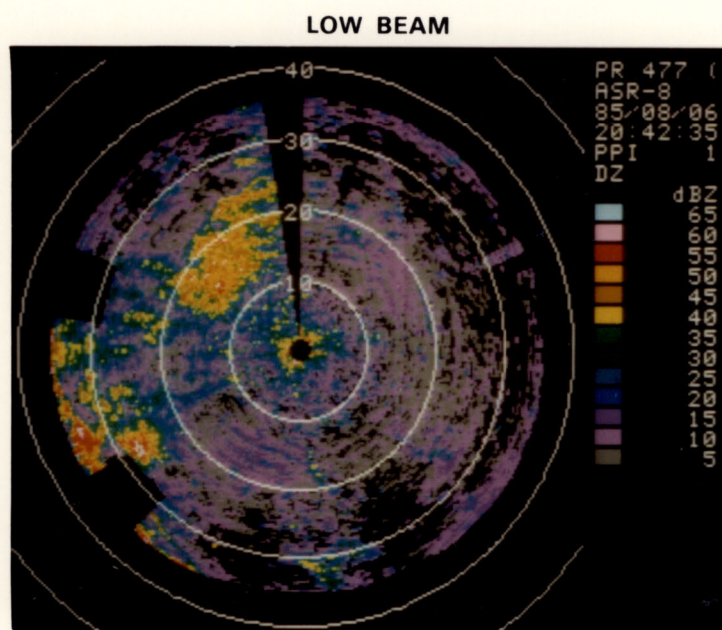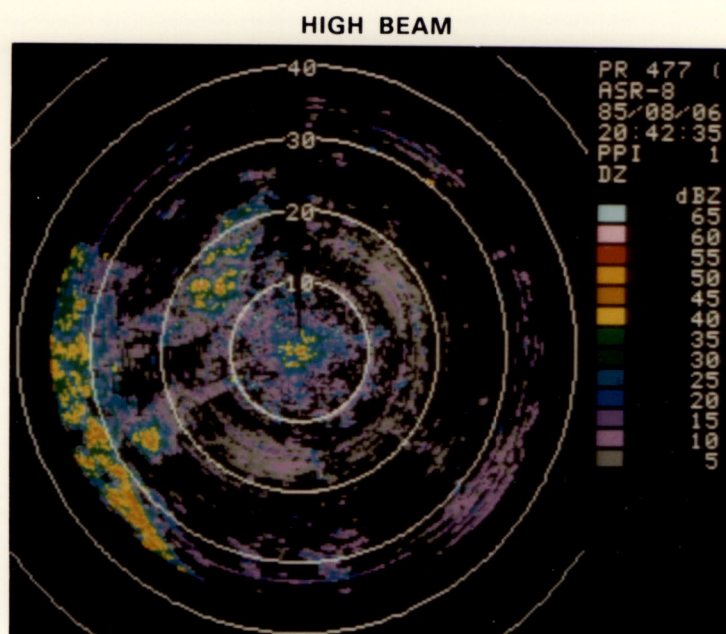
Figure IV-1b.   PPI display of ground clutter returns from the ASR-8 at Stapleton Airport in Denver.

77540-26

57

ASR-8 MEMPHIS LOW BEAM
CLUTTER CROSS SECTION DENSITY (dB//1 m²/m²)

ASR-8: MEMPHIS HIGH BEAM
CLUTTER CROSS SECTION DENSITY (dB//1 m²/m²)
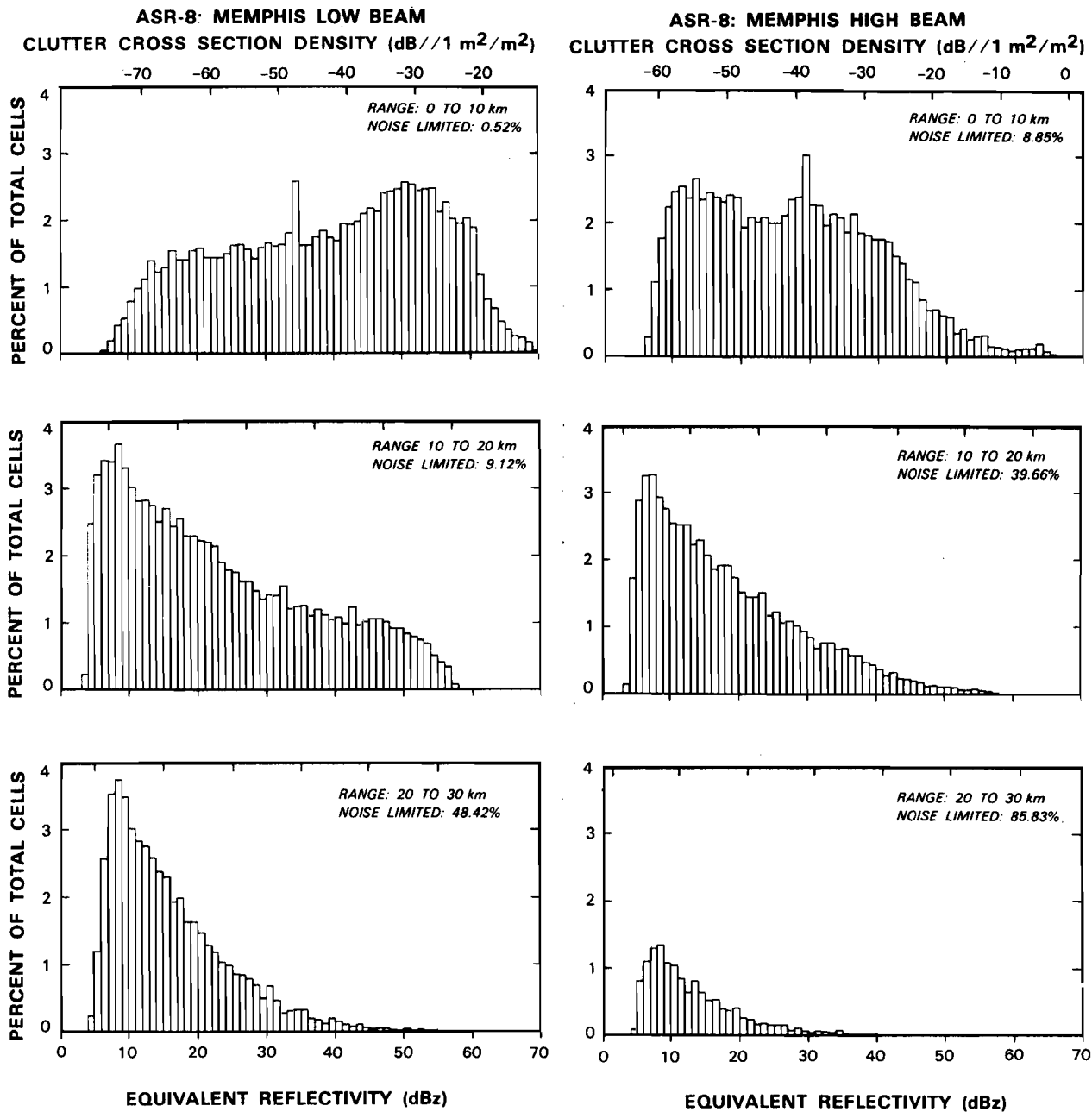
Figure IV-2a.   Histograms of ground clutter intensity at the ASR-8 at Memphis International Airport. Separate histograms are shown for both receiving beams and for each of three range intervals. The data are scaled to an equivalent weather reflectivity factor (dBZ). Upper abscissa label is the corresponding clutter cross-section density, σ_0, at the midpoint of the range interval considered.
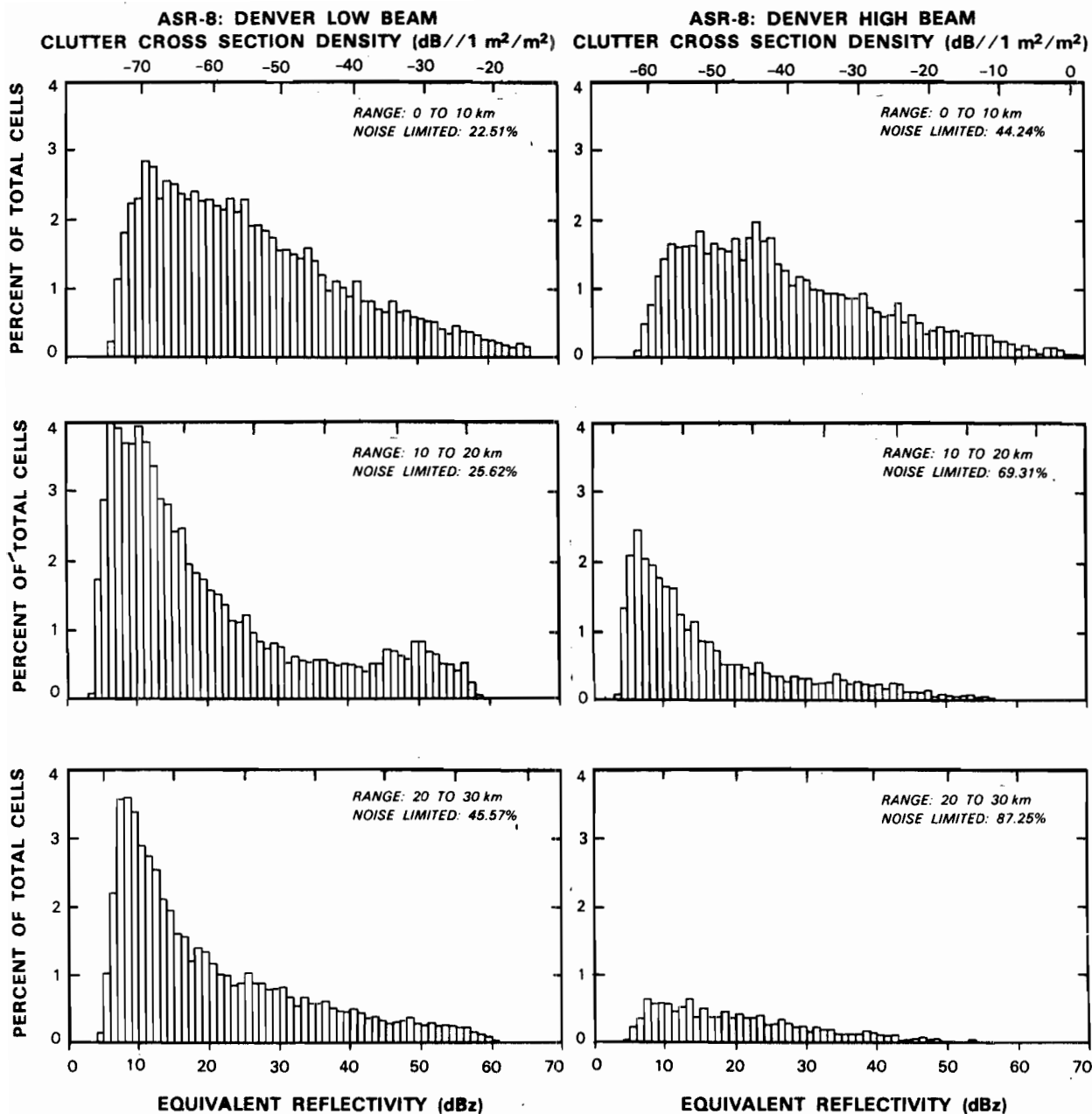
Figure IV-2b. Histograms of ground clutter intensity at the ASR-8 at Stapleton Airport in Denver.
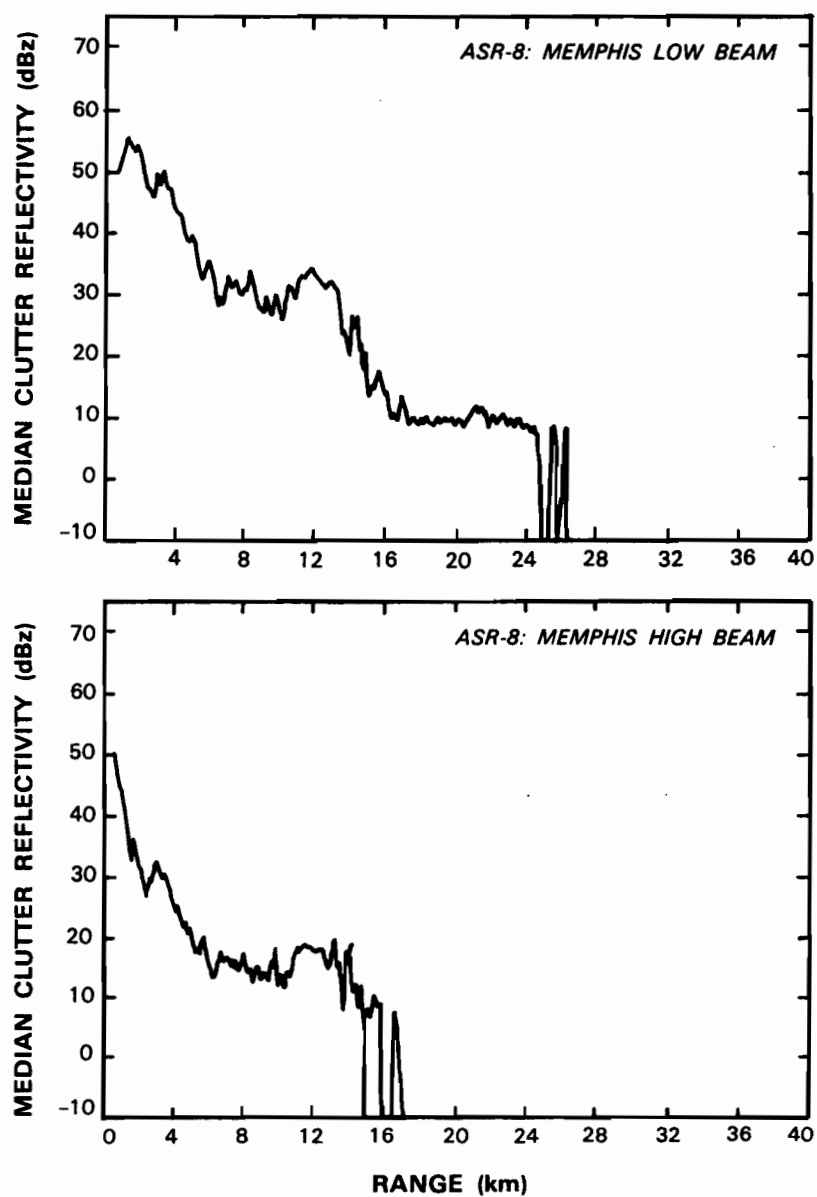
Figure IV-3a.   Median ground clutter intensity (ensembled over azimuth) versus range for the ASR-8 at Memphis International Airport.
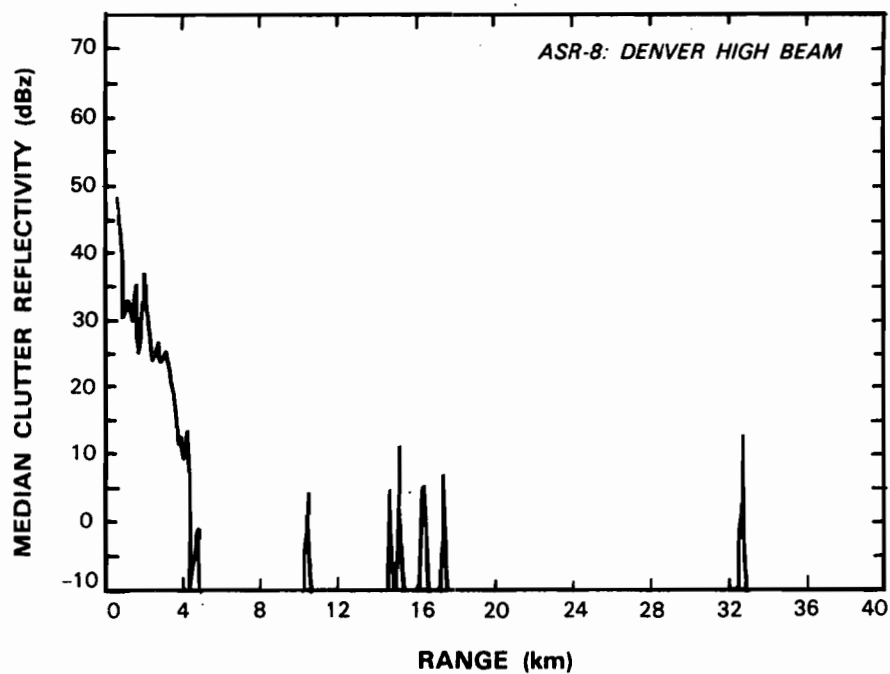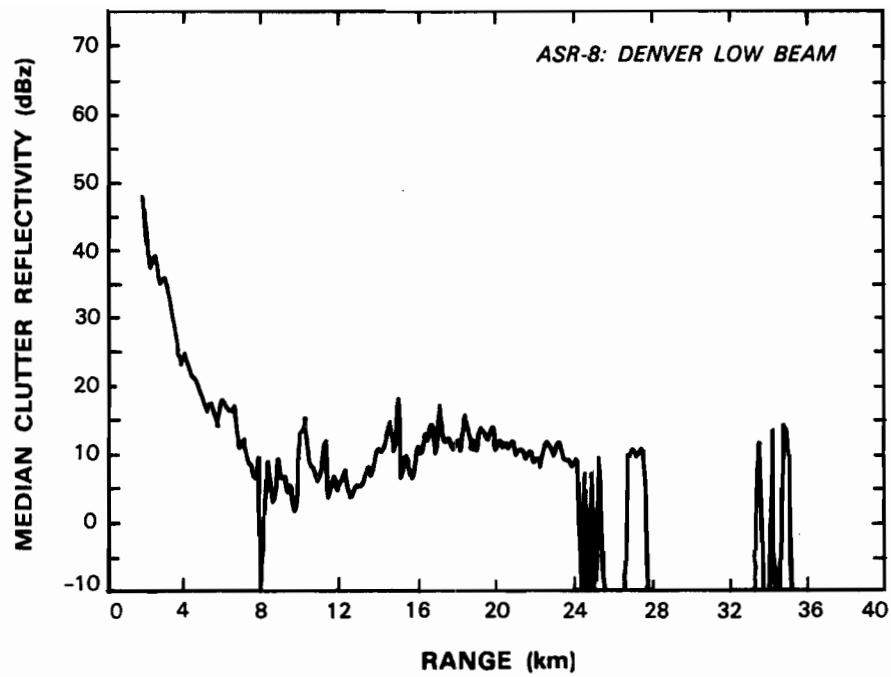
Figure IV-3b. Median ground clutter intensity (ensembled over azimuth) versus range for the ASR-8 at Stapleton Airport.

62

Figure IV-4. Runway layout at Memphis International Airport.

63
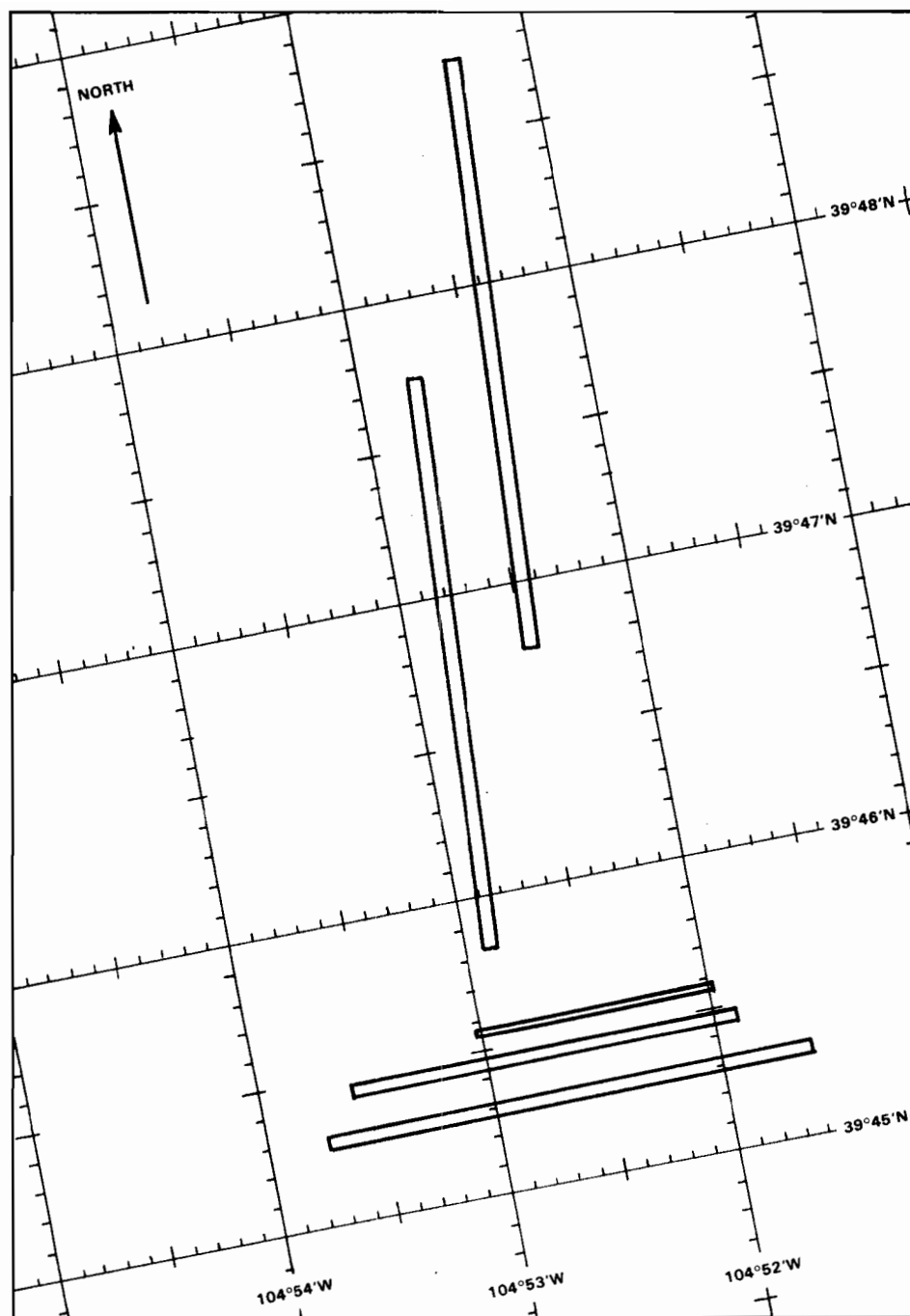
Figure IV-5.   Runway layout at Stapleton Airport.

77540-32

At short range, the upper dynamic range limit for these clutter measurements is greater than would apply if the $(R/23km)^2$ STC function suggested for wind shear detection in Section II was used. Thus we can compute the fraction of resolution cells where ground clutter would result in receiver clipping if the suggested STC function was used. As a function of range, the fraction of azimuthal cells where clipping would occur is plotted in Figure IV-6. At Memphis, both receiving channels would be clipped at almost all azimuths within about 500 m of the radar. Even in the low beam however, the percentage of azimuth cells that would be clipped drops below 20% beyond 1 km in range. No clipping would occur beyond 4 km. At Denver, a setup error for the recording system resulted in loss of low-beam data within 2 km of the radar. From 2 km to 4 km less than 10% of low beam resolution cells would be clipped and no clipping would occur at greater ranges. We conclude that in these clutter environments, an STC function that provides adequate sensitivity for detection of wind-shear associated with low reflectivity echoes (5 - 20 dBZ) could be employed in both receiving beams of an airport surveillance radar. More attenuation than considered would obviously be required for the first few range gates but loss of sensitivity at short range is not as critical since beamfilling loss is negligible.
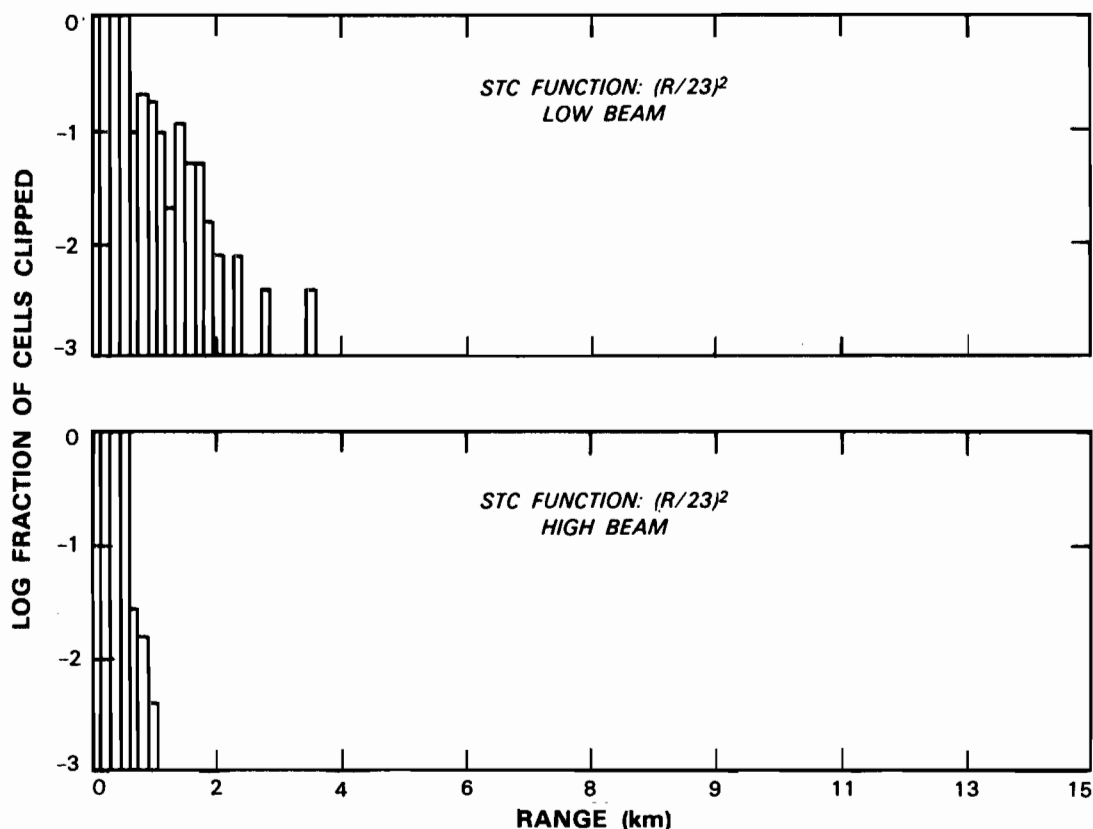
Figure IV-6a.   Probability of receiver clipping (ensembled over azimuth) versus range for the ASR-8 at Memphis. As discussed in the text, an $(R/23km)^2$ STC function is assumed.
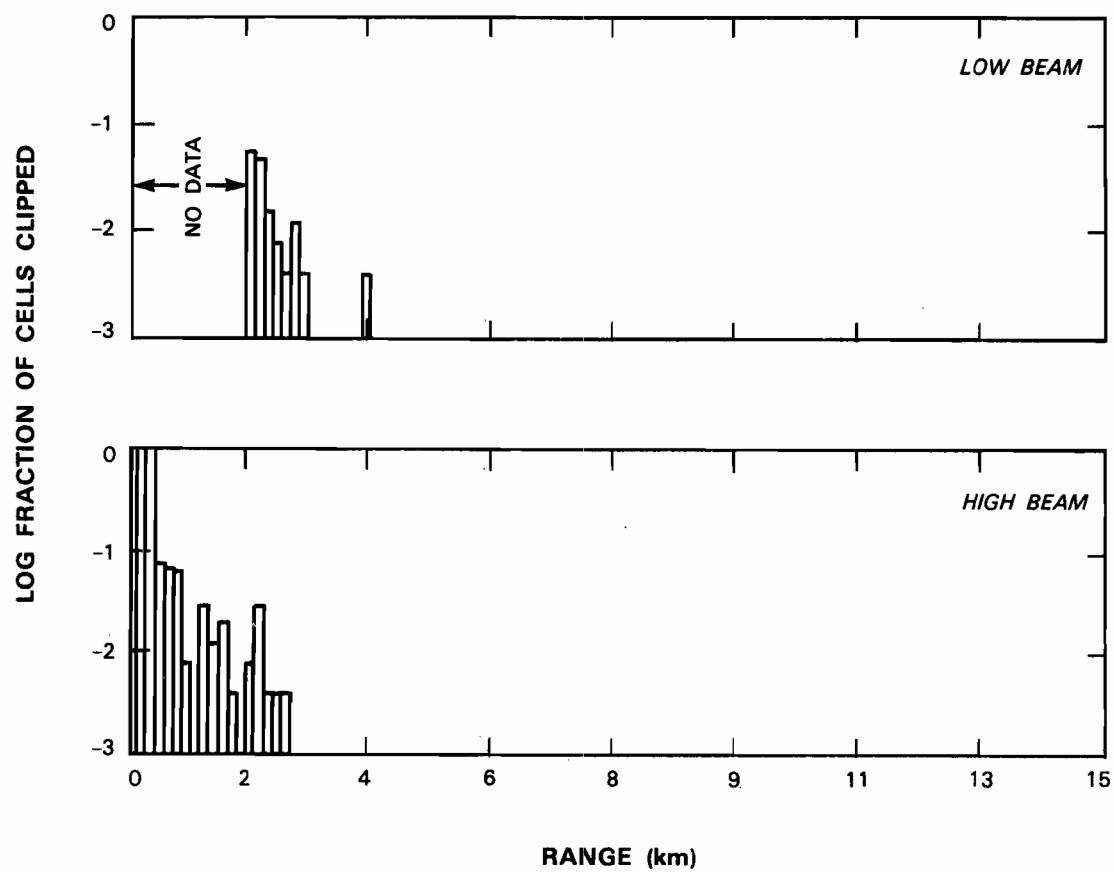
Figure IV-6b.   Probability of receiver clipping versus range for the ASR-8 at Denver, assuming an $(R/23km)^2$ STC function.

As with the precipitation "clutter" considered previously, the low-Doppler spectral component associated with ground clutter will bias mean velocity estimates away from the thunderstorm outflow velocity. To eliminate this bias, clutter filtering -- either in the time- or frequency-domains -- is required prior to forming the velocity estimate. The short coherent processing intervals (CPI) of an airport surveillance radar, however, severely limit the capability to achieve a narrow low-Doppler stop-band that will not effect weather sensing capability.

One approach to the problem would be to construct a bank of bandpass filters using all the pulses in the 8- or 10-pulse CPI as in the ASR-9 target channel; the weather radial velocity would then be estimated by determining the filter with the largest output. In those filters significantly removed from zero Doppler, ground clutter could readily be attenuated by 40 dB or more. The drawbacks to this approach are: (a) the filter passbands would be broad (approximately 8 ms^{-1}) resulting in poor velocity resolution for weather signals and a broad region around zero Doppler where weather echoes would not be detected; and (b) it might be difficult to identify that filter with peak response owing to the random nature of the weather signal. Anderson (17) considers the application of this approach to wind shear detection with an ASR.

Slower scanning meteorological Doppler radars frequently apply a time-domain digital filter to each CPI, followed by pulse-pair velocity estimation. This technique does not carry over in a straightforward manner to an airport surveillance radar because the filter impulse response length must be almost as long as the available CPI to achieve a useful transfer function. As a result, insufficient filtered data are available for velocity estimation. Anderson (17) describes a modification to this approach where the filter would operate across two or three adjacent CPIs, thereby providing sufficient time samples for clutter filtering and velocity estimation. His simulations indicate that reliable weather radial velocity estimates can be obtained when the signal to clutter ratio is approximately -40 dB or greater.

An alternative approach to clutter filtering and weather velocity estimation with an airport surveillance radar would involve full spectral estimation, probably using parametric or "high resolution" techniques. The use of such estimators is attractive, given the small number of data samples available for resolving the weather and ground clutter spectral components. Computational requirements of these algorithms are high, however, and an additional computation of mean weather radial velocity (for example, a power weighted average over the spectral interval outside the ground clutter region) would be required.

Clearly any method of clutter filtering will involve a tradeoff between achieved clutter suppression and the width of the low-Doppler "blind" interval where weather echoes will be subject to significant attenuation. To illustrate reasonable requirements on subclutter visibility at the Memphis and Denver airport sites, Tables IV-1 through IV-4 give the percent of radar resolution cells where echoes from a 20 dBZ microburst would exceed the interference background by at least 5 dB, assuming that ground clutter attenuation of 0, 10, 20, 30 or 40 dB is achievable. The 5 dB signal-to-interference ratio represents a minimum value for reliable weather velocity estimation with a pulse-pair estimator. The percentages are calculated within 2 km range intervals out to 10 km, and then in 10 km intervals to 30 km. The upper figure is for the high receiving beam and the lower figure is for the low beam.

Table IV-1: Percent Resolution Cells with Signal/(Clutter+Noise) > 5 dB

Memphis International Airport
Outflow Reflectivity = 20 dBz
Outflow Depth = 300 m

Range (km)	Clutter Attenuation (dB)					Resampling Requirement
	0	10	20	30	40	
0-2	1 / 0	12 / 1	40 / 12	72 / 37	83 / 65	7
2-4	8 / 1	34 / 8	67 / 26	94 / 51	99 / 86	21
4-6	14 / 9	44 / 28	68 / 46	90 / 68	98 / 93	36
6-8	3 / 10	40 / 33	69 / 57	86 / 77	96 / 94	50
8-10	0 / 9	8 / 34	27 / 55	42 / 73	50 / 91	64
10-20	0 / 18	0 / 49	0 / 69	0 / 84	0 / 95	*
20-30	0 / 11	0 / 42	0 / 59	0 / 67	0 / 70	*

Table IV-2: Percent Resolution Cells with Signal/(Clutter+Noise) > 5 dB

Memphis International Airport
Outflow Reflectivity = 20 dBz
Outflow Depth = 1000 m

Range (km)	Clutter Attenuation (dB)					Resampling Requirement
	0	10	20	30	40	
0-2	2 / 0	13 / 1	41 / 12	73 / 37	83 / 65	7
2-4	17 / 2	45 / 10	79 / 27	98 / 53	100 / 88	21
4-6	41 / 14	65 / 32	88 / 50	98 / 73	100 / 96	36
6-8	52 / 19	77 / 44	90 / 66	98 / 83	100 / 99	50
8-10	50 / 23	74 / 47	88 / 65	97 / 82	100 / 99	64
10-20	59 / 46	81 / 67	92 / 82	98 / 93	100 / 100	*
20-30	46 / 73	60 / 91	65 / 98	67 / 99	67 / 100	*

*   Average area of radar resolution cells is greater than Cartesian cell.

Table IV-3: Percent Resolution Cells with Signal/(Clutter+Noise) > 5 dB

Denver Stapleton Airport
Outflow Reflectivity = 20 dBz
Outflow Depth = 300 m

Range (km)	Clutter Attenuation (dB)					Resampling Requirement
	0	10	20	30	40	
0-2	6 **	30 **	50 **	74 **	87 **	7
2-4	20 / 12	53 / 33	78 / 61	93 / 82	98 / 95	21
4-6	54 / 39	82 / 69	94 / 89	98 / 96	100 / 99	36
6-8	57 / 50	83 / 77	94 / 91	98 / 97	100 / 100	50
8-10	30 / 62	44 / 84	52 / 94	54 / 98	56 / 99	64
10-20	0 / 38	0 / 69	0 / 83	0 / 89	0 / 94	*
20-30	0 / 17	0 / 42	0 / 55	0 / 63	0 / 67	*

Table IV-4: Percent Resolution Cells with Signal/(Clutter+Noise) > 5 dB

Denver Stapleton Airport
Outflow Reflectivity = 20 dBz
Outflow Depth = 1000 m

Range (km)	Clutter Attenuation (dB)					Resampling Requirement
	0	10	20	30	40	
0-2	6 **	31 **	50 **	75 **	88 **	7
2-4	32 / 13	63 / 36	84 / 63	94 / 83	99 / 95	21
4-6	79 / 46	93 / 75	98 / 91	99 / 97	100 / 100	36
6-8	88 / 62	96 / 84	99 / 94	100 / 99	100 / 100	50
8-10	92 / 76	96 / 91	99 / 96	100 / 99	100 / 100	64
10-20	82 / 66	92 / 82	95 / 88	98 / 93	99 / 99	*
20-30	58 / 69	63 / 82	65 / 90	66 / 96	67 / 99	*

*   Average area of radar resolution cells is greater than Cartesian cell.

**   Low beam clutter data not available inside 2 km.

For the two sites, Tables IV-1 and IV-3 assume beamfilling losses appropriate to a thunderstorm outflow that is 300 m in depth, whereas IV-2 and IV-4 assume an outflow depth of 1000 m. While receiver noise was included in calculating the interference term, we did not include a contribution from precipitation echoes above the outflow layer.

At Memphis, clutter attenuation of 20-40 dB would be necessary in the critical region within 10 km of the airport if more than half of the resolution cells are to contain usable low-beam weather data. For corresponding fractional visibility, the high beam signal would require 10-20 dB less attenuation at ranges less than 8 km; beyond 9 km however, beamfilling loss for the 300 m deep outflow considered in Table IV-1 reduces high-beam echo power to the point that system noise would prevent detection. A corresponding reduction in low beam signal power occurs at 27 km range, producing the smaller fractional visibility values in the 20-30 km range interval.

At short range, attenuation requirements for a deeper 1000 m outflow at Memphis (Table IV-3) are similar to the above. However, high beam data would now be usable to at least 20 km with 20-30 dB clutter attenuation, owing to much reduced beamfilling loss.

Near-in ground clutter at Denver was less intense than at Memphis. Within 10 km of the radar, the percent of unobscured resolution cells is therefore higher than at Memphis, given the same assumed ground clutter attenuation. For low-beam detection of a 20 dBZ outflow in half of the resolution cells inside 10 km, 10 - 20 dB ground clutter attenuation would suffice even if the outflow is shallow (Table IV-3). As will be shown subsequently, however, the intense ground clutter to the west of the radar at ranges greater than 15 km would result in large areas of obscuration unless 30-40 dB attenuation were achieved.

To aid in interpretation of the tables, the last column shows the percentage of usable resolution cells required for resampling the radar data to a lower resolution (at short range) Cartesian grid. Because the "targets" of interest here are extensive relative to a single range-azimuth cell, detection of thunderstorm outflows need occur only in a relatively small fraction of available resolution cells. This approach requires implementation of a ground-clutter "map" to identify those resolution cells that should be used for weather processing. We choose 200 m x 200 m as the maximum Cartesian bin size that would permit reliable identification of a 1-2 km radius microburst. For this bin size, the last column in the tables shows the percentages of unobscured resolution cells required for an average of one usable range/azimuth gate per Cartesian cell. Comparison with the table suggests, for example that this use of "interclutter" visibility might permit as little as 20 dB clutter suppression to be employed for low-beam data inside 10 km at Memphis. As illustrated subsequently, however, the non-uniform azimuthal distribution of the ground clutter will require that average fractional visibility be significantly higher than the values given if clutter obscuration is to be eliminated.

The above calculations are repeated in Tables IV-5 through IV-8 using the same assumptions except that outflow reflectivity is taken to be 45 dBZ. In this case, fractional visibility significantly exceeds the average requirement for Cartesian resampling in both receiving beams, even without clutter filtering.

Table IV-5: Percent Resolution Cells with Signal/(Clutter+Noise) > 5 dB

Memphis International Airport
Outflow Reflectivity = 45 dBz
Outflow Depth = 300 m

Range (km)	Clutter Attenuation (dB)					Resampling Requirement
	0	10	20	30	40	
0-2	55 / 18	80 / 50	99 / 92	100 / 100	100 / 100	7
2-4	83 / 37	98 / 68	100 / 99	100 / 100	100 / 100	21
4-6	82 / 57	96 / 82	99 / 100	100 / 100	100 / 100	36
6-8	84 / 68	95 / 86	99 / 99	100 / 100	100 / 100	50
8-10	78 / 65	92 / 82	98 / 99	100 / 100	100 / 100	64
10-20	85 / 79	95 / 91	99 / 99	100 / 100	100 / 100	*
20-30	98 / 96	99 / 99	100 / 100	100 / 100	100 / 100	*

Table IV-6: Percent Resolution Cells with Signal/(Clutter+Noise) > 5 dB

Memphis International Airport
Outflow Reflectivity = 45 dBz
Outflow Depth = 1000 m

Range (km)	Clutter Attenuation (dB)					Resampling Requirement
	0	10	20	30	40	
0-2	56 / 18	80 / 51	99 / 92	100 / 100	100 / 100	7
2-4	92 / 39	99 / 71	100 / 99	100 / 100	100 / 100	21
4-6	95 / 62	99 / 87	100 / 100	100 / 100	100 / 100	36
6-8	95 / 75	99 / 92	100 / 100	100 / 100	100 / 100	50
8-10	94 / 74	99 / 92	100 / 100	100 / 100	100 / 100	64
10-20	96 / 88	99 / 98	100 / 100	100 / 100	100 / 100	*
20-30	99 / 99	100 / 100	100 / 100	100 / 100	100 / 100	*

*   Average area of radar resolution cells is greater than Cartesian cell.

Table IV-7: Percent Resolution Cells with Signal/(Clutter+Noise) > 5 dB						
Denver Stapleton Airport *Outflow Reflectivity = 45 dBz* *Outflow Depth = 300 m*						
Range (km)	Clutter Attenuation (dB)					Resampling Requirement
	0	10	20	30	40	
0-2	59 **	82 **	97 **	100 **	100 **	7
2-4	87 73	96 90	99 99	100 100	100 100	21
4-6	97 93	99 98	100 100	100 100	100 100	36
6-8	98 95	99 99	100 100	100 100	100 100	50
8-10	97 96	99 99	100 100	100 100	100 100	64
10-20	93 87	96 92	99 98	100 100	100 100	*
20-30	94 88	97 94	99 98	100 100	100 100	*

Table IV-8: Percent Resolution Cells with Signal/(Clutter+Noise) > 5 dB						
Denver Stapleton Airport *Outflow Reflectivity = 45 dBz* *Outflow Depth = 1000 m*						
Range (km)	Clutter Attenuation (dB)					Resampling Requirement
	0	10	20	30	40	
0-2	60 **	82 **	97 **	100 **	100 **	7
2-4	91 74	97 90	100 99	100 100	100 100	21
4-6	99 95	100 99	100 100	100 100	100 100	36
6-8	99 97	100 99	100 100	100 100	100 100	50
8-10	99 98	100 100	100 100	100 100	100 100	64
10-20	97 91	99 97	100 100	100 100	100 100	*
20-30	98 94	99 98	100 100	100 100	100 100	*

*   Average area of radar resolution cells is greater than Cartesian cell.

**   Low beam clutter data not available inside 2 km.

Finally, in figure IV-7 we plot the spatial distribution of the low- beam signal-to-interference ratio for the two sites assuming: (a) outflow reflectivity of 20 dBZ and beamfilling loss corresponding to a 300 m outflow depth; (b) clutter attenuation of 20, 30 or 40 dB; and (c) selection of that range-azimuth cell in each 200 m x 200 m Cartesian bin with the smallest ground clutter residue for weather parameter estimation. Grey areas in the PPI displays correspond to regions where the signal-to-interference ratio is between 0 and 5 dB; black designates areas where the ratio is below 0 dB or else clutter data is missing. (Compare with figure IV-1 to determine regions of missing data). The color rings are the effect of azimuth- independent beamfilling loss.

The intense ground clutter north of the radar at Memphis was quite homogeneous spatially; thus, the fractional visibility requirement in this area is much higher than the azimuthally averaged requirement for resampling listed in the Tables. As a result, clutter attenuation about 20 dB greater than suggested by Table IV-1, or 40 dB, is required for a signal-to-interference ratio large enough for weather velocity estimation in this area. Similarly at the Denver site, clutter attenuation of 40 dB is required if large areas of low-beam obscuration to the west and northwest of the radar are to be avoided. For both sites, beamfilling loss becomes the dominant factor limiting detection of a shallow 20 dBZ outflow beyond 25 km.

Clutter filtering must be set up to handle the worst-case thunderstorm outflow assumptions (i.e. low reflectivity and shallow depth). Thus the above arguments indicate that at the sites considered 40 dB of ground clutter attenuation, in combination with the use of interclutter visibility techniques, would be required for velocity estimation with both beams of an airport surveillance radar. As suggested by figures IV-1 and IV-7, this requirement for filter attenuation could be considerably relaxed over much of the area considered if the clutter filters were chosen on a range-azimuth dependent basis. Additionally, if received power in a resolution cell was significantly above the ground clutter residue stored in a clear day "map", it would be appropriate to select a wider-passband or all-pass filter for weather parameter estimation in that cell. These techniques, which are used in the ASR-9 six-level weather reflectivity processor, would minimize impact of the clutter filters on weather velocity estimation while maintaining clutter residues below the required level.

SIGNAL/INTERFERENCE (dB)

77540-33

ATTENUATION 20 dB

65
60
55
50
45
40
35
30
25
20
15
10
5
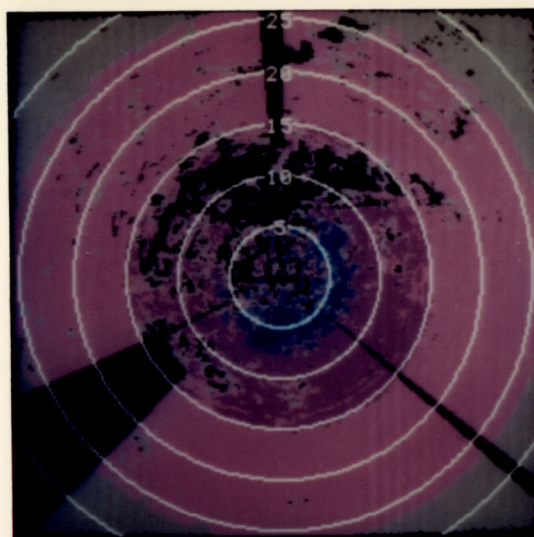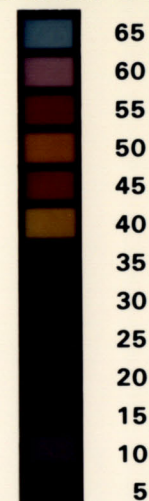
30 dB
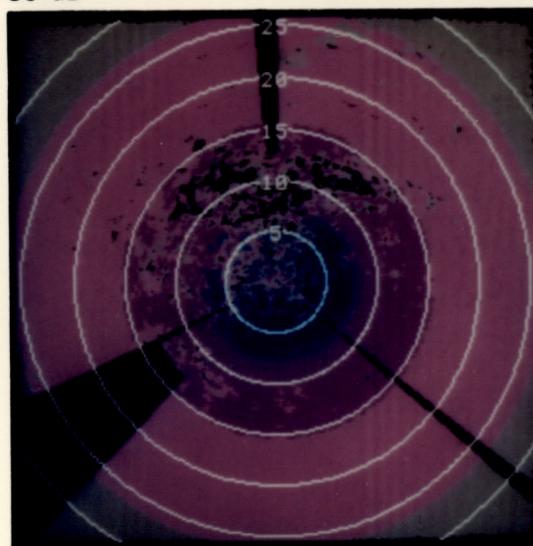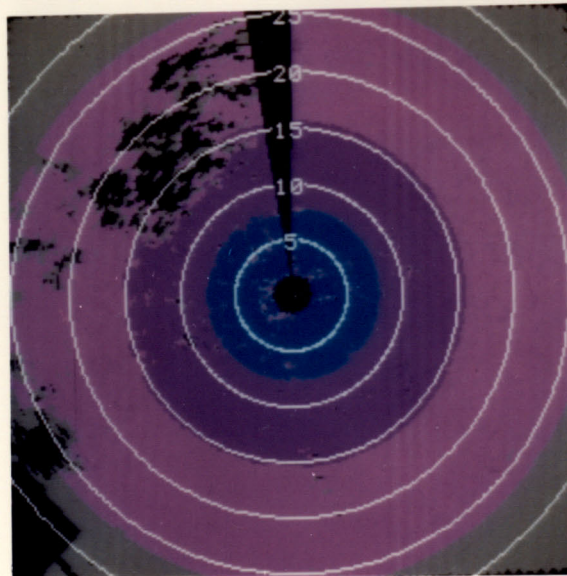
40 dB
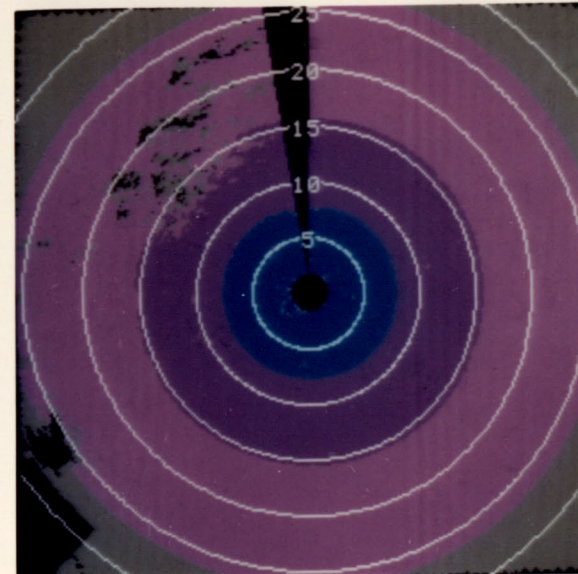
MICROBURST REFLECTIVITY= 20 dBz
MICROBURST DEPTH = 300 M

Figure IV-7a. PPI display of the signal-to-(ground clutter+noise) ratio (dB) for the low beam of the ASR-8 at Memphis. Microburst reflectivity is taken as 20 dBZ and assumed outflow depth is 300 m. Clutter attenuation of 20,30 or 40 dB is assumed, followed by resampling to a 200 x 200 m Cartesian grid as described in the text.

Figure IV-7b. PPI display of the signal-to-(ground clutter+noise) ratio for the low beam of the ASR-8 at Denver. The assumptions are as in Figure IV-7a.

V. SUMMARY AND PLANNED FUTURE WORK

A. Summary

We have examined the capability for thunderstorm outflow velocity measurements with airport surveillance radars through consideration of the ratio of outflow signal power to interference from receiver noise, ground clutter and precipitation above the low-altitude wind shear layer. We indicated that the sensitivity of an ASR is sufficient to detect even low reflectivity (20 dBZ) wind shear events subject to important caveats. For shallow outflows (depth less than about 500 m) beamfilling loss will severely degrade high beam sensitivity, even at ranges less than 10 km. This loss of outflow signal power is compounded by an increase in the interference background caused by precipitation echoes above the outflow layer. These problems were shown to be less severe if data from the low receiving beam could be used at ranges where an ASR would conventionally employ the high beam.

The desirability of using low-beam data in the critical region near an airport lead to examination of ground clutter measured with operational ASR-8's at Memphis, TN and Denver, CO. We found that use of interclutter visibility techniques would permit low-beam detection of shallow, weakly reflecting thunderstorm outflows if attenuation of 40 dB could be achieved through clutter "filtering". For the sites treated here, this requirement could be significantly relaxed over much of the radars' coverage areas through appropriate processor design. We did not consider in detail the signal processing problem of achieving the required clutter suppression with the short coherent processing intervals of the ASR-9. An interim evaluation of this problem is given by Anderson (17).

In many cases, microburst reflectivity will be sufficiently high that receiver noise and ground clutter are of secondary importance with respect to an ASR's detection capability. In these cases, the echo spectrum component associated with precipitation above the outflow layer may be the primary factor limiting the range to which the wind-shear event could be detected and the accuracy of radial velocity shear estimates. We indicated that, even using the low receiving beam, a maximum detection range of about 20 km would be expected for microbursts if the reflectivity of overhanging precipitation is roughly equal to reflectivity in the outflow layer. For very shallow outflows (500 m or less), this range could be as small as 5-10 km. One of the microburst case studies presented illustrated the difficulty of detecting a shallow outflow, even at short range.

We evaluated the extent to which a processor architecture that combined signals from the high and low receiving beams could produce more accurate low-altitude velocity estimates. In simulations with simple outflow models, coherent combination of time-series signals from the two beams to synthesize a more favorable elevation beam pattern resulted in a 30% increase in the maximum detection range for "outflows" less than 1000 m in depth. An alternate approach that includes cancellation of the overhanging echo spectrum component using an "orthogonal" signal channel might provide a more significant improvement in the ability to measure radial velocity in shallow outflows. Simulations indicated, however, that improvement in the accuracy of radial velocity estimates using a simple implementation of this technique was limited by the use of static combining weights and by statistical fluctuations of the weather signal.

B. Conclusions

Overall, our analysis indicates that an airport surveillance radar could serve as a useful sensor for measurement of low altitude wind shear in the critical region within 10 km of an airport. This

presumes that the required clutter filtering and velocity estimation can be performed using the short coherent processing interval of the fast-scanning radar. Detection of thunderstorm outflows and accurate estimation of radial velocity shear at ranges greater than 10 km will depend on the depth of the outflow and the distribution of cloud reflectivity in the vertical. Clearly the detection probability for an ASR will be significantly lower than for an appropriately sited pencil-beam Doppler weather radar such as TDWR. As indicated in the introduction, an appropriate role for airport surveillance radars is as adjunct wind-shear sensors, providing for example an alternate aspect angle to near- or on-airport outflows. The operational use of wind-shear data from ASRs sited at airports that do not have a TDWR must be based on a reliable estimate of detection and false-alarm probabilities for the site under consideration.

C. Near Term Plans for Further Analysis

Additional analysis of pencil beam weather radar data will provide more extensive statistics on the vertical structure of microbursts and gust fronts. Data from the FLOWS/MIST experiment in Huntsville, AL and from the JAWS project near Denver are being used to characterize the outflow reflectivity distribution in "wet" and "dry" microburst environments and the impact of overhanging precipitation. RHI scans of microbursts within 10-20 km range provide the necessary resolution in altitude.

Volume scans with sector tilts at contiguous elevation-angles, or RHI scans at adjacent azimuth angles will be used to simulate ASR processing over an entire wind-shear event, as opposed to the selected azimuthal "cuts" considered in this report. When dual- or multiple-Doppler coverage is available, three-component wind vector analysis would allow the data field to be translated to arbitrary ranges and aspect angles with respect to an "ASR". Our intention is to generate a number of microburst and gust front cases for use in developing and evaluating signal-processing and wind-shear detection algorithms.

Future simulations will include the effect of ground clutter and the necessary Doppler filtering. I and Q data from the ASR-8's at Memphis and Denver will be used to provide clutter signals with realistic amplitudes and temporal statistics. Our first-cut scheme for clutter filtering/velocity estimation will involve:

(a)   interpolation of the block-staggered PRF signal samples (weather plus clutter) to a uniform sampling interval. This would result in usable coherent processing intervals two to three times longer than the eight or ten available from the ASR-9, provided that the weather echoes are not aliased;

(b)   clutter filtering with a weighted Chebyshev high-pass filter designed for the interpolated sampling frequency;

(c)   pulse-pair velocity estimation using the low receiving beam or dual-beam techniques as described in this report.

This scheme is analogous to one of those described by Anderson (17) except that it effectively applies a shift-variant filter to the original block-staggered data.

Owing to the fast scanning ASR antenna and corresponding short CPI, clutter filtering based on linear processing techniques will necessarily produce a wide low-Doppler interval where weather echoes will undergo significant attenuation. The resulting bias in velocity estimates could be significant for LAWS detection when, for example, one component of a microburst outflow has a low absolute radial velocity owing to overall storm translation. Techniques based on high-

resolution spectral estimation will be evaluated to determine whether the necessary clutter attenuation can be achieved while maintaining sensitivity to low radial velocity weather echoes.

As indicated in this report, the ground clutter distribution at Memphis was considerably more severe in relation to aircraft takeoff and departure paths than at Denver. It would be desirable to obtain ASR clutter data from additional major air terminals to obtain more extensive statistics on clutter reduction requirements.

FAA usage of Doppler weather radar data requires computer recognition of low-level wind shear to alert controllers to the hazard. The algorithms under development for TDWR (1,2,3) can serve as a starting point for a corresponding capability for airport surveillance radars. However, substantial modifications will be required for the ASR owing to the lack of vertically resolved data, the generally less reliable outflow velocity estimates and the loss of weather data caused by clutter filtering. In addition, the on-airport siting of ASRs means that operationally important microbursts may sometimes occur over the radar, thereby involving diametric radials. Existing algorithms utilizing radial velocity shear as a detection parameter will require modification for this case.

To provide real storm data for assessing LAWS detection with an airport surveillance radar, Lincoln Laboratory has deployed a modified ASR-8 in Huntsville, AL. A colocated pencil-beam Doppler weather radar serves as "truth" for these measurements. The transmitter control of the ASR-8 has been modified to provide the block-staggered PRF waveform that will be used by the ASR-9. I and Q samples from both receiving beams are recorded synchronously on high-density digital tape for off-line analysis.

These data will allow for confirmation of results from simulation and analysis and will facilitate identification of hardware issues. While the number of microbursts or gust fronts occurring at close range to the radar will be limited, we expect that sufficient cases will be observed during operations in 1987 to provide at least a preliminary demonstration of the capabilities and limitations of ASRs for low-altitude wind shear detection. We anticipate that the combination of results from this testbed radar and analysis as described above using the more extensive data available from meteorological field programs will provide the necessary basis for determining the operational role of airport surveillance radars as LAWS sensors.

REFERENCES:

1. H. Uyeda and D.S. Zrnic, *Automatic Detection of Gust Fronts,* Final Report DOT-FAA-PM-85-11, April 1985.

2. M.W. Merritt, Microburst Detection Algorithm, *NEXRAD/JSPO* 1986.

3. S. Campbell, Microburst Recognition: An Expert System Approach, *Preprints, 23rd Radar Meteor. Conf.,* Snowmass, Co., American Meteor. Soc., Boston, Ma., 1986.

4. T.T. Fujita, *The Downburst,* SMRP Research Paper **210,** University of Chicago, 1985.

5. T.T. Fujita, *DFW Microburst on August 2,1985,* SMRP Research Paper **217,** University of Chicago, 1986.

6. T.T. Fujita, *Microburst Wind Shear at New Orleans International Airport, Kenner, Louisiana on July 9,1982,* SMRP Research Paper **199,** University of Chicago, 1983.

7. R.C. Goff, Observation of Thunderstorm Induced Low Level Wind Variations, *Preprints, Amer. Inst. of Aeronautics and Astronautics, 9th Fluid and Plasma Dynamics Conf.,* San Diego, CA (AIAA Paper No. 76-388), 1976.

8. L. Stevenson, *The Stapleton Microburst Advisory Service Experiment: An Operational Viewpoint,* Final Report DOT-TSC-FAA-85-8, September 1985.

9. J.E. Evans and D.H. Turnbull, The FAA/MIT Lincoln Laboratory Doppler Weather Radar Program, *Preprints: Second International Conference on the Aviation Weather System ,* Montreal, P.Q., Canada, American Meteor. Soc., Boston, Ma., 1985

10. J.W. Wilson, R.D. Roberts, C. Kessinger and J. McCarthy, Microburst Wind Structure and Evaluation of Doppler Radar for Airport Wind Shear Detection *J. Climate Appl. Meteor.* **23,** pp. 989-915, 1984.

11. M.W. Wolfson, J.T. DiStefano and B.E. Forman *The FLOWS Automatic Weather Station Network in Operation,* Project Report ATC 134, Lincoln Laboratory, MIT, FAA-PM-85-27, 1987.

12. R.E. Rinehart and M.A. Isaminger, Radar Characteristics of Microbursts in the Mid South, *Preprints, 23rd Radar Meteor. Conf.,* Snowmass, Co., American Meteor. Soc., Boston, Ma., 1986.

13. D.L. Klingle, *A Gust Front Case Studies Handbook,* Project Report ATC-129, Lincoln Laboratory, MIT, FAA-PM-84-15, 1985.

14. R.J. Doviak and D.S. Zrnic, *Doppler Radar and Weather Observations,* (Academic Press, 1984), 458 pp.

15. D. Sirmans and B. Bumgarner, Numerical Comparison of Five Mean Frequency Estimators , *J. Appl. Meteor.* **14** , pp. 991-1003,1975.

16. C.F. Winter, Vertical Plane Pattern Calculations for Shaped Beam Reflectors with Multiple Feeds, *IEEE Trans. Antennas Propagat.* **AP-22,** pp. 495-497, 1974.

17. J.R. Anderson, The Measurement of Doppler Wind Fields with Fast Scanning Radars, submitted to *J. Atmos. Oceanic Technology ,* 1986.

APPENDIX A: CALCULATION OF THE MINIMUM DETECTABLE WEATHER REFLECTIVITY FACTOR

The sensitivity of the ASR-9 receiver is specified as -108 dBm. This figure presumably includes receiver losses, thermal noise, processing gains for bandlimited signals against noise and thresholding requirements for detection. For comparison, thermal noise at $293^{\circ}K$ is -110 dBm for the ASR-9 receiver. We use the more conservative figure since it more accurately reflects the limit for confident detection of a weather echo.

The equation for received power from precipitation (for example, equation 4.30 in Doviak and Zrnic (14)) is then inverted to calculate the minimum detectable reflectivity factor:

$$Z_{\min}(mm^6/m^3) = 2.50 \; x \; 10^{19} \; \frac{\lambda^2 R^2 P_N}{P_T \, G^2 l^2 l_R \, l_{STC} \, \tau \theta \phi |K_W|^2} \tag{A.1}$$

$$= 1.92 \; x \; 10^{-3} \; \frac{R^2}{l_{STC}}$$

If the STC attenuation is constant, this limit increases with range from the radar as R^2. The parameters in equation (A.1) are given below.

λ	wavelength (cm)	11
R	range (km)	
P_N	minimum detectable receiver power (mW)	$10^{(-108/10)}$
P_T	transmitted power (W)	$1.12 \; x. \; 10^6$
G	antenna gain	$10^{(34/10)}$
l	loss due to atmospheric attenuation	1.0
l_R	loss due to finite receiver bandwidth	$10^{(-2.3/10)}$
l_{STC}	attenuation from STC function	
τ	radar pulse duration (μs)	1.03
θ	elevation beamwidth (deg)	4.8
ϕ	azimuthal beamwidth (deg)	1.4
$|K_W|$	magnitude of index of refraction for water	0.93

APPENDIX B: CALCULATION OF WEIGHTING COEFFICIENTS FOR COMBINATION OF HIGH AND LOW BEAM SIGNALS

1. Combination of I and Q time-series signals

We seek first a range-dependent complex weight:

$$\eta(R) = \alpha(R) + i\beta(R) \tag{B.1}$$

such that the ratio of signal power from a low altitude outflow layer to interference from echoes above the outflow layer:

$$\frac{P(S)}{P(C)} = \frac{\int_0^{\theta_0} Z(\theta) || V_1(\theta)\{V_1(\theta)+\eta V_2(\theta)\} ||^2 d\theta}{\int_{\theta_0}^{\frac{\pi}{2}} Z(\theta) || V_1(\theta)\{V_1(\theta)+\eta V_2(\theta)\} ||^2 d\theta} \tag{B.2}$$

is an extremum. The variables in (B.2) were defined in the discussion of equation (5) in the text. The elevation-angle dependent phase difference between the high- and low-beam voltage antenna patterns is incorporated into the high-beam pattern:

$$V_2(\theta) = \delta(\theta) + i\kappa(\theta) \tag{B.3}$$

so that $V_1(\theta)$ is taken as real.

We shall employ the following definitions in deriving the extrema of equation (B.2):

$$
\begin{aligned}
A_1 &= \int_0^{\theta_0} Z(\theta) V_1^2(\theta) d\theta \\
B_1 &= \int_0^{\theta_0} Z(\theta) \delta^2(\theta) d\theta \\
C_1 &= \int_0^{\theta_0} Z(\theta) \kappa^2(\theta) d\theta \\
D_1 &= \int_0^{\theta_0} Z(\theta) V_1(\theta) \delta(\theta) d\theta \\
E_1 &= \int_0^{\theta_0} Z(\theta) V_1(\theta) \kappa(\theta) d\theta \\
A_2 &= \int_{\theta_0}^{\frac{\pi}{2}} Z(\theta) V_1^2(\theta) d\theta \\
B_2 &= \int_{\theta_0}^{\frac{\pi}{2}} Z(\theta) \delta^2(\theta) d\theta \\
C_2 &= \int_{\theta_0}^{\frac{\pi}{2}} Z(\theta) \kappa^2(\theta) d\theta \\
D_2 &= \int_{\theta_0}^{\frac{\pi}{2}} Z(\theta) V_1(\theta) \delta(\theta) d\theta \\
E_2 &= \int_{\theta_0}^{\frac{\pi}{2}} Z(\theta) V_1(\theta) \kappa(\theta) d\theta \\
a_0 &= A_2 D_1 - A_1 D_2 \\
a_1 &= A_2(B_1 + C_1) - A_1(B_2 + C_2)
\end{aligned}
\tag{B.4}
$$

$$a_2 = D_2E_1 - D_1E_2$$

$$a_3 = D_2(B_1+C_1) - D_1(B_2+C_2)$$

$$a_4 = E_1(B_2+C_2) + E_2(B_1+C_1)$$

$$b_0 = A_1E_2 - A_2E_1$$

These quantities are entirely defined by the voltage antenna patterns, an assumed upper boundary for the outflow layer and an assumed profile of precipitation reflectivity.

Differentiating equation (B.2) with respect to α and β and setting the result equal to zero gives a pair of simultaneous equations:

$$f_2(\alpha,\beta)g_1(\alpha) - f_1(\alpha,\beta)g_2(\alpha) = 0 \tag{B.5}$$

$$f_2(\alpha,\beta)h_1(\alpha) - f_1(\alpha,\beta)h_2(\alpha) = 0$$

where

$$f_1(\alpha,\beta) = A_1 + 2\alpha D_1 - 2\beta E_1 + (\alpha^2 + \beta^2)(B_1 + C_1)$$

$$f_2(\alpha,\beta) = A_2 + 2\alpha D_2 - 2\beta E_2 + (\alpha^2 + \beta^2)(B_2 + C_2)$$

$$g_1(\alpha) = 2D_1 + 2\alpha(B_1 + C_1) \tag{B.6}$$

$$g_2(\alpha) = 2D_2 + 2\alpha(B_2 + C_2)$$

$$h_1(\beta) = -2E_1 + 2\beta(B_1 + C_1)$$

$$h_2(\beta) = -2E_2 + 2\beta(B_2 + C_2)$$

It follows that:

$$\frac{g_1(\alpha)}{g_2(\alpha)} = \frac{h_1(\beta)}{h_2(\beta)} \tag{B.7}$$

This can be expanded to yield a linear relation between the real and imaginary parts of the weighting coefficient:

$$a_4\alpha - a_3\beta + a_2 = 0 \tag{B.8}$$

Substituting this relation back into equation (B.5) and expanding terms yields a quadratic equation for the real part of the weighting coefficient:

$$\left\{2(a_3^2 + a_4^2)\frac{a_4}{a_3}\right\}\alpha^2 +$$

$$\left\{2a_1a_4 - 2a_2a_3 + \frac{2a_2a_4^2}{a_2} + 2(a_3^2 + a_4^2)\frac{a_2}{a_3}\right\}\alpha + \tag{B.9}$$

$$\left\{a_0a_4 + b_0a_3 + 2a_2^2\frac{a_4}{a_3} + a_1a_2\right\} = 0$$

The roots of equation (B.9), in combination with (B.8) define the desired complex weights.

2. Combination of autocorrelation lag estimates

We consider next the combination of autocorrelation lag estimates from two receiving channels (i.e. the maximum and minimum signal to interference channels considered above). We denote the complex time-samples for channel j by $x_{i,j}$ which can be resolved into a component due to scattering from the thunderstorm outflow layer, $s_{i,j}$, and from precipitation above the outflow, $c_{i,j}$:

$$x_{i,j} = s_{i,j} + c_{i,j} \qquad j = 1,2 \tag{B.10}$$

The autocorrelation functions at a one sample delay are then:

$$R_{xx}(\tau_s,j) = < x_{i+1,j} x^*_{i,j} > \tag{B.11}$$
$$= < s_{i+1,j} s^*_{i,j} > + < c_{i+1,j} c^*_{i,j} >$$

where cross-terms vanish owing to the expectation operation. The desired information on outflow radial velocity is contained in the phase of the first terms on the right. As a simplifying assumption, we take the weather echo spectrum to be constant in altitude within the two layers considered. Then the different elevation angle weightings for the two receiving channels do not affect the phase of the signal and "clutter" components of the autocorrelation function. This allows for cancellation of the clutter components in (B.11) through linear combination of the auto-correlation samples from the two receiving channels:

$$R_{xx}(\tau_s,1) + \gamma R_{xx}(\tau_s,2) = < s_{i+1,1} s^*_{i,1} > + \gamma < s_{i+1,2} s^*_{i,2} > \tag{B.12}$$

The combining weight:

$$\gamma = - \frac{< c_{i+1,1} c^*_{i,1} >}{< c_{i+1,2} c^*_{i,2} >} \tag{B.13}$$

is a real number by virtue of the above assumption on weather variation with height.

If we further assume that the elevation angle resolved weather echo spectra are Gaussian in shape, then the precipitation clutter component of the autocorrelation function at one sample delay is related to the total power of this spectral component by:

$$R_{cc}(\tau_s,j) = < c_{i+1,j} c^*_{i,j} > \tag{B.14}$$
$$= R_{cc}(0,j) e^{-2\pi^2 \sigma_f^2 \tau_s^2} e^{i 2\pi f_c \tau_s}$$

This allows the combining weight to be written as:

$$\gamma = - \frac{R_{cc}(0,1)}{R_{cc}(0,2)} \tag{B.15}$$

$$= \frac{-\int_{\theta_0}^{\frac{\pi}{2}} Z(\theta) || V_1(\theta)\{ V_1(\theta) + \eta_1 V_2(\theta)\} ||^2 d\theta}{\int_{\theta_0}^{\frac{\pi}{2}} Z(\theta) || V_1(\theta)\{ V_1(\theta) + \eta_2 V_2(\theta)\} ||^2 d\theta}$$

where η_1 and η_2 are the coherent combining weights associated with the maximum and minimum signal-to-precipitation interference channels respectively. The combining weight γ for the auto-correlation functions can again be computed from knowledge of the antenna elevation patterns and an assumed model for reflectivity versus altitude.

3. Illustration of error sources for dual-channel velocity estimates

As indicated in section III, errors in estimating outflow radial velocity with the dual-channel method illustrated in figure III-10(b) result from:

(a)   discrepancies between actual outflow structure and the model used in evaluating (B.15);

(b)   statistical error in estimation of the autocorrelation functions (B.11) which results in imperfect "clutter" cancellation even when the assumed outflow model is appropriate.

Figure B-1 illustrates the error introduced by an inexact model for thunderstorm outflow structure. As in the text, combining weights were computed assuming an outflow depth of 500 m and uniform reflectivity from the surface to 5000 m. Assuming that the autocorrelation function can be exactly determined, the figures plot estimated velocity versus range when:

(a)   actual outflow heights are 300 m, 500 m, 1000 m and 3000 m;

(b)   reflectivity is constant from the surface to 10,000 m;

(c)   outflow radial velocity is -15 ms^{-1} and overhanging precipitation radial velocity is 5 ms^{-1}.

The figure is directly comparable with figure III-15 in the text.

It is seen that the magnitude of the error introduced is small when the actual outflow depth is equal to or greater than the assumed depth, 500 m. For a shallower 300 m depth outflow, the inappropriate choice for the weighting coefficient results in significant bias in the velocity estimates beyond about 5 km.

Figure B-2 simulates an autocorrelation lag "estimate error" for each channel. The calculations are as in the preceding figure except that an "error vector" has been added to each autocorrelation function. The magnitude of this error is uniformly distributed from 0 to the true magnitude of the autocorrelation function; the phase is taken as uniformly distributed between 0 and 2π.

The mean of the resulting velocity estimates may differ significantly from the values in figure B-1 when the weighted magnitude of the autocorrelation function in the second receiving channel is comparable to that in the first channel. In this circumstance, the contribution from the "error" components may substantially alter the phase of the vector formed by combining the two functions. The resulting velocity estimates will be subject to large errors and may be distributed over a significant portion of the Nyquist interval. The effect is to bias the mean of the velocity estimates towards the center of the Nyquist interval. Observe that significant differences between the mean of velocity estimates in figures B-1 and B-2 coincide with large estimate standard deviations. With the exception of the 300 m "true" outflow depth, this statistical bias is generally of greater magnitude than the modeling error treated in figures B-1.

The simple geometrical simulations used in this appendix reproduce the qualitative features of the time-series signal simulations plotted in figure III-15; remaining differences are due to the simplifying assumptions used here for the distribution of the autocorrelation lag estimate error.
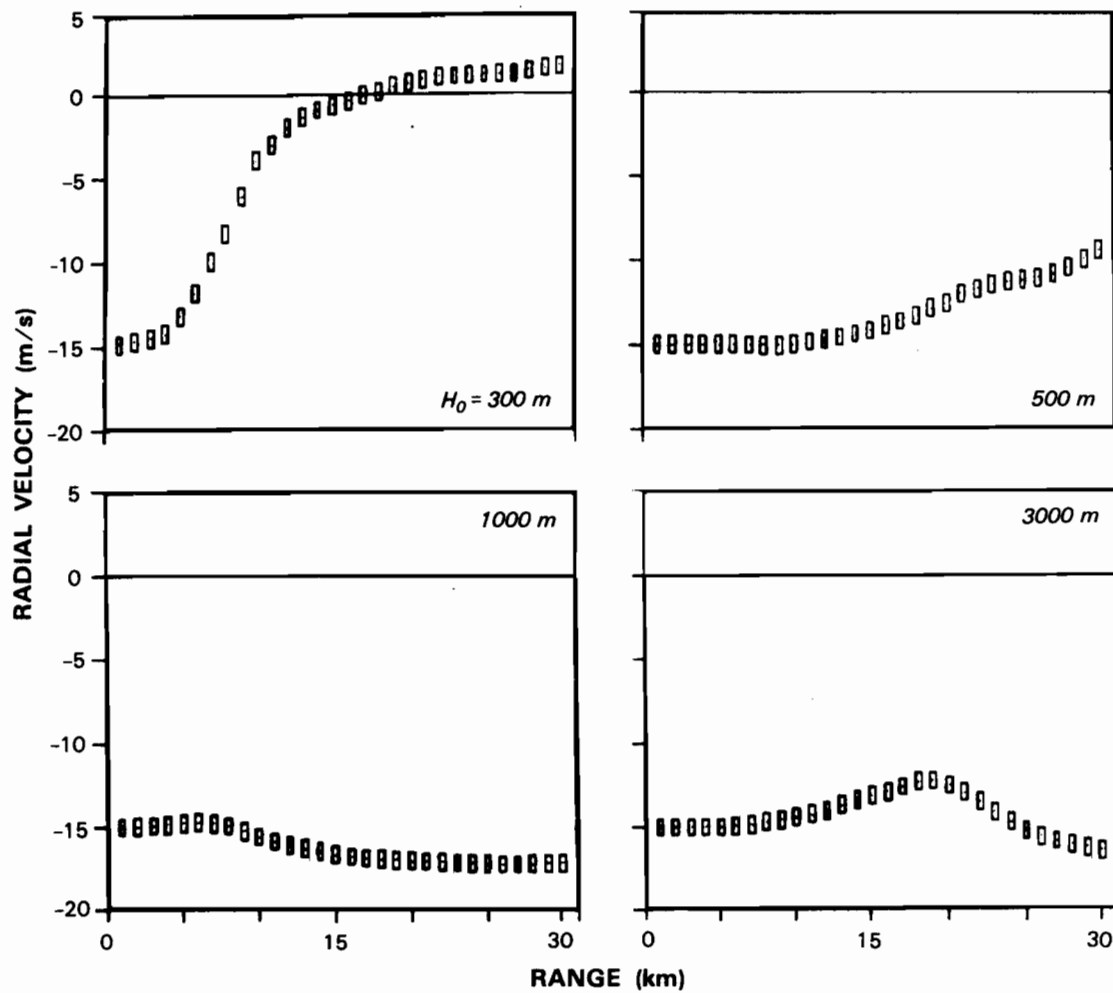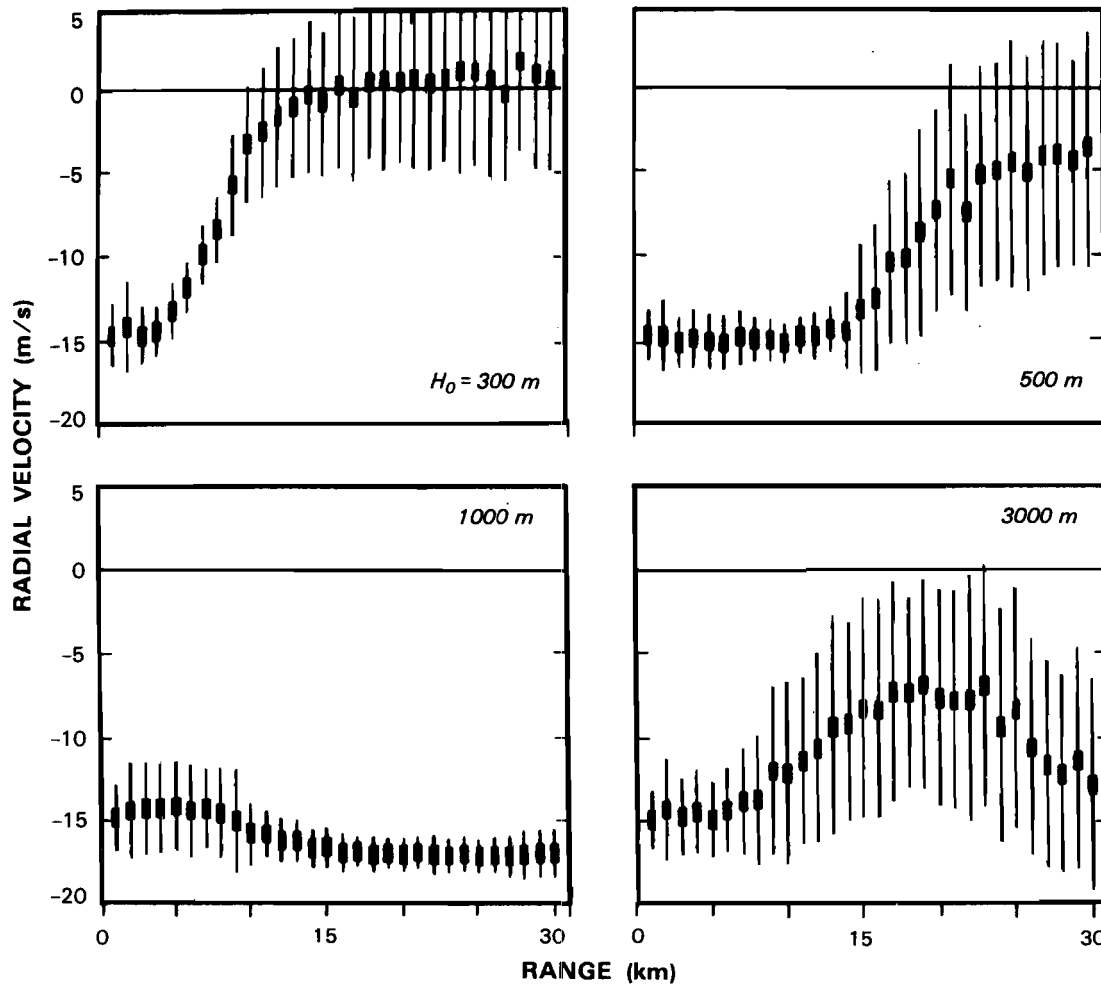
Figure B-1.   Dual-channel velocity estimate versus range assuming autocorrelation functions can be determined without error. The outflow model is as in Figure III-2.

Figure B-2.   Dual-channel velocity estimate versus range including an error contribution from statistical uncertainty in estimation of autocorrelation functions.

APPENDIX C: GROUND CLUTTER MEASUREMENTS AND DATA REDUCTION

Bill Drury at Lincoln Lab has designed an instrumentation package to record ground clutter with an operational ASR-7 or ASR-8. The system is sketched in Figure C-1. On each antenna scan, I and Q samples from a sector that is 96 range gates by 256 pulse transmissions are buffered, then written to magnetic tape during the remainder of the scan. The radar transmits at a uniform pulse repetition frequency of 1024 s^{-1} while scanning azimuthally at a nominal rate of 12.5 RPM. Range gate spacing for an ASR-8 is 140 m. Thus the wedge-shaped area recorded on one antenna scan is 18.5° by 13.4 km. The starting azimuth and range for data collection are selected with thumbwheel switches.
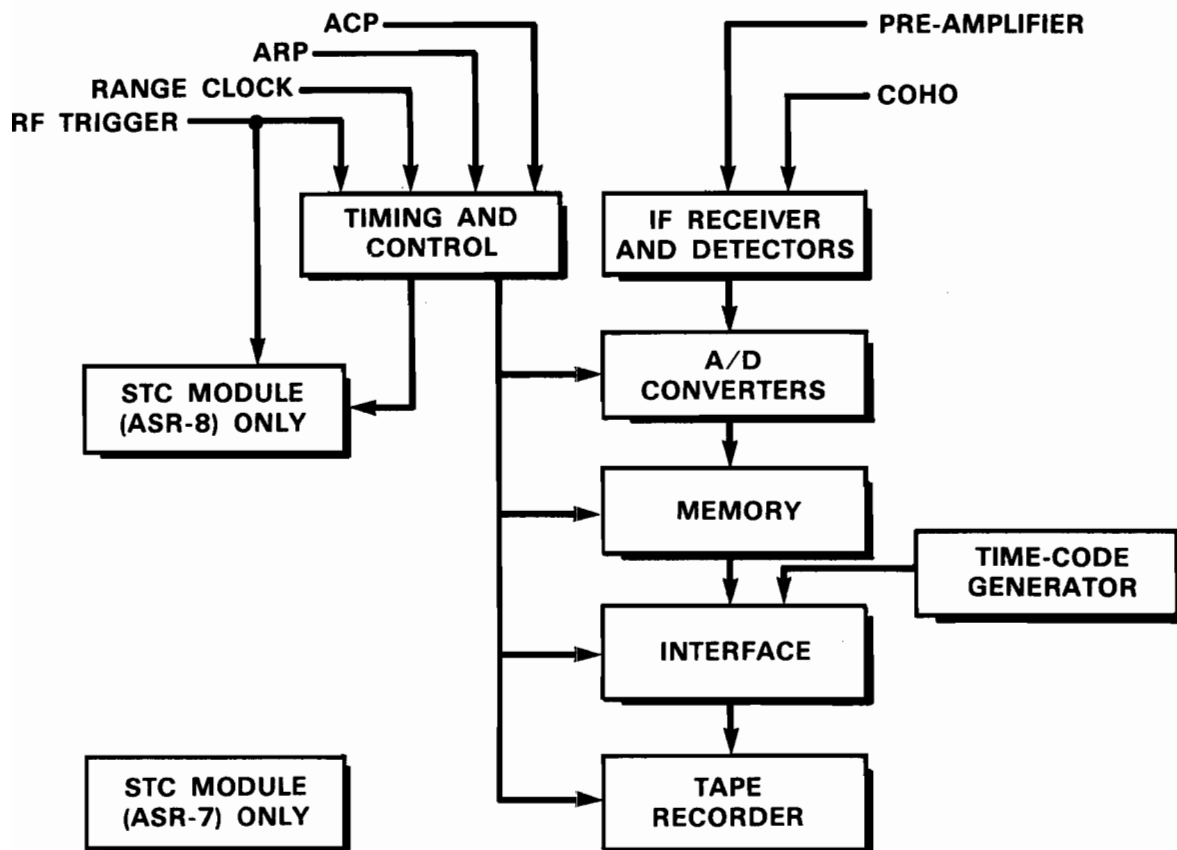
In operation, data from a given wedge were recorded on five successive antenna scans to allow for power averaging or examination of scan-to-scan fluctuations. The measurements were repeated with new start azimuths or ranges in order to provide full azimuthal coverage from 0 - 30 km. As is evident in Figure IV-1, small range-azimuth sectors were missed owing to operator error or recording system malfunction.

The parameters of an ASR-8 are quite similar to the ASR-9 parameters listed in Table I-1. For the ground clutter measurements, an STC function that varied as $(R/18.5 \ km)^3$ was used. This selection results in constant sensitivity with range inside 18.5 km when the data are used to compute the ground clutter cross-section density σ_0. Figure C-2 plots the dynamic range limits of the measurements in these units. Inside 18.5 km, clutter cross-section densities between -72 dB $(// \ 1m^2/m^2)$ and -2 dB can be measured if data from the two receiving beams are merged.

Table C-1 lists the sites where measurements have been made as well as the antenna heights and prevailing wind speed. The radar at the FAA Technical Center was used to test the equipment and to develop operating procedures. Measurements at Huntsville were made primarily to support an experimental program in which Lincoln Laboratory is involved. In this report, therefore, we considered only data from radars at the major air-terminals in Memphis and Denver.

Table C-1: Sites for Ground Clutter Measurements with ASRs			
Site	*Radar*	*Prevailing Wind Speed*	*Antenna Height*
FAA Technical Center, Atlantic City, N.J.	ASR-8	< 5 ms^{-1}	77 feet
Memphis International Airport	ASR-8	< 5 ms^{-1}	67 feet
Madison County Airport, Hunstville, AL	ASR-7	calm	57 feet
Stapleton Airport, Denver, CO	ASR-8	calm	17 feet

Data reduction consisted of: (i) power averaging of returns in each resolution cell over the five successive antenna scans and the 20 pulses transmitted as the antenna swept across one

ACP

ARP

RANGE CLOCK

RF TRIGGER

PRE-AMPLIFIER

COHO

TIMING AND CONTROL

IF RECEIVER AND DETECTORS

STC MODULE (ASR-8) ONLY

A/D CONVERTERS

MEMORY

TIME-CODE GENERATOR

INTERFACE

STC MODULE (ASR-7) ONLY

TAPE RECORDER

75674-5
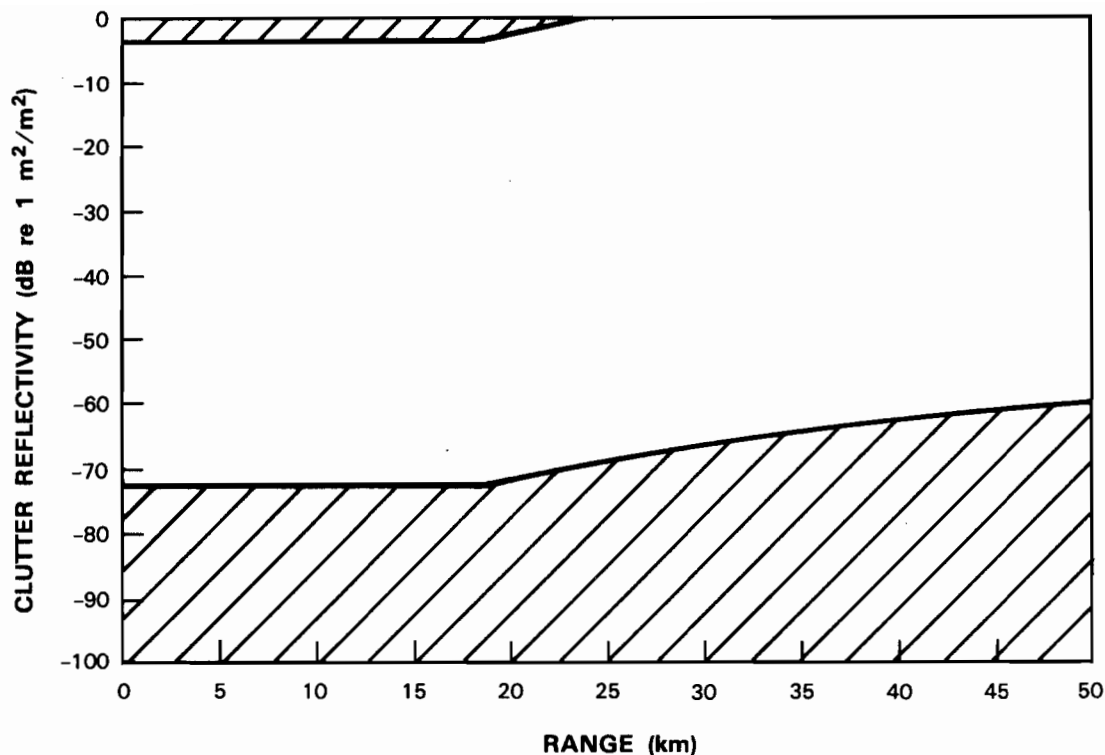
Figure C-1.   ASR ground clutter recording system.

Figure C-2.   Dynamic range limits for ASR ground clutter measurements versus range from radar. Expressed in terms of clutter cross-section density, σ_0.

beamwidth; (ii) scaling of these averaged sampled intensity values to represent received power in milliwatts. The scaling constant was calculated by comparing the noise level for the sampled data to the nominal receiver noise level for an ASR-8. Data from the furthest 4.2 km range interval were averaged to estimate the sampled noise level; visual examination of a PPI display was used to exclude sectors within this interval containing ground clutter. The averaged power levels in each resolution cell were then thresholded 4 dB above this noise level to exclude receiver noise from the analysis.

This report considered therefore the scan-averaged ground clutter intensity. When a resolution cell contains many scatterers of comparable cross-section, relative movement on the order of the radar wavelength can result in large fluctuations in signal intensity. The time-scale for such movement is generally large compared to the duration of a CPI but small relative to the scan period. Clutter intensity measurements for a given resolution cell therefore fluctuate on a scan-to-scan basis according to a non-central Chi-squared distribution. In the limiting case that no large, discrete scatterers are present in a resolution cell, the distribution function is exponential and the standard deviation of the clutter intensity samples equals their mean.